The Synthesis and Characterization of Porous, Conductive, and Ordered Materials
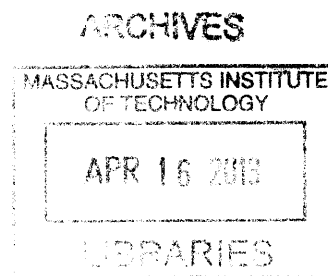
By

Tarun Chandru Narayan

Submitted to the Department of Chemistry
In Partial Fulfillment of the Requirements for the Degree of

Master of Science

At the

Massachusetts Institute of Technology

February 2013

Signature of Author _____
Department of Chemistry
21 September 2012

Certified by _____
Mircea Dincă
Professor of Chemistry
Thesis Supervisor

Accepted by _____
Robert Field
Chairman, Departmental Committee on Graduate Students

The Synthesis and Characterization of Porous, Conductive, and Ordered Materials

By

Tarun Chandru Narayan

Submitted to the Department of Chemistry
On 7 September 2012 in Partial Fulfillment of the
Requirements for the Degree of Master of Science in
Chemistry

ABSTRACT

Two different classes of polymers were pursued as candidates for materials possessing porosity, conductivity, and crystalline order. Attempts were made with hexaazatrinaphthylene- and dibenzotetrathiafulvalene-based precursors with boronic acids to prepare covalent-organic frameworks (COFs) possessing boroxole linkages. After preparing the precursors, several different reaction conditions were attempted, but the desired COFs proved elusive.

The second class of materials was tetrathiafulvalene-based metal-organic frameworks (MOFs). These materials were constructed with tetrathiafulvalene tetrabenzoic acid and zinc, cobalt, and manganese nitrate to give helical structures with approximately cylindrical pores. This structure type has one close S$\cdots$S contact of 3.8 Å which acts as a potential avenue for charge transfer. Gas sorption measurements suggest that the materials retain porosity upon evacuation. The material possesses high charge mobility as determined by flash photolysis time-resolved microwave conductivity measurements.

Thesis Supervisor: Mircea Dincă
Title: Assistant Professor of Chemistry

Table of Contents

List of Figures, Tables, and Schemes

Chapter 1. Motivation

Porous, conductive, and ordered materials have the potential to impact many fields in energy science. Applications range from fuel cell components to batteries to electrocatalysts to sensors to photovoltaics. Some porous conductors are already in use in these areas. Fuel cells face a great need for these materials. These materials can find two uses in this technology, namely gas transport as a support and as one of the electrodes.[1] As a gas transporting support, the materials are responsible for the diffusion of reactant gases to the electrodes, providing mechanical support for electrolytes that are frequently fragile, and interfacing with current collection elements. The electrodes require electrical and ionic conductivity, porosity for gas diffusion and liquid for three-phase reactions, and mechanical stability. Porous ceramics are typically used in this area for many of the high temperature solid oxide fuel cells, but there is space for new materials in cells that function at lower temperatures such as polymer electrolyte membrane cells. Since these cells often have problems with CO contamination, a material containing pores unfavorable for CO but favorable for other gasses may be of interest.

Porous materials are also being explored for technologies other than fuel cells. The ability to access a large number of active sites in a porous material allows for increased catalytic activity. Semiconducting, porous manganese oxides have shown to perform oxidative catalysis of simple substrates such as benzyl alcohols. Although they do not appear to be particularly conductive, materials derived from iron-sulfur clusters and divalent metal ions show appreciable catalytic activity towards carbon dioxide and carbon disulfide reduction.[2,3] A material that possesses active sites in a porous, conductive matrix can more efficiently utilize the advantages of porous materials in catalysis.
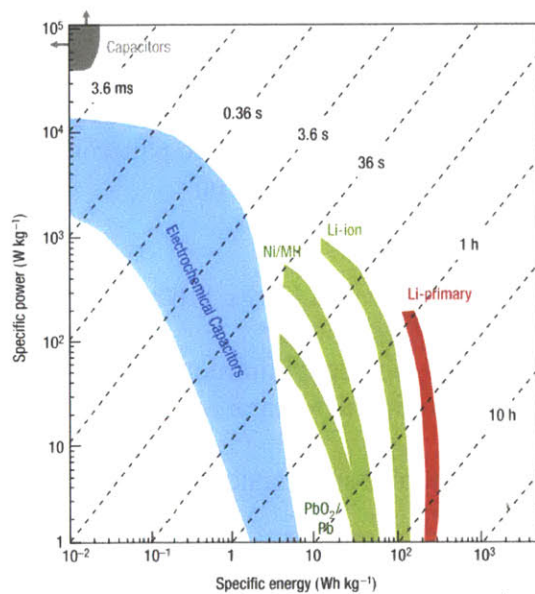
Figure 1.1 Ragone plot of different energy storage technologies.[4] Reproduced with permission from Ref. 4.

Energy storage technologies that can provide sustained power for applications drawing a large current are becoming increasingly valuable in the search for alternative sources of energy. The energy storage landscape is well organized in the Ragone plot shown in Figure 1.1.[4] The

ideal energy storage solution would lie on the upper right corner of this plot, meaning it would be capable of storing a large amount of energy as well as delivering it at high rates. Typical battery materials such as $LiCoO_2$ and $LiFePO_4$ undergo phase changes upon deintercalation. The channels for Li transport are also very narrow, resulting in sluggish charge transport.[5] The electronic charge transport in these materials is also fairly low, necessitating a conductive binder such as carbon. This decreases the weight percent of active material, thus decreasing the energy density of the device.

Supercapacitors are based on fast ion movement and thermodynamically and kinetically accessible redox couples. These storage devices tend to have high power density but relatively low energy density. The term supercapacitor has come to encompass a broad range of technologies. On one end of this spectrum one can consider the slower redox reactions approaching those present in battery systems. These systems, known as pseudocapacitors, are characterized by an intercalation and electron transfer. The other end of the spectrum constitutes a physical rather than chemical storage of ions. Materials of this sort are known as electrical double layer capacitors. Here, the ions remain in the pore and interact minimally with the storage materials. Porous activated carbons offer numerous sites for ion storage, but achieve minimal chemical interaction with the ion. Many materials such as manganese and ruthenium oxides exhibit fast redox couples with their respective hydroxides and thus fall somewhere in the middle of this spectrum. These materials frequently possess disordered pores and thus do not present a defined pathway for the movement of ions. A material that possesses a high degree of order, electrical conductivity, and ionic conductivity will tremendously assist the progress of this growing field.

Porous, conductive, ordered materials also have potential to be useful materials in the area of photovoltaics and are only beginning to be exploited in this area. Chromophores can be incorporated in a crystalline lattice with pores to carefully design the nature of chromophore aggregation. The proper arrangement of these chromophores will allow for enhanced absorption, thus allowing for the increased utilization of solar energy. In addition to better absorption, the ability to rationally control the arrangement of chromophores allows for the incorporation of highly efficient charge transport pathways, which would mitigate the commonly encountered problem of poor charge transport in organic materials.[6] Much of the work that has been done in this area has involved block copolymers that self-segregate into donor and acceptor supramolecular units. However, this often requires tedious synthesis and does not allow for direct measurement of donor-acceptor distances. A porous material may offer a solution to this problem. If the pores are sufficiently large, this approach will allow for the intercalation of different small molecules that can act as donors or acceptors. If the material is intrinsically p-type, n-type molecules can be intercalated into the pores and vice versa. This provides a well-defined pathway for electron transfer between the donor and acceptor. The exciton diffusion length must be very short in organic materials to allow for effective charge transfer. The direct overlap of donor and acceptor allows for the process to occur efficiently. In addition to the practical benefits, well-defined system allows for a fundamental study of charge transfer and its effect on efficiency of a device. In a crystalline system, there is a possibility of varying the pore size and chromophore to change the driving force for charge transfer as well as the distance between donor and acceptor. Conclusions drawn in these studies can be applied to small molecule systems with similar driving forces to estimate the interaction between donor and acceptor.

In order to prepare functional porous, conductive, and ordered materials, we sought to use organic materials in a well-defined lattice constructed of chromophores joined together with structure directing units. We were interested in different structure directing units – namely aryl groups consisting of multiple boronic acid units and metal ions or clusters. In the former case, we pursued covalent-organic frameworks (COFs), in which two-dimensional sheets of planar molecules are held together via π-π interactions. These materials tend to have large pores in which dye molecules may be intercalated. The combination of metal nodes and chromophores with linking groups leads to the preparation of metal-organic frameworks (MOFs). Although these materials tend to have smaller pores, MOFs are frequently highly crystalline, which allows for detailed studies of donor-acceptor electron transfer processes. We were able to prepare a MOF displaying high charge mobility. The material is highly crystalline and absorptive, exhibiting a charge transfer transition suggestive of a partially delocalized system.

Chapter 2. Towards Conductive Covalent-Organic Frameworks

2.1 Introduction

Covalent organic frameworks (COFs) are relatively new materials that have the potential to possess conductivity, porosity, and order. These frameworks, first reported in 2005,[7] are composed of light elements linked together with a variety of functional groups including boroxoles,[7–18] borosilicate trigonal bipyramids,[19] imines,[20] hydrazones,[21] borazines,[22] benzimidazoles,[23] and boroxines.[7,24] Many of these structures are composed of planar 2D sheets stacked along the third dimension. The crystallinity arises from the reversibility of the framework-forming reaction, which builds a regular 2D net. Although COFs display poor crystallinity, it is possible to resolve a few of the most intense powder X-ray diffraction peaks. By creating models to fit the powder diffraction data, it has been suggested that most of these structures adopt an eclipsed stacking motif. A complementary computational study has suggested that the stacks exhibit a slight offset relative to each other in the lowest energy configuration.[25] The exact organization of these stacks is of the utmost importance in understanding their electronic properties.[26] Computations have shown that the angle of offset between adjacent layers of a triphenylene COF plays a significant role in the degree of charge localization. When the layers are perfectly eclipsed, there is a slight delocalization of electron density onto adjacent aryl units. Even a slight rotation from this eclipsed configuration causes the electrons to preferentially localize on one unit. These studies were not carried forward to understand the impact of slight translational offsets between adjacent layers, but it is conceivable that the offset could also play a role in electron delocalization.

The electronic properties of COFs have only recently been given consideration.[13,17,24,27–30] A relatively early work introduces the idea of highly absorptive compounds such as phthalocyanines in porous frameworks.[31] This framework is comprised of phthalocyanines separated by oxanthrene-bound spirocyclic groups. The resulting material does not display interactions between phthalocyanine units as a result of the isolation of electroactive units. A subsequent study reported the preparation of a rigid phthalocyanine COF that appears to be stacked in an eclipsed fashion.[14] In order to access this compound, the authors utilized the more soluble tetra(acetonated) derivative of octahydroxy phthalocyanine. An *in situ* deprotection[32] was conducted using a strong Lewis acid, $BF_3 \cdot Et_2O$ followed by a reaction with *p*-phenylenedi(boronic acid) to furnish the desired material. There is no report of conductivity measurements, as the authors only report a UV-Vis-NIR spectrum in addition to gas sorption data. The UV-Vis-NIR data appears to resemble that of materials exhibiting a band edge, but the resemblance to the spectrum of the starting material indicates that assignment to band-based transitions may be premature.

The literature on porphyrins and phthalocyanines indicates that stacks of these electroactive π-systems can be highly conductive when doped.[33] Based on this information, significant conductivity in the as-prepared state would be surprising but treatment with iodine or another oxidant in a non-stoichiometric ratio could afford a highly conductive material. Previous studies indicate that phthalocyanine is most conductive in its + ⅓ state. A subsequent study on the nickel analog of this COF demonstrated weak photoconductivity.[30] This study supports the notion that phthalocyanine COFs are semiconducting since they exhibit some conductivity upon photogeneration of charge carriers. The more relevant quantity to study is the charge carrier mobility, as that is intrinsic to the material. The authors report values upwards of 1 $cm^2/V \cdot s$,

which is very high for a molecular material. The reported conductivity is low because the number of charge carriers is low. If the system is significantly doped or exposed to high intensity light, the number of charge carriers can increase drastically and lead to high conductivity.

Other organic systems have also been used as the electrically conductive component. Systems based on self-condensed pyrene boroxine systems[24] and boroxole-linked systems[17] of triphenylene and pyrene have also shown promising properties. In both cases, doping has a positive effect on the photoconductivity, although the triphenylene-based COF exhibits a more dramatic dependence on dopant levels. Triphenylene is more difficult to oxidize than pyrene by approximately 0.5 V,[34] but pyrene is functionalized with two electron withdrawing groups whereas triphenylene is decorated by six electron-donating groups. Hexahydroxytriphenylene is also calculated to have a fairly small reorganization energy upon accepting a hole, indicating that a hopping-based conduction pathway could be fast.[35]

In the search for another organic compound that could display interesting properties in a COF, we decided upon hexahydroxyhexaazatrinaphthylene (HATNOH). A hypothetical COF incorporating this synthon has potential applications in a number of different areas. Crystalline phases of hexaazatrinaphthylene (HATN) with alkylthio sidechains have been shown to have a charge mobility on the order of 0.5 cm^2/Vs, which is comparable to materials involving phthalocyanines and porphyrins.[36] Experiments and calculations with ordered stacks of alkyl HATN compounds in liquid crystals indicate a fairly large bandwidth of 2 eV with a significant sensitivity to the offset of the stacks.[37] Although the calculated reorganization energy upon accepting an electron or hole is larger than that of hexahydroxytriphenylene, it is still fairly low and thus amenable to charge transport. These pieces of information indicate that the HATN core is primed for applications requiring electrical conductivity. The bpy-like chelation sites on HATN also make it an attractive ligand for potential further chemistry. Several studies using small molecule complexes of hexaazatriphenylene (HAT) or HATN-derived systems have shown very strong MLCT bands that persist in oscillator strength at different redox states.[38-41] This property bodes well for applications in photocatalysis with the added advantage that bimolecular deactiviation is very unlikely in a rigid framework.

2.2 Towards Hexaazatrinaphthylene-Based COFs
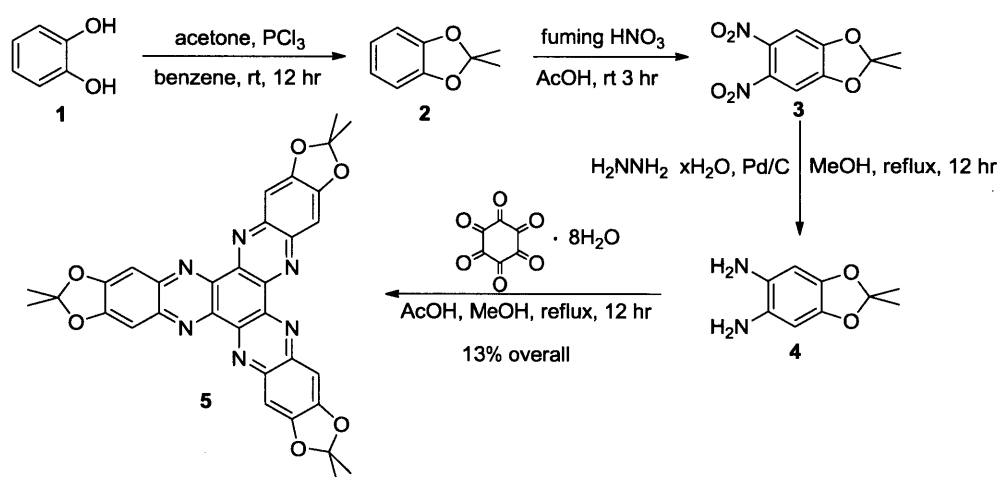
Scheme 2.1. Synthesis of triacetonated HATNOH (5)

We were able to access **5** in four steps from catechol and hexaketocyclohexane, as shown in Scheme 2.1. Catechol (**1**) was treated with acetone in the presence of phosphorus trichloride and benzene. The yield of this reaction was consistently under 50%, but **2** could be obtained in excess of 20g with consistency. The nitration proceeded smoothly as long as red fuming nitric acid was used. Other grades of fuming nitric acid led to either no reaction or very minimal conversion. Treatment of **3** with hydrazine hydrate and palladium on carbon afforded **4**. This compound is particularly air sensitive, so it was necessary to filter and handle the product in a nitrogen atmosphere; a glove bag provided sufficient protection to this end. ^{1}H NMR taken in solvents stored under ambient conditions showed no signal, indicating that the product is oxidized within minutes. The final condensation step was more challenging than anticipated due to poor solubility in ethanol, which is sometimes used as a solvent for the preparation of HATN derivatives.[42,43] Unlike related materials, **4** was not amenable to complete reaction in ethanol. After optimization of reaction conditions, we found that the reaction proceeded more smoothly in methanol, and a relatively pure product precipitated from the reaction mixture. Dissolving the crude product in chloroform and passing through an alumina plug afforded analytically pure **5**. Slow evaporation of the chloroform solution yielded dark yellow needles suitable for analysis with single crystal X-ray diffraction.

The solid state structure of **5** obtained in these reaction conditions is shown in Figure 2.1.The molecule crystallizes as a chloroform solvate in P2$_1$/c. It is not entirely planar and the bond lengths of each arm of the molecule differ slightly, resulting in a deviation from the idealized D$_{3h}$ geometry. The steric hindrance of the *gem*-dimethyl groups likely induces puckering to minimize interaction with methyl groups on an adjacent molecule. The stack of **5** is slipped such that the centroid is shifted by approximately 4.5 Å along one arm. The overall stacking motif can be described as a slipped eclipsed stack.
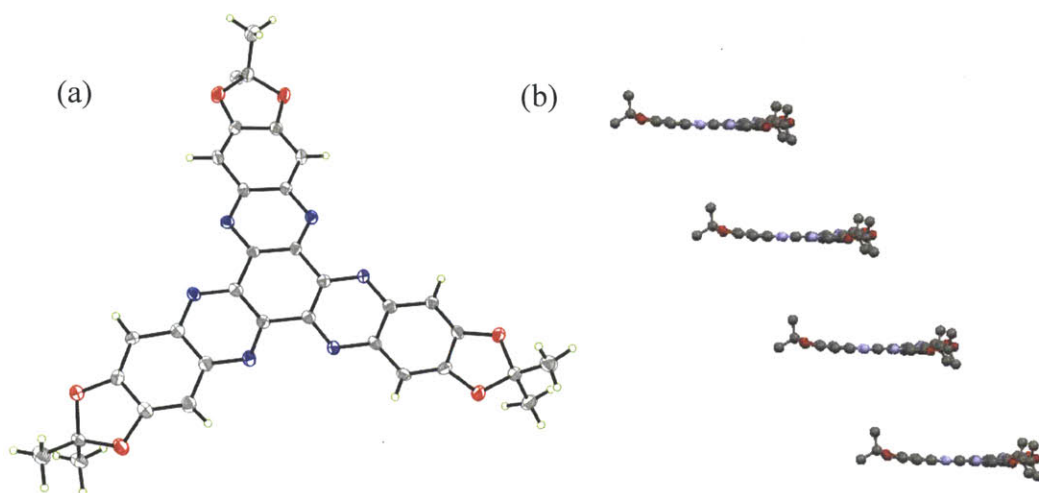
Figure 2.1 Solid state structure of **5**. Solvent molecules are removed for clarity. (a) An ORTEP of a molecule of **5**. (b) A diagram depicting the stacking motif and curvature of **5**.

Cyclic voltammetry, shown in Figure 2.2, suggested a reversible reduction at -1.74 V in 0.1 M tetra-*n*-butylammonium hexafluorophosphate in dichloromethane vs. Fc/Fc$^+$. The hexylthioether analog has three reported reductions in a less negative region, namely -1.49 V, -1.75 V, and -2.00 V.[36] The oxygen atoms can interact with the aromatic system more efficiently and thus donate more electron density to the core. The presence of extra electron density will

11

raise the LUMO and make the compound more difficult to reduce. The reduction potential is very low and requires potent reductants such as sodium naphthalenide for reduction. Assuming the viability of a COF with this material, it may be difficult to introduce reducing agents of this strength without destroying the framework.
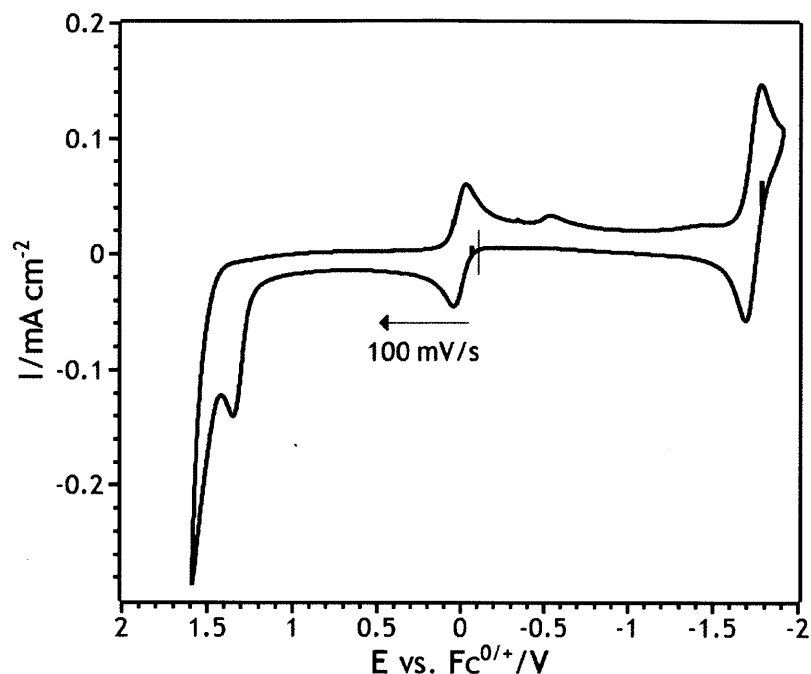
Figure 2.2 Cyclic voltammogram of **5** in 0.1 M tetra-n-butylammonium hexafluorophosphate in dichloromethane with a glassy carbon button working electrode, platinum wire counter electrode, and silver wire pseudoreference electrode in the presence of ferrocene. The scan was performed at 100 mV/s. The trace shown corresponds to the third cycle.

We also recorded a UV-Vis spectrum in chloroform shown in Figure 2.3. The peaks observed have a high molar absorptivity, albeit in a high-energy region of the spectrum. **5** allows for some donation of the oxygen atoms into the aromatic system, but it is likely that this effect will increase in the case of the deprotected system and the corresponding boroxole ring. The more delocalized electron density in these cases will lead to a red-shifted absorption spectrum.
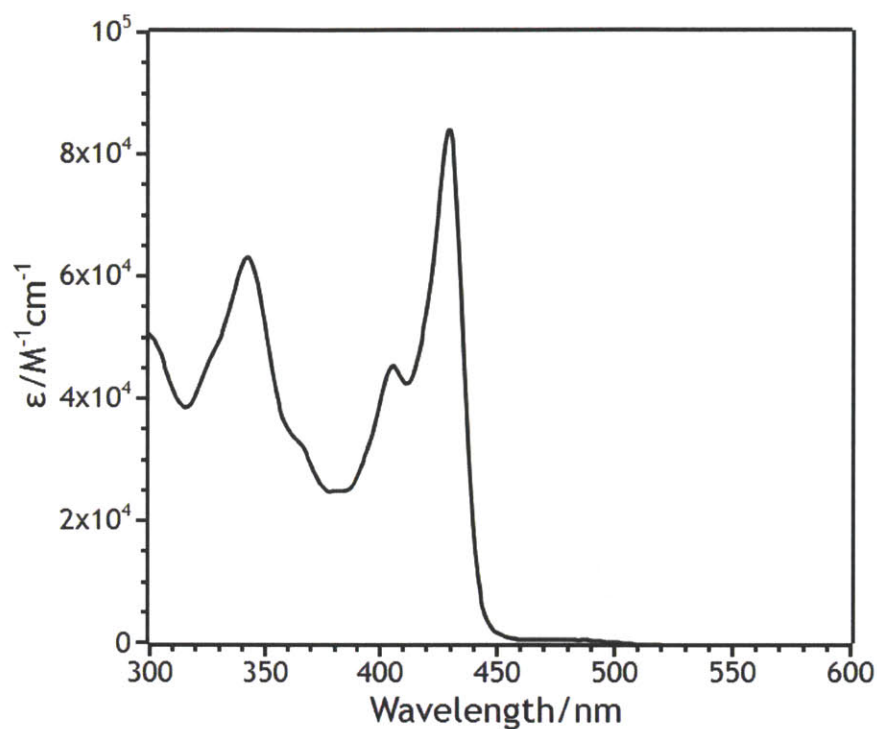
Figure 2.3 UV-Vis spectrum of **5** in chloroform. There were no observed features between 600 and 1000 nm.
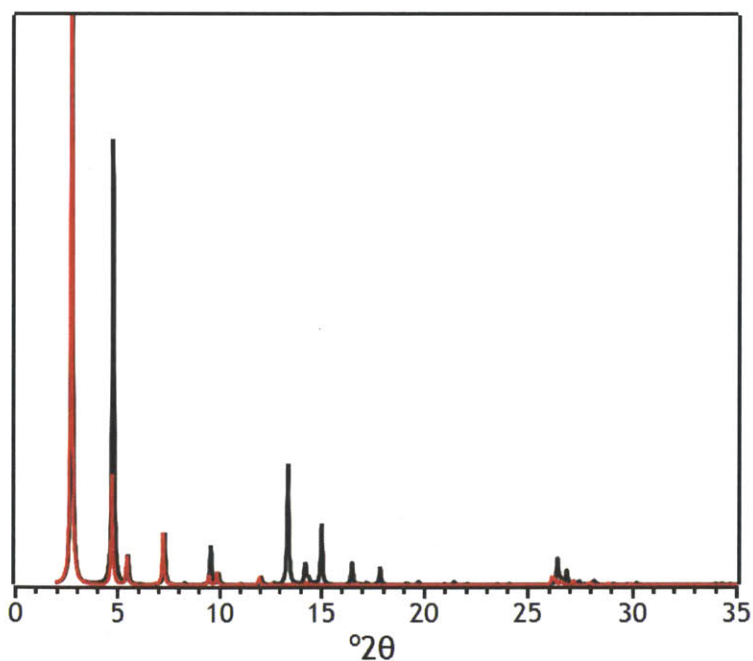
Figure 2.4. Simulated PXRD patterns for COFs derived from HATNOH and *p*-phenylene diboronic acid in staggered (black) and eclipsed (red) stacking motifs.

Once we fully characterized **5**, we attempted numerous reaction conditions with *p*-phenyleneboronic acid to try to obtain the corresponding COF. Simulation of the PXRD patterns corresponding to eclipsed and staggered structures was performed to determine expected patterns, as shown in Figure 2.4. Although the staggered motif clearly has extra peaks near 15° 2θ, COFs tend to exhibit very poor crystallinity and their PXRD patterns only display a few intense reflections. As a result, we anticipated that the two structures would be difficult to distinguish by diffraction alone.

Starting material	HATNO(acet)	HATNO(acet)	HATNO(acet)	HATNO(acet)	HATNOH	HATNO(acet)	HATNOH
Solvent 1	Mesitylene	Mesitylene	Mesitylene Anisole Toluene	Mesitylene Toluene Anisole Xylene	Mesitylene Toluene Anisole Xylene	Mesitylene Anisole Toluene Xylene	Anisole Mesitylene
Solvent 2	Dichloroethane	Dichloroethane	Dioxane Methanol	Dioxane Dichloroethane Dioxane	Dioxane Dichloroethane Dioxane	Dioxane Methanol Dichloroethane	Dioxane Dichloroethane Methanol Ethanol Acetonitrile
S1/S2	1:1	1:1	1:1 for diox 9:1 for MeOH	1:1 for diox/DCE 9:1 for MeOH	1:1 for diox/DCE 9:1 for MeOH	for diox/DCE: 1:3, 1:1, 3:1 for MeOH: 9:1, 19:1, 59:1	For diox/DCE: 1:3, 1:1, 3:1 for Me/EtOH: 9:1, 19:1, 59:1 for MeCN: 1:3, 1:1, 3:1, 0:1
O₂ precaution	3 FPT, add BF₃, 2 FPT	Flash freeze	3 FPT after BF₃	Flash freeze	Flash freeze	none	distilled anisole
Temperature	120°C	140°C	120°C	85°C	85°C	120°C	160°C
Time	4 days	1 week	1 week	5 days	5 days	15 min	25 min
Notes						microwave	microwave, stirring

Table 2.1. Attempts to make HATNOH-based COFs. All reactions were performed with degassed solvents.

With these patterns in hand, we attempted a variety of reaction conditions tabulated in Table 2.1. We began with conditions typically used to prepare COFs, taking extensive precautions to exclude oxygen. The addition of $BF_3 \cdot Et_2O$ caused an immediate color change from yellow to red, likely corresponding to the deprotection of the acetone groups since it would correspond to greater delocalization, as discussed above. The resulting compounds were amorphous or corresponded to the structure of either of the starting materials. To account for the possibility of oxygen-assisted bond formation, we attempted a similar synthesis without freeze-pump-thaw cycles. This set of conditions resulted in very similar products. We then moved to a different combination of aromatic and polar solvents, namely dioxane and mesitylene noting that solvent choice has a significant impact on the crystallinity and identity of the product. After taking precautions to exclude oxygen and allowing the reaction to proceed for a week at high temperature, we again did not see any low angle peaks corresponding to the (100) peak of our proposed structure. We also noted that none of the reaction conditions discussed so far yielded a material possessing an IR absorption band near 1325 cm⁻¹, which would correspond to stretches in a boroxole ring. All known COFs using this linkage have a strong, broad absorption in this region.

To check if we were bypassing the desired phase in favor of an unknown thermodynamic product, we tried a series of reactions at lower temperature. A reaction in 1:1 anisole/dioxane afforded red crystals suitable for single crystal X-ray diffraction. Contrary to expectation, these red crystals corresponded to a new phase of **5** as its dioxane and chloroform solvate, as seen in

14

Figure 2.5. In this case, acetonated HATNOH units have a much closer intermolecular spacing of approximately 3.7 Å. The primary factor enabling this close packing arrangement is that the molecules exist in a slipped staggered stacking motif. The staggered packing motif helps to enforce a more planar configuration of **5**, thus offering more delocalization and a consequent red shift in absorption.
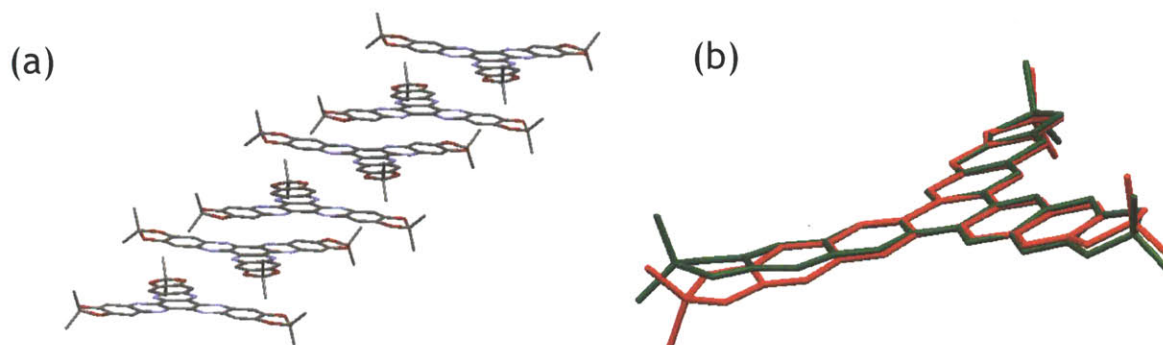
Figure 2.5 (a) Depiction of the stacking motif of the dioxane and chloroform solvate of **5** with solvent molecules removed. (b) Overlay of the chloroform solvate (green) and dioxane and chloroform solvate (red) of **5**.

Noting that **5** persisted despite the addition of an excess of BF$_3$·Et$_2$O, we were unsure if we were accessing HATNOH. In order to investigate this matter, we treated **5** with a large excess of BF$_3$·Et$_2$O to generate a red solid that had significantly different solubility properties when compared to the starting material. ^{1}H NMR in (CD$_3$)$_2$O indicated the presence of weak aromatic peak significantly downfield from the starting material. This shift would suggest that the aromatic ring is becoming more electron deficient in the product, which is contrary to the expectation that hydroxy groups would serve as electron donors into the aromatic system. Purification of the product proved difficult and a sample suitable for elemental analysis was not obtained. Despite the impure and uncertain nature of the obtained material, we attempted different reaction conditions to try to access COFs. The resulting materials exhibited powder patterns that did not match those of either of the protected HATNOH structures or the predicted COF structures and did not show characteristic boroxole IR stretches.

To provide an increased driving force to form the boroxole ring, we looked to the alternative of microwave synthesis. Even in the presence of dehydrating agents such as triethyl orthoformate, we were unable to detect any boroxole formation. The compound nominally designated as HATNOH also did not produce any of the desired COF materials when combined with phenylene diboronic acid in the microwave.
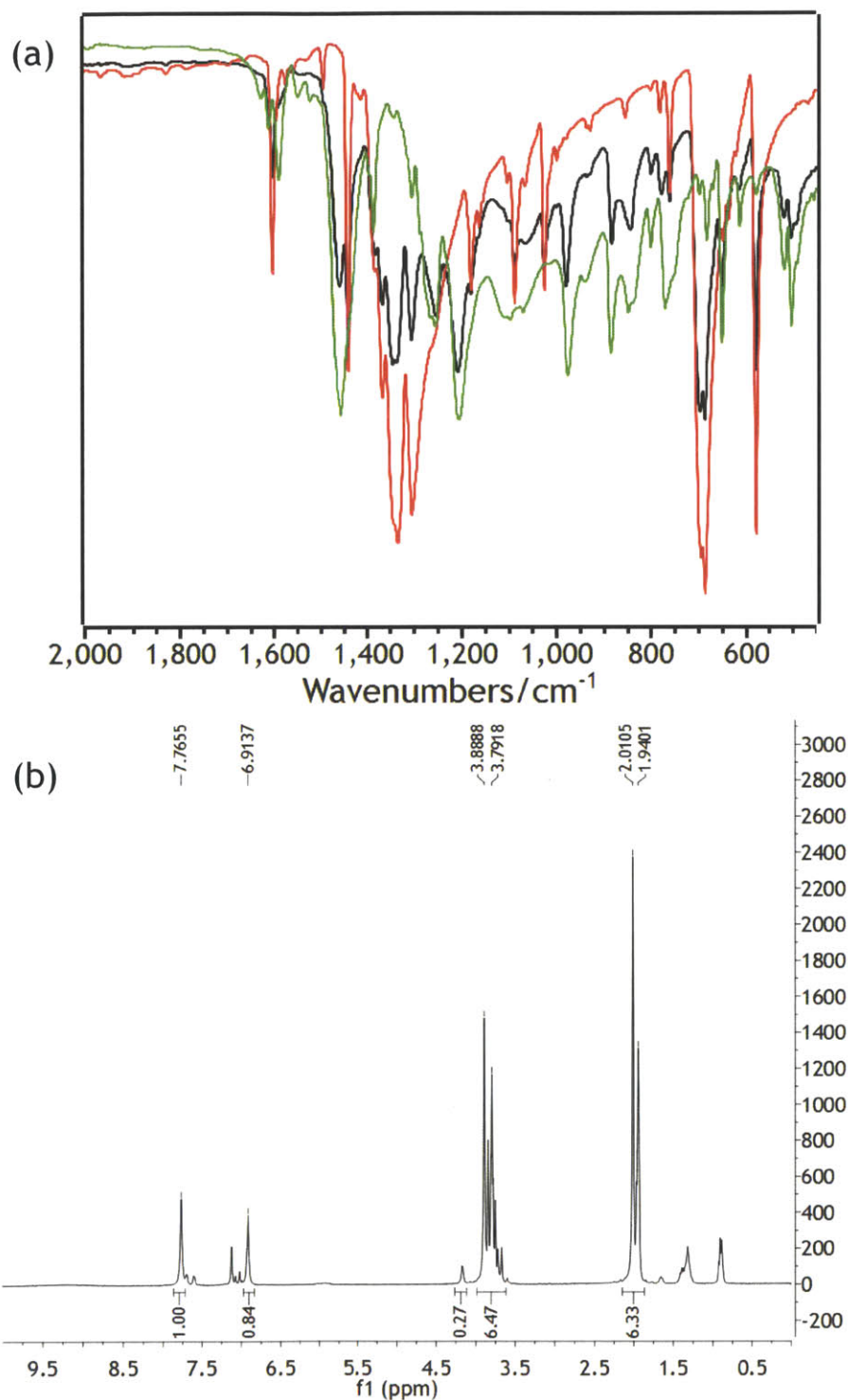
Figure 2.6 (a) IR spectrum of the reaction product (black) of putative HATNOH (green) and phenylboronic acid (red). (b) ^{1}H NMR spectrum in CD$_3$CN of the reaction product between 3,4,5-trimethoxyphenyl boronic acid.

The COF-forming reactions were entirely unsuccessful, so we sought to perform a simpler reaction – the reaction of a monoboronic acid with acetonated and deprotected HATNOH. We initially chose an approach similar to the initial attempts made at synthesizing COFs. When a suspension of **5** and phenylboronic acid in dry toluene was treated with $BF_3 \cdot Et_2O$, the reaction mixture started to become red as is typical with this treatment. Heating at reflux and then removing the solvent *in vacuo* gave a product whose IR spectrum, shown in Figure 2.6a, does not appear to contain a B-O stretch. We then attempted other reactions with the putative HATNOH and phenylboronic acid in either toluene/methanol or no solvent. In both cases, we obtained a product containing IR stretches that appear to be the sum of the stretches present in the two reactants. Due to lack of solubility, we were unable to characterize this product further. This inability led us to pursue more soluble derivatives. We chose 3,4,5-trimethoxyphenyl boronic acid[44] since it possesses solubilizing groups that do not interfere with the boronic acid reaction site. We also decided to start with a material with a known identity, **5**. Upon suspension in anhydrous acetonitrile with 3,4,5-trimethoxyphenyl boronic acid, treatment with $BF_3 \cdot Et_2O$ afforded a slight color change and addition of ~10 μL water cause the reaction mixture to darken and become homogeneous. Removal of solvent left behind a solid, dark residue. The ^1H NMR spectrum in CD_3CN, shown in Figure 2.6b, indicates the presence of a variety of impurities that cannot be assigned.
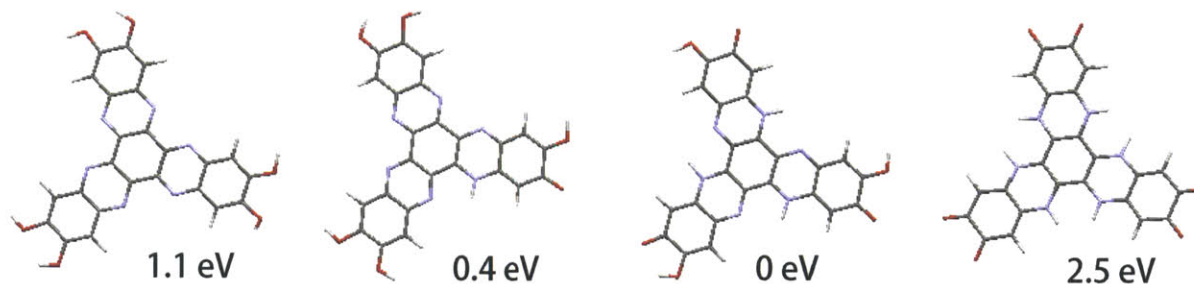
Figure 2.7 Calculated geometries for different HATNOH tautomers. All structures were calculated to be flat except for the all amino-keto tautomer shown on the right. The numbers below each structure correspond to the zero-point energies relative to the lowest energy structure, the tri(amino-keto) tri(imino-hydroxy) tautomer.

Preparing the molecular species modeling the COF was proving difficult, so we looked to computation to provide some insight. An inquiry from Prof. Geoffrey Coates regarding the potential of tautomerization in HATNOH pushed us to investigate the relative stabilities of different tautomers of HATNOH. We considered two sets of possibilities – those with the initially anticipated imino-hydroxy tautomeric form and those existing in the amino-keto form. We then selected four tautomers for further study – molecules existing (1) exclusively in the imino-hydroxy form, (2) with one amino-keto motif and five imino-hydroxy motifs, (3) with one amino-keto and one imino-keto functionality on each arm, and (4) exclusively in the amino-keto form. The optimized structures and relative single-point energies are shown in Figure 2.7. The HATNOH derivative with three amino-keto was calculated to be the lowest energy of the four structures considered. This finding suggests that HATNOH is likely to be much less nucleophilic

17

than we had initially expected since the hydroxyl groups will likely have significant ketone character.
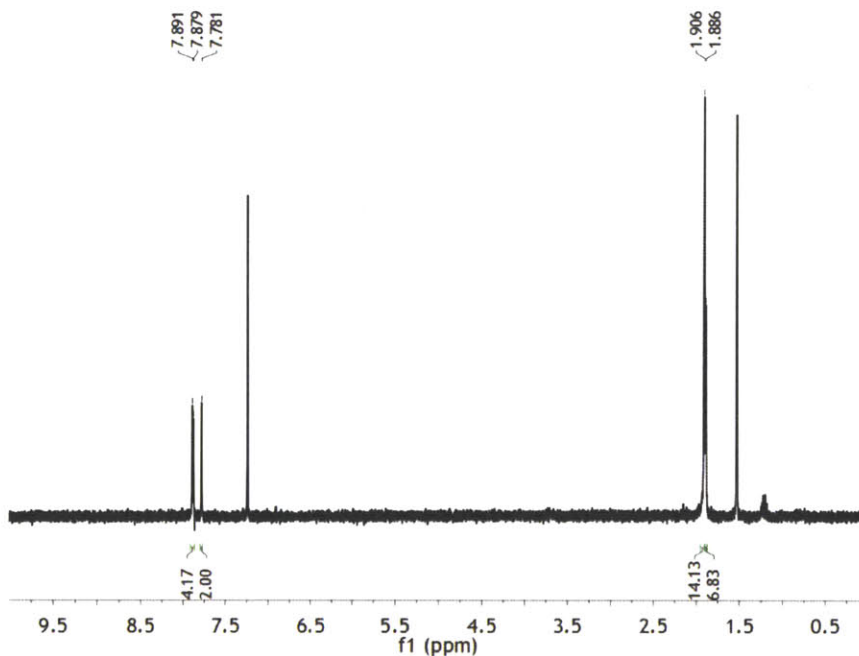
Figure 2.8 ^{1}H NMR spectrum of zinc-HATNOH adduct in CDCl$_3$.

We tried installing metal centers at the bpy-like positions to reduce the favorability of the amino-keto tautomer and restore nucleophilicity to the hydroxyl groups. Noting the success of microwave-assisted synthesis for installing metal centers in related systems,[45–47] we tried follow similar procedures with both zinc and nickel chlorides. Compound **5** was added to a solution of either zinc or nickel chloride hydrate and heated to 80°C for 15 minutes in a microwave reactor. In the case of zinc, the reaction yielded a fine powder whereas the reaction with nickel yielded a homogeneous solution. Although the mass spectra for both species only indicated the presence of monomers, dimers, and trimers of acetonated HATNOH, the ^{1}H NMR spectrum of the product of the zinc reaction indicated the presence of a pure material, which is likely the monosubstituted derivative, as seen in Figure 2.8. Further treatment of the product of the zinc reaction with a fresh batch of zinc nitrate in the microwave did not afford additional zinc binding.

2.3 Towards Dibenzotetrathiafulvalene-Based COFs

The difficulty in accessing COFs based on HATNOH caused us to look elsewhere for new synthons. We looked to tetrathiafulvalene (TTF),[48] which is one of the most studied electroactive organic systems.[49] It is very easily oxidized and forms a stable cation and dication since each oxidation causes the formation of a 6π electron aromatic system in a dithiole ring.[50] The ease with which TTF can stabilize different oxidation states is a key precursor to fast electron transport. Studies have shown that polycrystalline pellets of TTF$^+$Cl$^-$ have a conductivity of 0.27 S/cm.[51] This conductivity is likely due to the columns of TTF radical cations that form reasonably dispersive bands through the interaction of the frontier π orbitals.[52] The ease of introducing charge carriers and the high electrical conductivity led us to propose a

series of COFs containing TTF that should exhibit high electrical conductivity. We wished to utilize the easy oxidation of TTF, so we wanted to link TTF to a trigonal node through an electron rich functionality such as a catechol, namely tetrahydroxy dibenzotetrathiafulvalene (THDBTTF). This would preserve the ease of oxidation of the TTF core. One potential trigonal node is 1,3,5-tri(boronic acid) benzene. In such a system, the exclusive conductivity pathway would be through a TTF p-stack, so it would be easy to isolate the conductivity due to TTF. The next goal was to utilize electroactive trigonal linkers such as triazine to have a well-ordered charge transfer salt that exhibits large hexagonal pores.
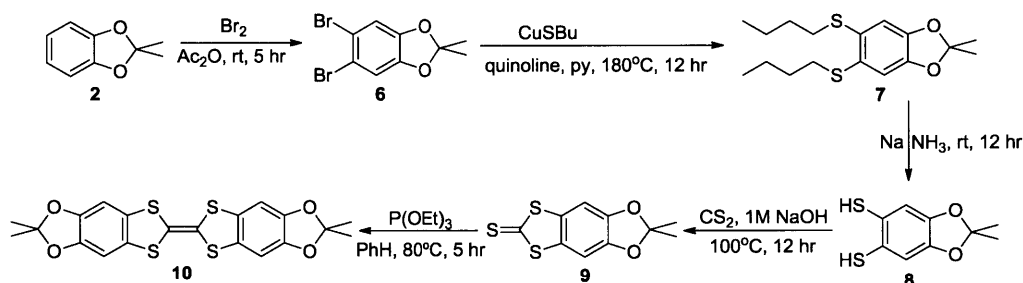
Scheme 2.2 Synthetic scheme for diacetonated tetrahydroxyTTF (**10**)

We first developed a synthesis for **10**, as shown in Scheme 2. Initial attempts to prepare **6** were successful on large (>10 g) scales, but subsequent attempts at that scale were met with failure. The reaction is most reliable when performed on a 1 g scale. Treatment of **6** with copper (I) butanethiolate at high temperatures afforded **7**, albeit with a significant impurity that persisted after chromatography. Even when the reaction conditions were altered, the impurity remained, so we chose to proceed in the synthesis with an impure product. The product of the Birch reduction retained an impurity that could be removed upon sublimation. The subsequent deprotonation of the thiols and reaction with carbon disulfide afforded a pure, yellow precipitate (**9**) regardless of the purity of the starting material. The reaction of the thione with triethylphosphite furnished **10**. The TTF derivative is air stable, although it should be noted that after pulling through large quantities of air, the material changes from marigold to a paler yellow color, which could be indicative of a chemical change.

We then attempted to prepare a model complex with phenylboronic acid in benzene with the addition of $BF_3 \cdot Et_2O$ at reflux for three days. After filtration in a nitrogen environment, the solid was examined by IR spectroscopy, as seen in Figure 2.9. The material exhibits a shift in stretching frequency near 1350 cm^{-1}, which is in the area expected for a B-O stretch of a boroxole. Again, solubility was a problem, so NMR spectroscopy could not be performed. When the filtrate was moved into ambient atmosphere, the yellow solution turned green within minutes. Since TTF is highly susceptible to oxidation, it is unsurprising that the reaction would occur that quickly.
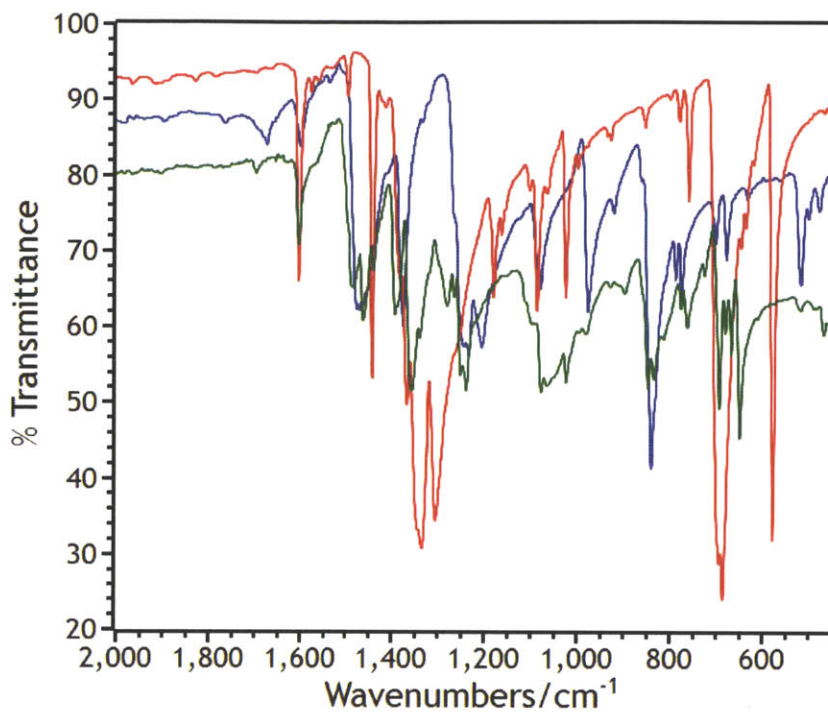
Figure 2.9. IR spectra of phenylboronic acid (red), **10** (blue), and the reaction product of a reaction in benzene (green).

Noting the promising stretch in the IR, we then attempted to prepare a soluble derivative using mesityl boronic acid with less success. ^{1}H NMR of the product suggested at the presence of a number of different compounds, although none of them had signals characteristic of a mesityl unit. Examination of the corresponding IR spectrum showed that there was no significant stretch in the expected B-O stretching region. We surmised that the *ortho* methyl groups provided enough steric hindrance to prevent B-O bond formation.

We followed a similar set of reaction conditions as those used to try to prepare COFs based on HATNOH with the TTF-based materials. We consistently started with the acetonated form of the ligand because the deprotected form proved very difficult to obtain. Upon adding $BF_3 \cdot Et_2O$, the only visible indicator of a reaction was a slight browning of the reaction mixture. We attempted syntheses with mesitylene and anisole as the high boiling solvents with polar cosolvents such as methanol, dichloroethane, dioxane, and acetonitrile and did not obtain the expected structure in any case. On the occasion that a crystalline material was obtained, the (100) reflection of the desired material, which is calculated to be *significantly* stronger than any other reflection, was not observed. The only observed reflections are likely indicative of a molecular species.

In summary, we prepared two electroactive COF precursors based on ketal-protected catechols, but were unable to prepare the desired COFs. In the case of our HATNOH-based precursor, calculations showed that the hexahydroxy tautomer was less energetically favorable than a tautomer favoring keto-based functionality on half of the oxygen atoms. We attempted to block the nitrogen atoms through metal-atom coordination, but were unable to fully decorate **5** with metal atoms and thus unable to access COFs through this strategy. In the case of our

dibenzoTTF-based precursor, we were unable to find a reason for the lack of reactivity and had difficulty accessing the deprotected species.

2.4 Experimental Section
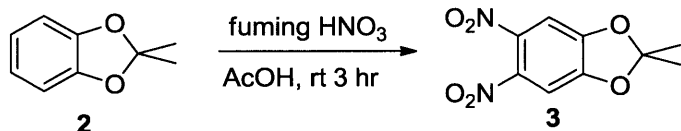
2,2-Dimethyl-5,6-dinitro-1,3-benzodioxole (3). This procedure was adapted from a literature procedure.[53] Compound 2[54] (8.16 g, 54.3 mmol) was dissolved in acetic acid (200 mL) and cooled with an ice bath. To this was added a solution of fuming nitric acid (115 mL) and 70% nitric acid (15 mL) over the course of 30 minutes. The resulting solution was allowed to warm to room temperature and proceed for three hours. The reaction was poured onto ice to generate a yellow precipitate. The mixture was further diluted with water. The precipitate was collected by filtration and dried *in vacuo* to afford **3** as a yellow solid (10.9 g, 45.6 mmol, 84%). ^{1}H NMR (acetone-d_6): δ = 7.54 (s, 2H, Ar*H*), 1.84 (s, 6H, C*H*$_3$).
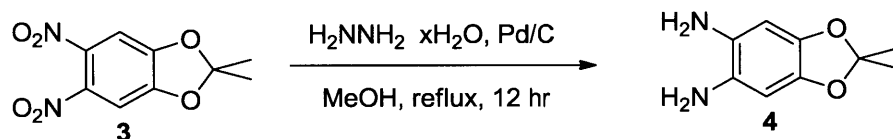
2,2-Dimethyl-5,6-diamino-1,3-benzodioxole (4). This procedure was adapted from a literature procedure.[53] Compound **3** (19.81 g, 82.5 mmol) was dissolved in methanol (350 mL) under N$_2$. To this was added 10% palladium on carbon (825 mg) and hydrazine hydrate (52 mL). The reaction was heated to reflux and allowed to proceed overnight. The reaction mixture quickly turned red. The reaction was cooled to room temperature and filtered through Celite under a N$_2$ atmosphere to remove the catalyst. The filtrate was concentrated to yield **4** as a light brown powder (13.12 g, 72.6 mmol, 88%). ^{1}H NMR (DMSO-d_6): δ = 6.14 (s, 2H, Ar*H*), 4.03 (br s, 4H, N*H*$_2$), 1.51 (s, 6H, C*H*$_3$).
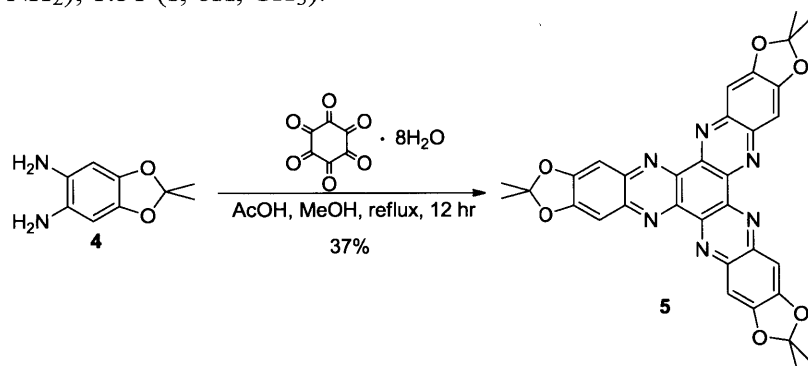
2,2,9,9,16,16-hexamethyl-[1,3]dioxolo[4',5':6,7]quinoxalino[2,3-a][1,3]dioxolo[4',5':6,7]quinoxalino[2,3-c][1,3]dioxolo[4,5-i]phenazine (5).
Hexaketocyclohexane octahydrate (2.34g, 7.49 mmol) and **4** (5.04g, 27.7 mmol) were dissolved in MeOH (200 mL) under N$_2$. To this solution was added degassed acetic acid (20 mL). The reaction was heated to reflux and allowed to proceed overnight to afford a dark yellow precipitate. The reaction was cooled to room temperature and the precipitate was collected by

filtration. After removal of volatiles *in vacuo*, the product was recrystallized from chloroform/hexane. The crystals were collected by filtration and the residual product in the filtrate was also recrystallized from chloroform/hexanes to afford **5** as yellow needles (1.66g, 2.76 mmol, 37%). ^{1}H NMR (CDCl$_3$): δ = 7.78 (s, 6H, ArH), 1.88 (s, 18H, CH_3). ^{13}C NMR (CDCl$_3$): δ = 153.1, 142.9, 140.8, 121.4, 104.9, 26.5.
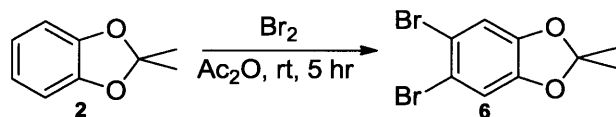
5,6-Dibromo-2,2-dimethylbenzo[*d*][1,3]dioxole (6). This procedure was adapted from a literature procedure.[54] A flask was charged with **2** (16.22g, 108 mmol) and acetic anhydride (20 mL). To this was added bromine (11.6 mL, 225 mmol), dropwise. A white precipitate formed during the addition. After stirring for five hours, the precipitate was collected by filtration to yield **6** a crystalline white powder. The ^{1}H NMR signals are in agreement with reported values.[54]
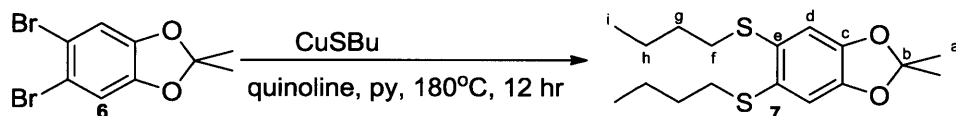
5,6-*bis*(Butylthio)-2,2-dimethylbenzo[*d*][1,3]dioxole (7). This procedure was adapted from a literature procedure.[55] A Schlenk flask was charged with **6** (3.856g, 12.5 mmol), cuprous butanethiolate,[55,56] degassed quinoline (35 mL), and degassed pyridine (10 mL). The reaction mixture was heated to 180°C and allowed to proceed overnight. The reaction was then cooled to 100°C and poured onto HCl in ice water (200 mL). This mixture was stirred for 3 hours. The aqueous mixture was then extracted twice with ether. The organic layers were then combined and poured onto the black, gummy reaction residue. After mixing in an ultrasonic bath for 5 minutes, the mixture was filtered through Celite. The residue was washed twice more with ether and the resulting mixtures were filtered through Celite. The organic layers were combined and washed twice with 1M HCl (100 mL), once with distilled water (100 mL), twice with aqueous ammonia (100 mL), and once with distilled water (100 mL). The organic layer was then dried with magnesium sulfate and concentrated to yield a brown oil. The brown oil was passed through a short silica gel column (5 cm diameter, 6 cm height) in hexanes to give **7** as an orange oil (3.04g, 9.31 mmol, 74%). ^{1}H NMR (CDCl$_3$): δ = 6.76 (s, 2H, ArH), 2.82 (t, 4H, J = 7.4 Hz, SCH_2), 1.67 (s, 6H, C(CH_3)$_2$), 1.62 (m, 4H, SCH$_2$CH_2), 1.45 (m, 4H, CH_2CH$_3$), 0.92 (t, 6H, CH$_2$CH_3, J = 7.3 Hz). ^{13}C NMR (CDCl$_3$): δ = 146.7 (c), 129.5 (e), 118.8 (d), 110.7 (b), 34.3 (f), 31.2 (g), 26.0 (a), 22.2 (h), 13.8 (i).
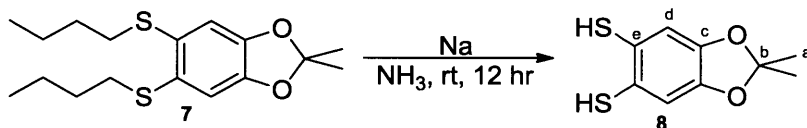
5,6-Dithio-2,2-dimethylbenzo[*d*][1,3]dioxole (8). This procedure was adapted from a literature procedure.[57] A 500 mL 3-necked round bottom flask was equipped with a gas adapter to the Schlenk line, a gas adapter to an ammonia tank, and a dry ice condenser with an outlet to a bubbler filled with mineral oil. The line to the mineral oil was closed off and the system was put under vacuum and then back filled with N$_2$. The condenser and flask were then cooled to -78°C. Ammonia (60 mL) was condensed into the flask. The ammonia outlet was removed and replaced

with a septum. The flask was then charged with **7** (896mg, 2.75mmol). The dry ice bath was replaced with a water bath and the reaction reached reflux. Sodium (350 mg, 11 mmol) was added slowly. Each piece was added once the blue color from the previous piece had disappeared. After the addition of the last piece, the blue color persisted for approximately 15 minutes. Ammonium chloride (1 g, 20 mmol) was added in small portions. Stirring was then stopped and nitrogen was allowed to flow over the reaction for approximately 5 hours. The residue was then dissolved in NaOH in ice water. The aqueous mixture was washed twice with ether. These ether extracts were then discarded. The aqueous layer was then acidified with concentrated HCl until a white precipitate was evident. The aqueous mixture was then extracted with ether. The organic layer was dried with magnesium sulfate and then concentrated to yield **8** as a pale green solid (373 mg, 1.73mmol, 63%). ^{1}H NMR (CDCl$_3$): δ = 6.80 (s, 2H, Ar*H*), 3.67 (s, 2H, S*H*), 1.65 (s, 6H, C*H$_3$*). ^{13}C NMR (CDCl$_3$): δ = 147.2 (c), 122.3 (e), 119.1 (d), 111.7 (b), 25.9 (a).
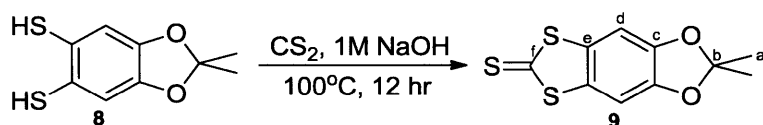
2,2-Dimethyl-[1,3]-dithiolo[4',5':4,5]benzo[1,2-*d*][1,3]dioxole-6-thione (**9**). This procedure was adapted from a literature procedure.[58] Compound **8** (373 mg, 1.74 mmol) was dissolved in degassed 1M NaOH (10 mL). To this was added carbon disulfide (775 mL, 12.8 mmol). The reaction was transferred to a Schlenk flask under N$_2$. The reaction was then heated to reflux and allowed to proceed overnight. The reaction was cooled to room temperature and then stored in the fridge for two days. The precipitate was collected by filtration and dried to afford **9** as a bright yellow solid. ^{1}H NMR (CDCl$_3$): δ = 6.84 (s, 2H, Ar*H*), 1.71 (s, 6H, C*H$_3$*). ^{13}C NMR (CDCl$_3$): δ = 211.5 (f), 148.7 (c), 132.6 (e), 120.4 (d), 101.8 (b), 26.0 (a). Anal. Calcd. for C$_{10}$H$_8$O$_2$S$_3$: C, 46.85; H, 3.15; N, 0.00. Found: C, 46.63; H, 3.28; N, 0.00.
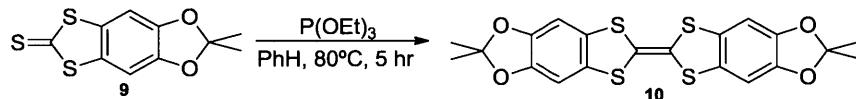
2,2,2',2'-Tetramethyl-6,6'-bi[1,3]dithiolo[4',5':4,5]benzo[1,2-*d*][1,3]dioxolylidene (**10**). This procedure was adapted from a literature procedure.[58] Compound **9** (943 mg, 3.68 mmol) was added to a flask under N$_2$. To this was added anhydrous benzene (25 mL). The mixture was stirred vigorously until the starting material had fully dissolved. Triethylphosphite (5.2 mL, 30 mmol) was added to the reaction mixture, dropwise. The reaction was heated to reflux and allowed to proceed overnight. The reaction was then cooled to room temperature. After allowing the reaction mixture to stand for 10 hr, a yellow crystalline material appeared in the flask. The reaction mixture was refrigerated. The yellow precipitate was collected by filtration. The filtrate was concentrated and the residue was then brought up in methanol, generating a marigold precipitate. This precipitate was collected by filtration and combined with the previously collected precipitate to give **10** as a marigold powder (436 mg, 0.973 mmol, 26%). ^{1}H NMR (C$_6$D$_6$): δ = 6.28 (s, 4H, Ar*H*), 1.27 (s, 12H, C*H$_3$*). ^{13}C NMR (C$_6$D$_6$): δ = 147.5, 119.5, 112.3, 103.3, 100.6, 25.8. Anal. Calcd. for C$_{20}$H$_{16}$O$_4$S$_4$: C, 53.55; H, 3.60. Found: C, 53.51; H, 3.57.
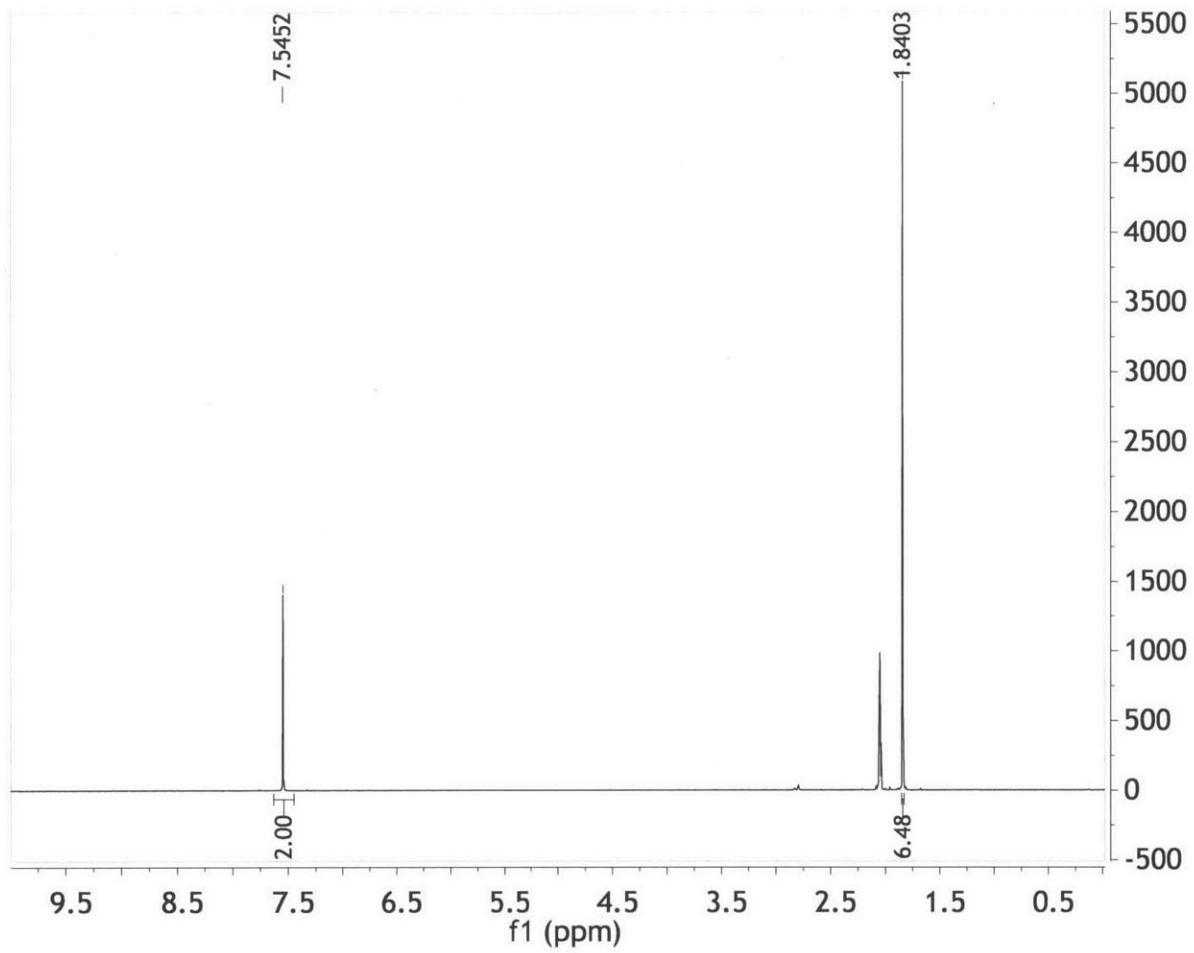
Figure 2.10 ^{1}H NMR of **3** in CDCl$_3$.
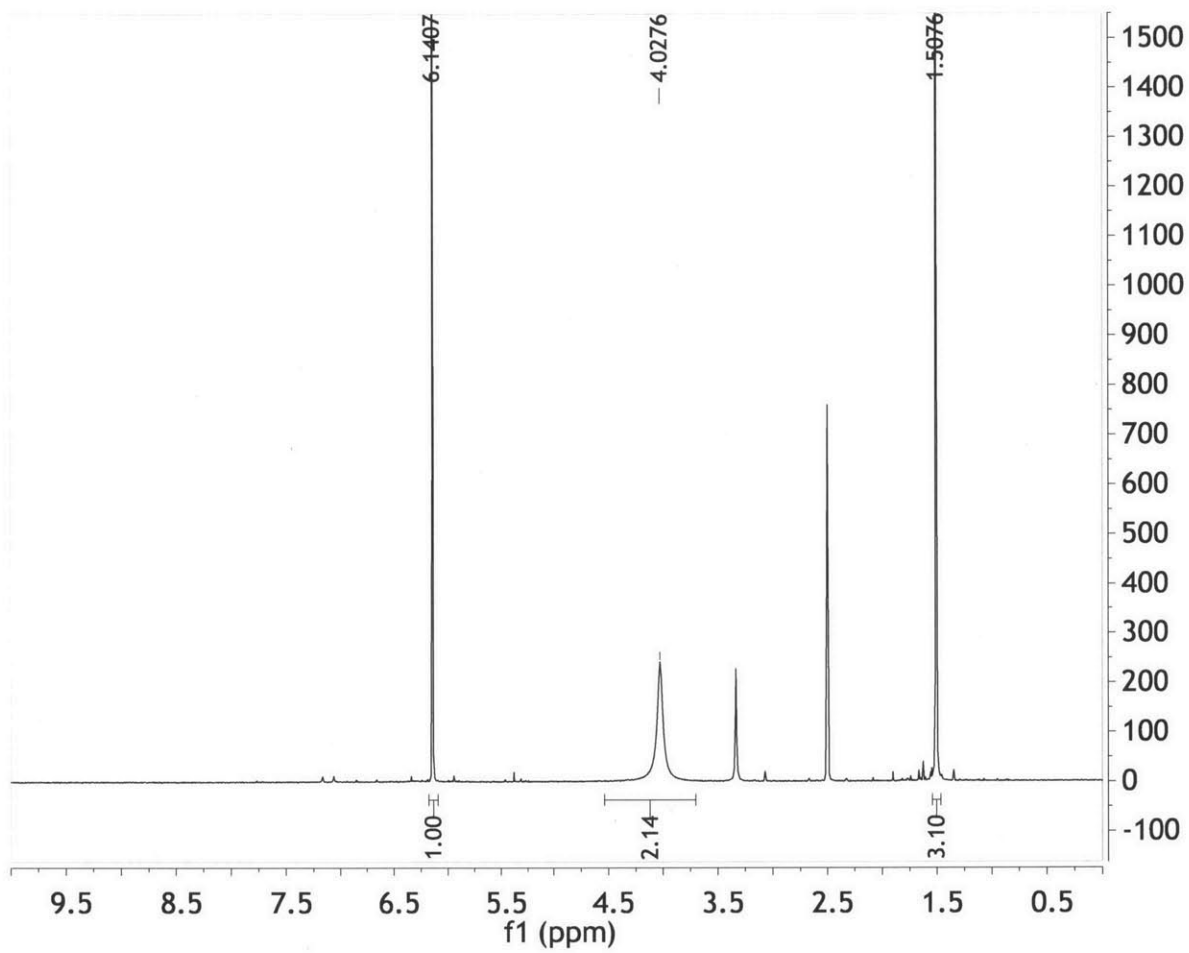
Figure 2.11 ^{1}H NMR of **4** in DMSO-d_6.
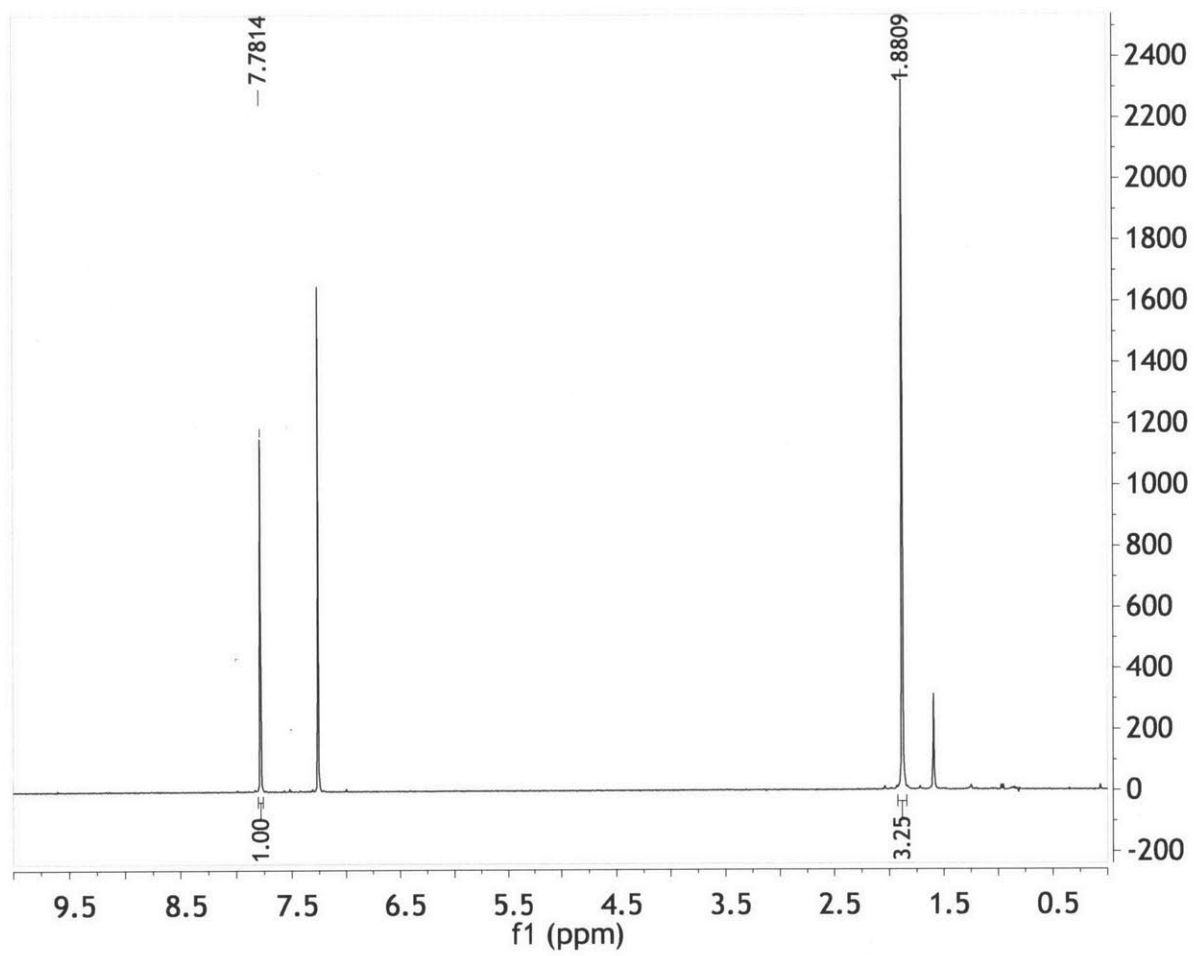
Figure 2.12 ^{1}H NMR of **5** in CDCl$_3$.
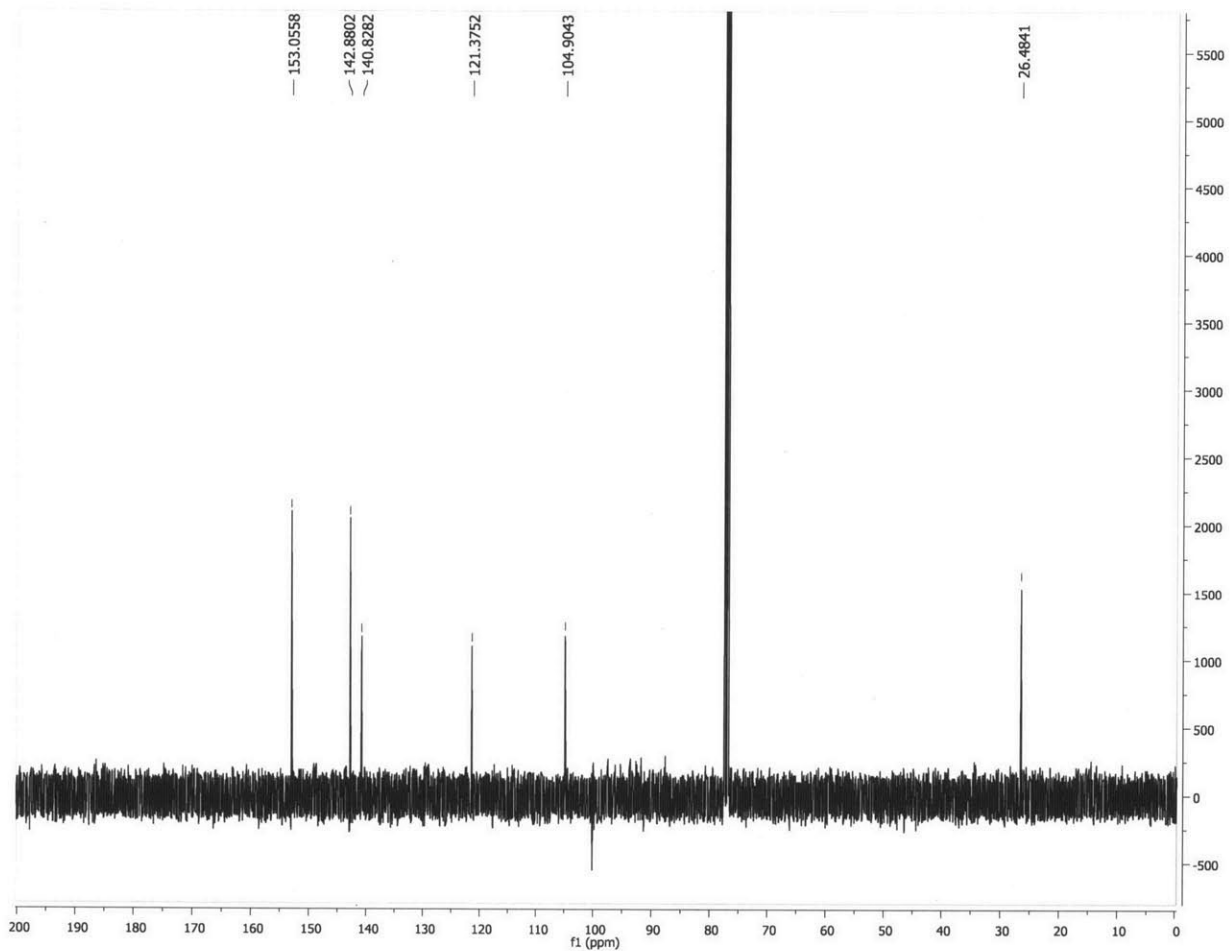
Figure 2.13 ^{13}C NMR of **5** in CDCl$_3$.
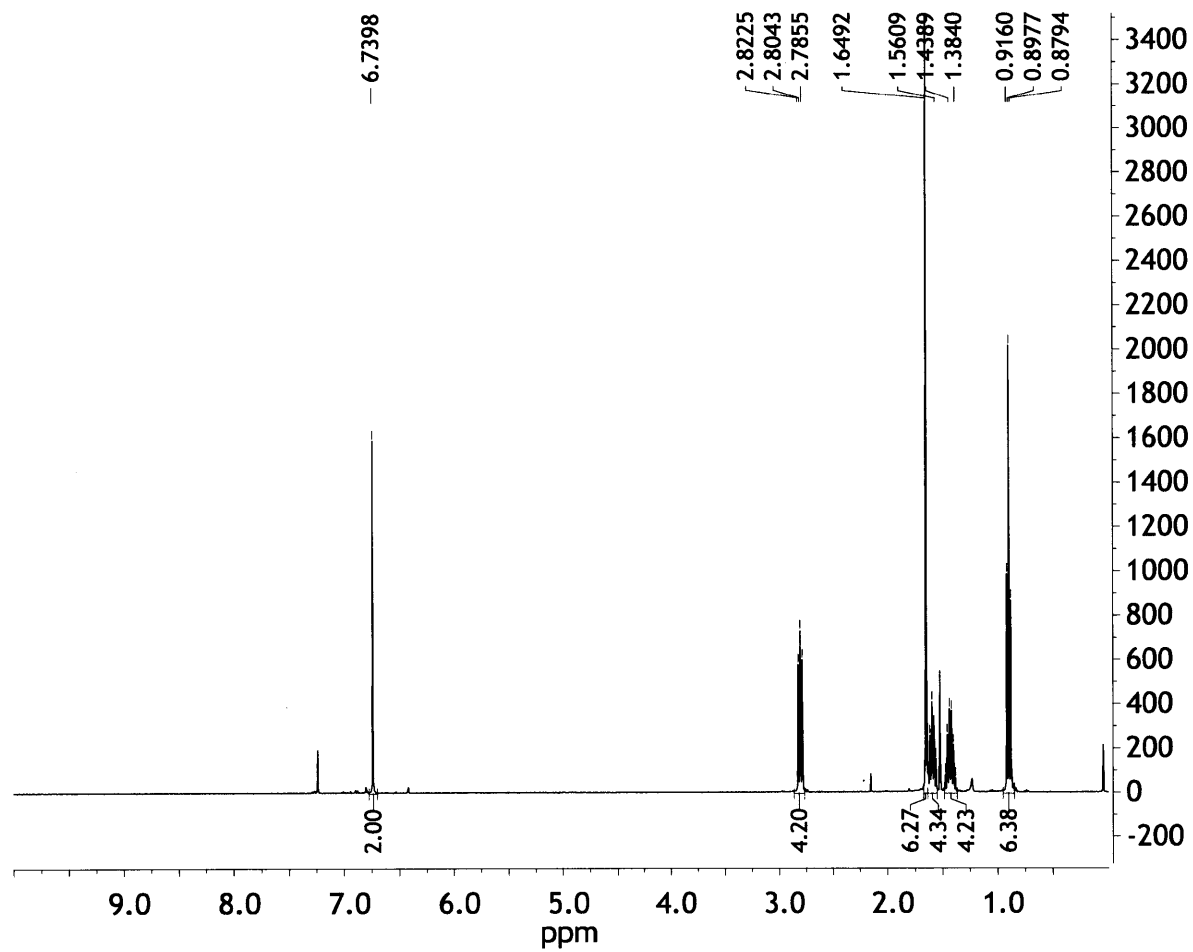
Figure 2.14 ^{1}H NMR of **7** in CDCl$_3$.
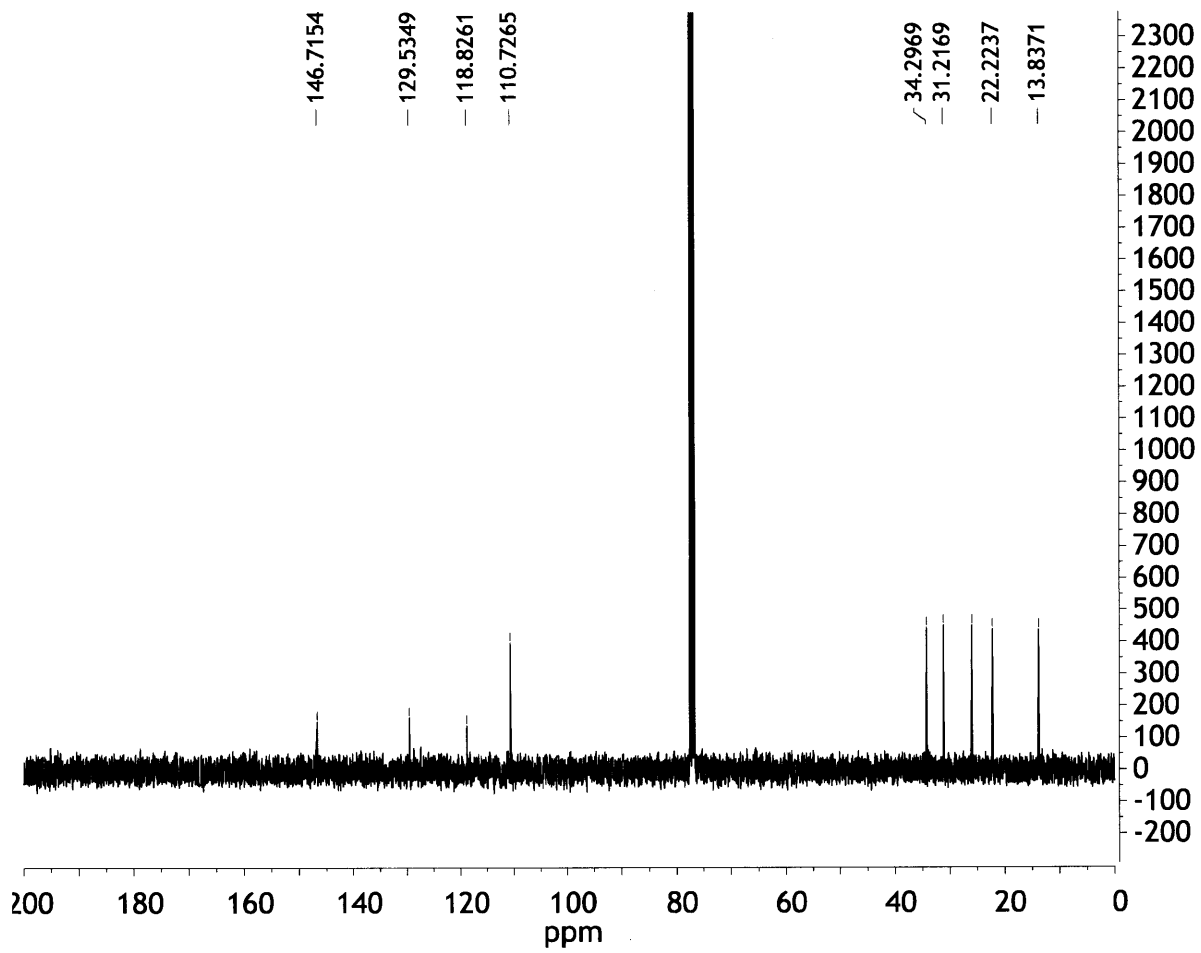
Figure 2.15 ^{13}C NMR of **7** in CDCl$_3$.
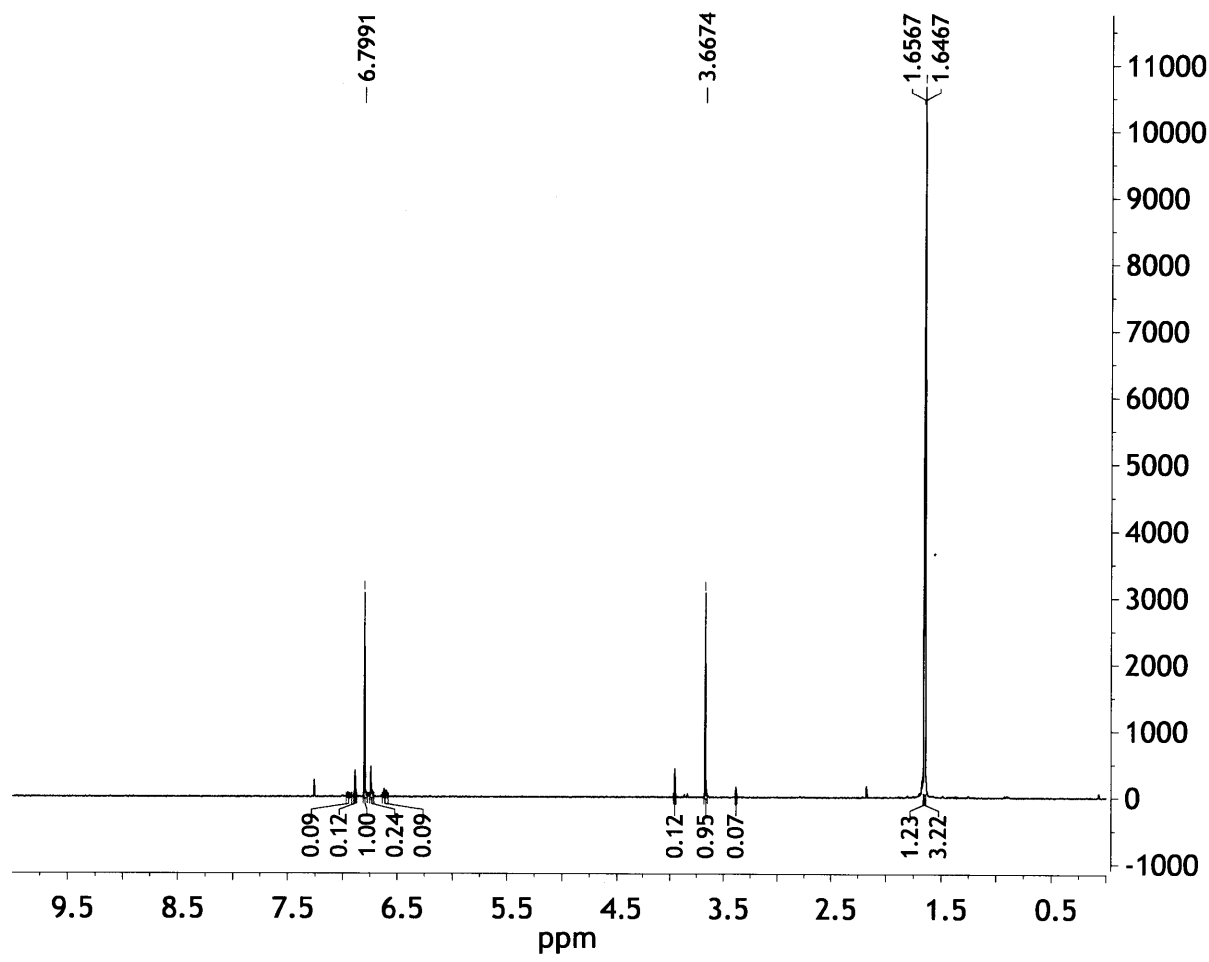
Figure 2.16 ^{1}H NMR of **8** in CDCl$_3$.
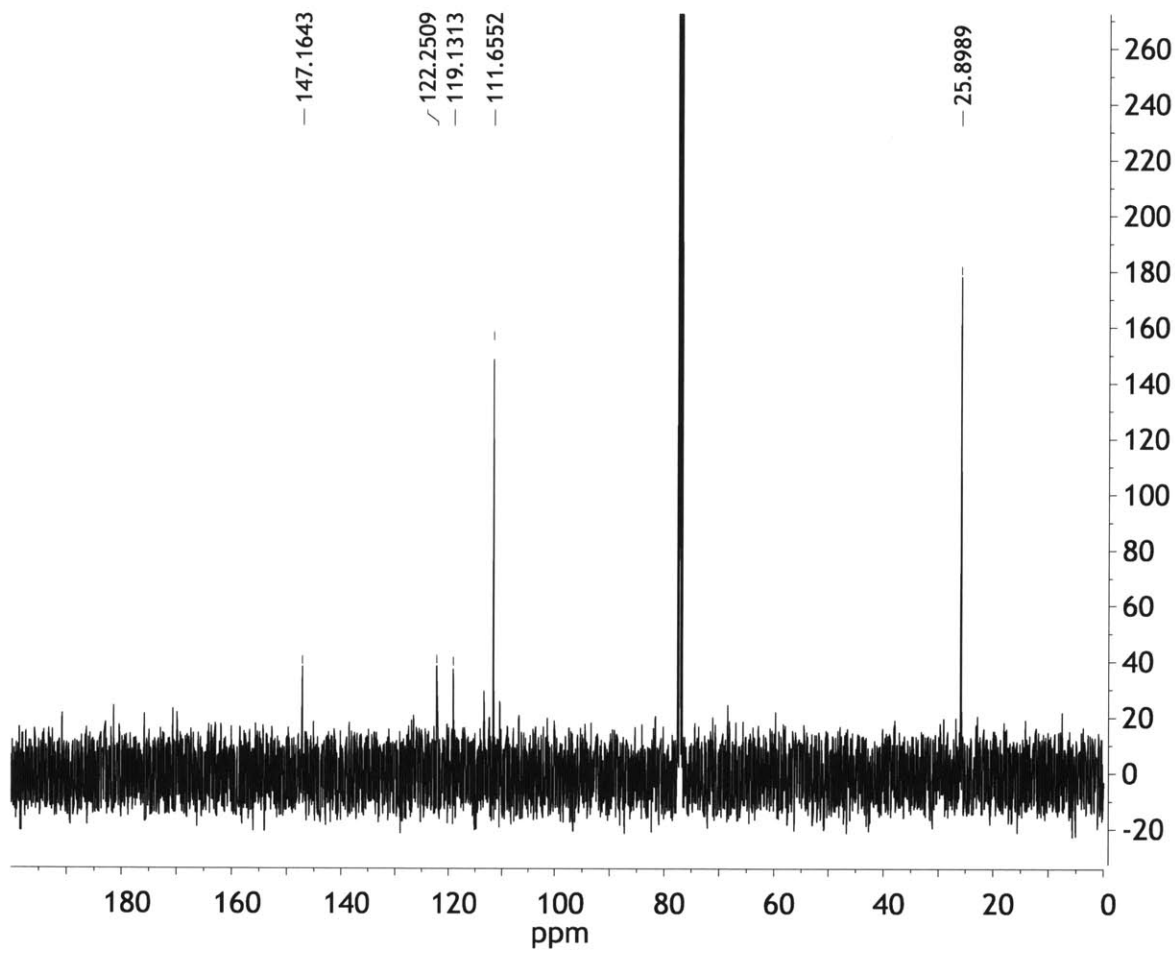
Figure 2.17 ^{13}C NMR of **8** in CDCl$_3$.
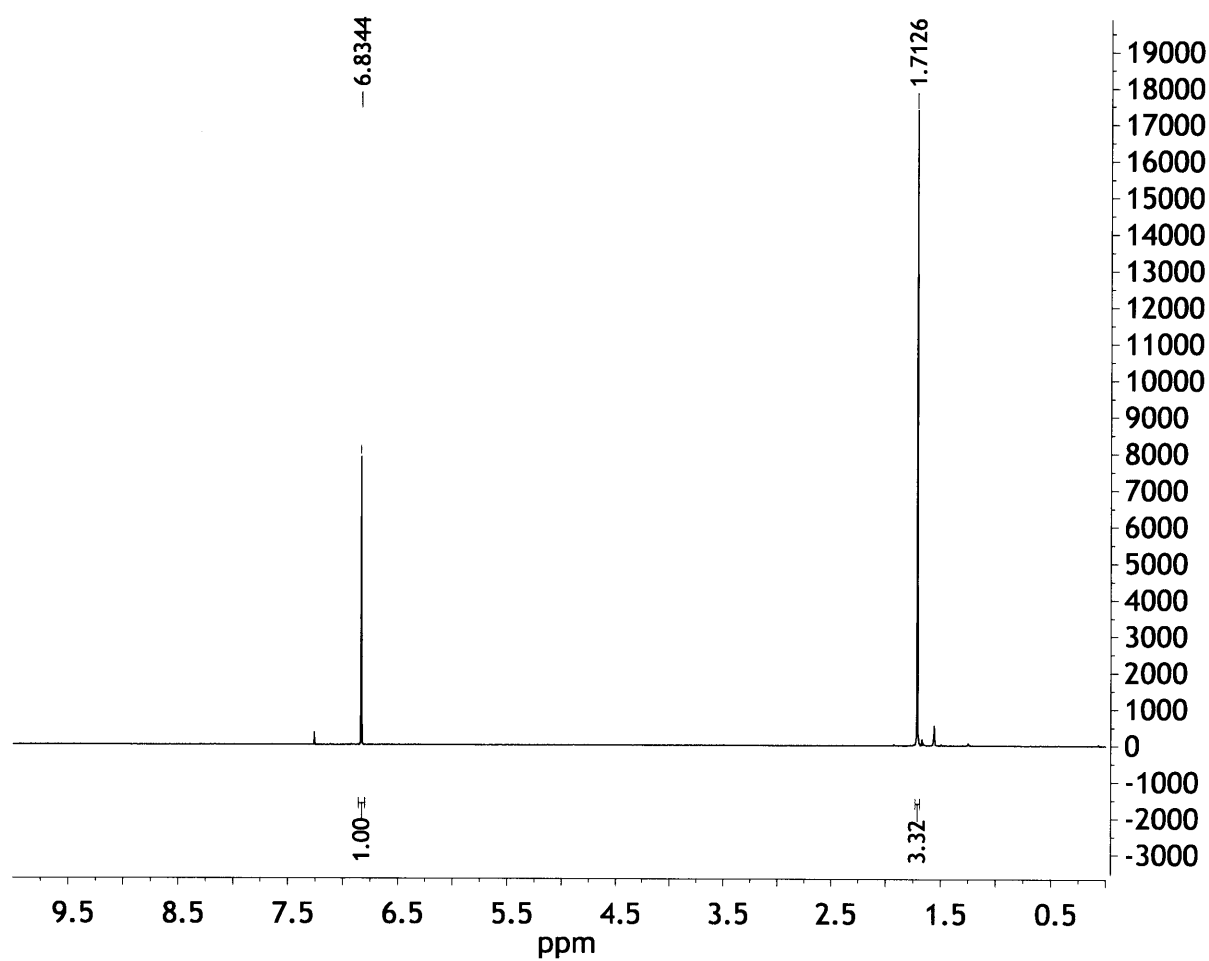
Figure 2.18 ^{1}H NMR of **9** in CDCl$_3$.
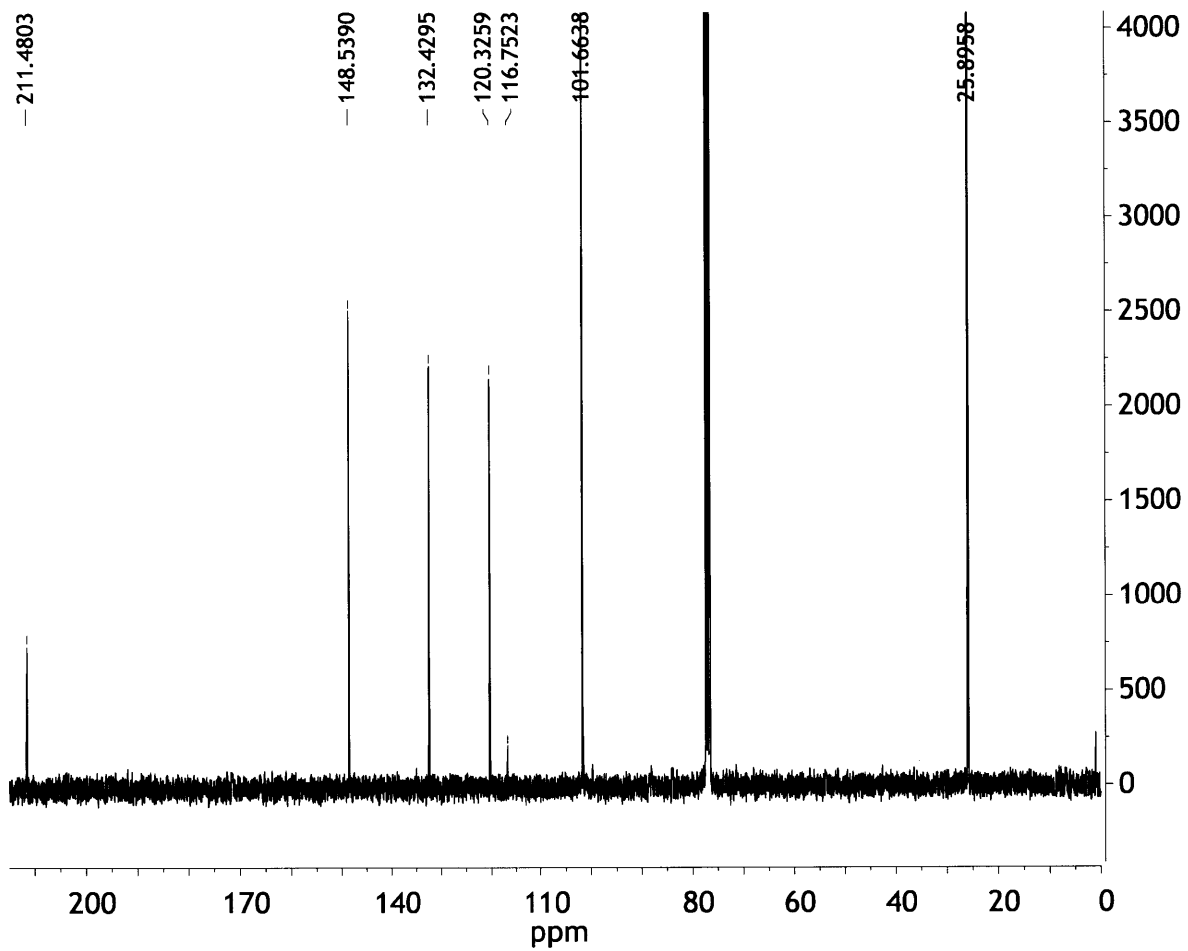
Figure 2.19 ^{13}C NMR of **9** in CDCl$_3$.
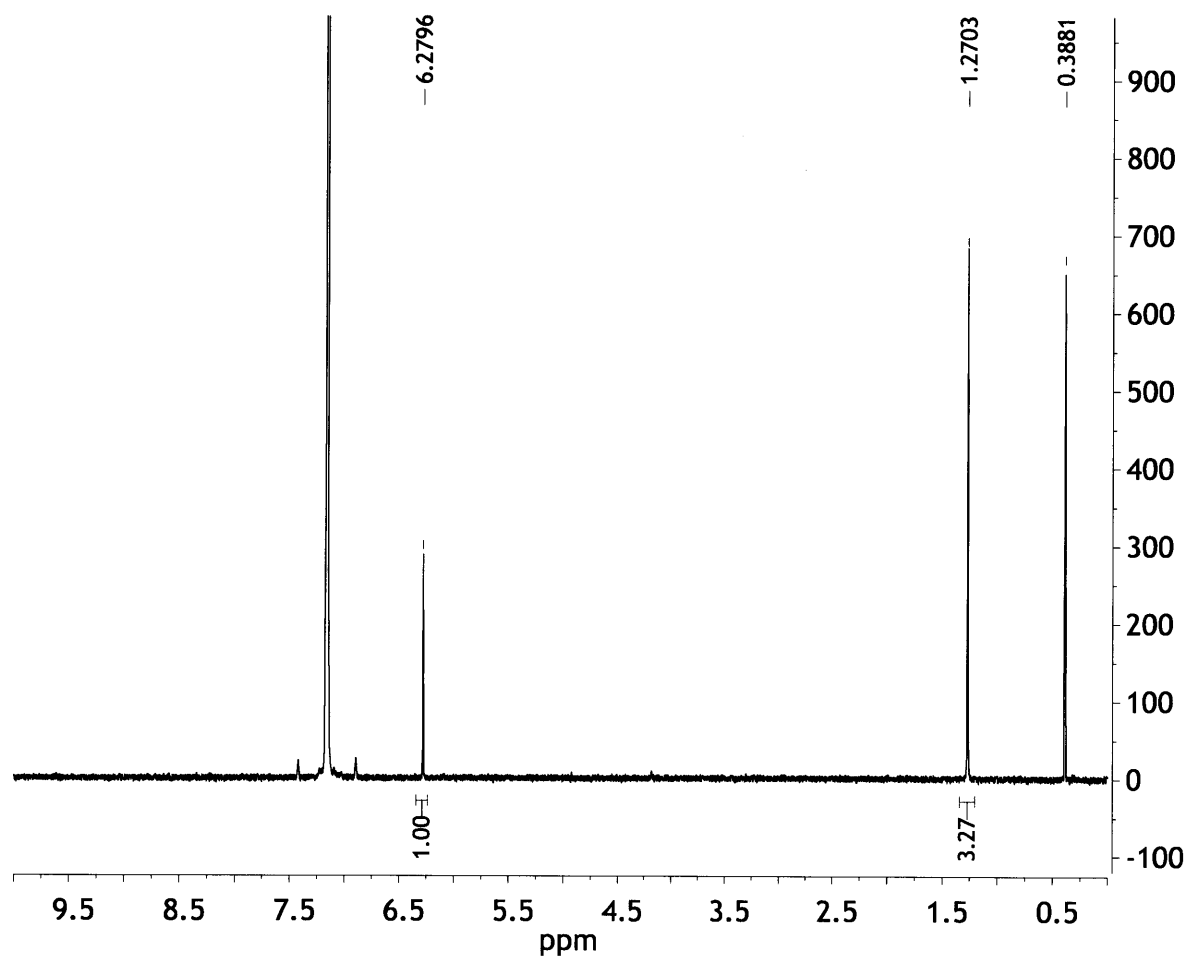
Figure 2.20 ^{1}H NMR of **10** in C_6D_6.
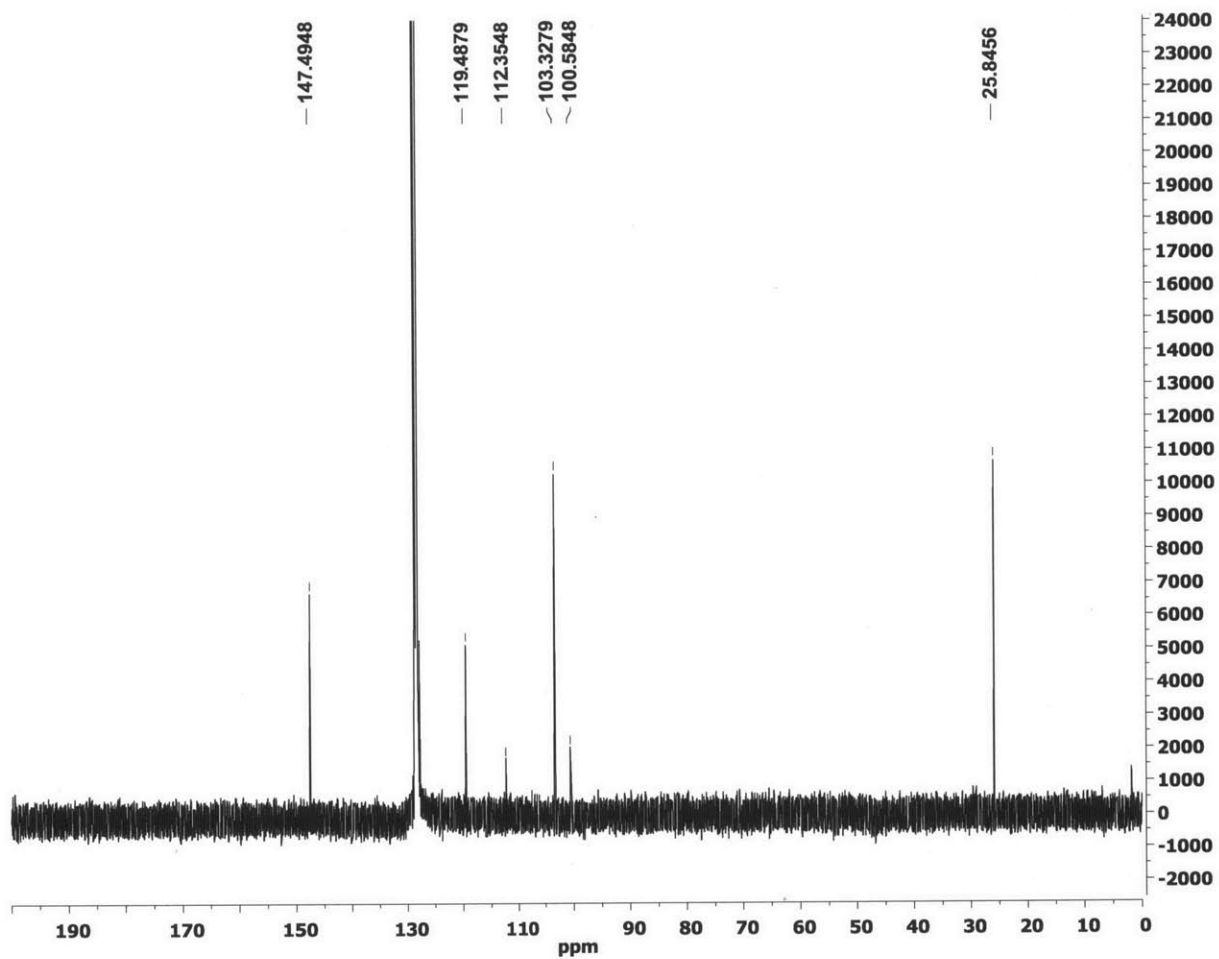
Figure 2.21 ^{13}C NMR of **10** in C$_6$D$_6$.

Table 2.2 Crystal data and structure refinement parameters for **5·(CHCl₃)₃**

empirical formula	$C_{36}H_{27}Cl_9N_6O_6$
formula weight	958.69
Temperature/K	100(2)
λ/Å	0.71073
crystal dimensions/mm³	0.10 x 0.10 x 0.20
crystal system	Monoclinic
space group	$P2_1/c$
a/Å	11.909(1)
b/Å	5.9377(5)
c/Å	56.694(5)
α/°	90
β/°	94.768(2)
γ/°	90
V/Å³	3995.1(6)
Z	4
ρ calcd/mg·m⁻³	1.594
μ/mm⁻¹	0.685
F(000)	1944
θ range collected	2.87 to 26.41
limiting indices	$-14 \leq h \leq 14$
	$-7 \leq k \leq 7$
	$-70- \leq l \leq 69$
Completeness to θ	0.997
Reflections collected/unique	8189/5098
min and max transmission	0.8751 and 0.9346
data/restraints/parameters	8189/622/0
R(int)	0.1094
goodness-of-fit on F²	1.018
Final R indices [I>2σ(I)]	$R_1 = 0.1046$
	$wR_2 = 0.1187$
R indices (all data)	$R_1 = 0.0526$
	$wR_2 = 0.1010$
largest diff. peak and hole	-0.391 and 0.506

Table 2.3 Crystal data and structure refinement parameters for **5·(CHCl₃)₂(C₄H₈O₂)**

empirical formula	$C_{25.71}H_{16}Cl_{3.15}N_4O_{5.33}$
formula weight	577.91
Temperature/K	100
$\lambda/Å$	0.71073
crystal dimensions/mm^3	0.1 x 0.1 x 0.2
crystal system	Monoclinic
space group	$P2_1/n$
a/Å	13.508(1)
b/Å	10.412(1)
c/Å	27.740(3)
$\alpha/°$	90
$\beta/°$	95.858(2)
$\gamma/°$	90
V/Å^3	3881.2(6)
Z	6
ρ calcd/mg·m^{-3}	1.484
μ/mm^{-1}	0.416
F(000)	1767
θ range collected	2.45 to 26.91
limiting indices	$-15 \leq h \leq 15$
	$-11 \leq k \leq 111$
	$-31 \leq h \leq 31$
Completeness to θ	1.000
Reflections collected/unique	53364
min and max transmission	5965
data/restraints/parameters	5965/598/2
R(int)	0.0775
goodness-of-fit on F^2	1.047
Final R indices [I>2σ(I)]	$R_1 = 0.1299$
	$wR_2 = 0.2711$
R indices (all data)	$R_1 = 0.0915$
	$wR_2 = 0.2381$
largest diff. peak and hole	-0.749 and 0.715

Chapter 3. Towards Conductive Metal-Organic Frameworks

3.1 Introduction

Metal-organic frameworks (MOFs) are materials comprised of an inorganic node – potentially a single metal atom but typically a cluster – joined together by an organic ligand through one of any number of functional groups including carboxylates,[59] azoles,[60] sulfonates, phosphonates,[61,62] and amines. The reversibility of the coordinative linkage generally allows for the synthesis of relatively homogeneous, crystalline materials. These materials can contain large pores that are typically filled with solvent molecules used during synthesis. In certain cases, the solvent molecules can be removed,[63,64] leaving behind a (poly)crystalline, porous network that can demonstrate porosities upwards of 4500 m^2/g.[65–69] The strong coordinative bonds between metal and ligand help to maintain a rigid network capable of withstanding the driving force towards collapse. Partly for this reason, the most common ligand motif seen in the literature is the use of aryl rings to provide structural rigidity. The resulting network is frequently employed as a medium for gas storage,[70–72] gas separation,[73] and catalysis.[74,75] Ligands used in MOFs are not chosen for their electronic properties, leading to choices such as terephthalic acid. This compound has two highly anionic oxygen atoms on either end that are far more electronegative than typically employed metal atoms, thus resulting in very poor electronic communication.

Much like the case of COFs, the electronic properties of MOFs are only now coming under study. One of the first reports of a porous, crystalline, potentially conductive material was that of Fe^{III}(OH)(bdc) (bdc = benzene-1,4-dicarboxylate).[76] Rather than containing a redox-active ligand, this MOF contains a one-dimensional Fe-O-Fe chain that is the presumed path for conductivity. When Fe^{III}(OH)(bdc) is mixed with carbon black, the resulting composite displays non-negligible energy storage potential for lithium ions. While electrical and ionic conductivity are implicated, they are not shown explicitly. It is unlikely that this system exhibits electronic conductivity since the mixed valence variant of this MOF, in which some of the iron atoms are reduced to Fe^{II}, appears to be an electronically localized system, with discrete signals for Fe^{II} and Fe^{III} species. A system displaying conductivity is likely to exhibit at least some delocalization of electron density.

More pertinent studies of electronic properties of MOFs have been reported recently using metal dithiolene systems bridged through pyrazine units.[77,78] The compounds chosen, nickel and copper (pyrazinedithiolate) (Ni(pdt)⁻ and Cu(pdt)⁻) utilize the connectivity of the pyrazine unit to bind copper(I) centers to generate a cubic lattice. This framework type offers two potential avenues for conduction. In the first scenario, an electron can hop from one highly electroactive metal dithiolene unit to another, much like the typical pathway for conduction implicated in organic systems. In the second scenario, conduction can occur through the pyrazine-metal bond. Systems such as the Creutz-Taube ion exhibit significant electronic delocalization through a pyrazine unit, so this pathway is viable for electron transport.[79] There have been no studies into the nature of conduction in these materials, so it is not possible to ascertain the conduction pathway at the present.

We hoped to capitalize on the advantages of both COFs and MOFs to obtain a material that derives its conductivity through an organic π system typical of COFs, while using the higher crystallinity and coordinative immobilization of MOFs. As our organic core, we decided to use tetrathiafulvalene (TTF). As described earlier, TTF is a highly electroactive molecule that can undergo two reversible oxidations and whose charge transfer salts often exhibit high

conductivities and charge mobilities. The TTF system is particularly attractive because of its well-developed synthetic chemistry that allows for tuning of the ligand to achieve optimal properties.[80–82] There have been attempts to control the supramolecular structure of TTF-based materials while retaining conductivity such as through N···I (N lone pair donation to C-I σ*) interactions,[83] coordination to metal ions through thioalkyl groups,[84] and carboxylates directly appended onto the TTF core,[85] but none of these materials has demonstrated both conductivity and porosity.

By appending benzoate spacers onto the TTF core, we hoped to achieve columnar stacking of TTF that were spaced apart by phenyl groups to generate a porous structure possessing conductivity. TTF tetracarboxylate-based materials have been shown to self-assemble with alkali cations to form stacks of TTF units separated by alkali metal cations.[85] The possibility of metal-carboxylate interactions to arrange TTF in a stacking motif inspired us to look to extended system to maintain π stacking while introducing new functionality into the material. Herein we show that we can generate materials from TTF tetrabenzoic acid (H_4TTFTB) and metal nitrates that exhibit stacking of the TTF cores and employ the benzoate arms to delineate pores that persist upon evacuation of solvent.

3.2 Synthesis and Structural Characterization

We were able to access the ligand H_4TTFTB in two steps with a palladium catalyzed cross coupling between TTF and ethyl 4-bromobenzoate[86] followed by saponification[87] as shown in Scheme 3. Treatment of a solution of H_4TTFTB in 3:1 DMF/EtOH with a solution of $M(NO_3)_2 \cdot xH_2O$ [M = Zn (**11**), Co (**12**), Mn (**13**)] in 1:1 EtOH/H_2O followed by heating at 75°C for two days afforded the M_2TTFTB materials as dark red needles suitable for single crystal X-ray diffraction. These reaction conditions were adapted from a previous report on tetradentate ligand-based MOFs.[88,89]

Scheme 3.1 Synthetic pathway for M_2TTFTB
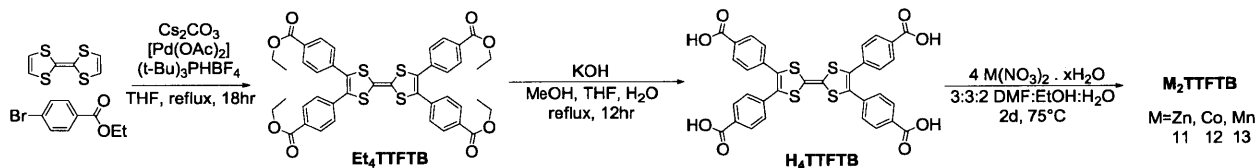
The three MOFs form an isomorphic series, as depicted in Figure 3.1, comprised of helical chains of corner sharing pseudo-octahedra joined together by TTFTB^{4-}. The benzoate groups act as spacers to delineate nearly cylindrical pores. The structure of **11** is described here, but a similar description is appropriate for both **12** and **13**. Compound **11** crystallized in the $P6_5$ space group with a racemic twinning domain. The screw axis is slightly offset from the central ethylene unit of the TTF core of TTFTB^{4-}. Thus, adjacent TTF units are rotated by 60° relative to one another and translated by 3.47 Å. The approximate plane through the TTF core is not perpendicular to the screw axis, which results in just one relatively close S···S contact of 3.81 Å. This distance is within the range of S···S distances in some other highly conducting derivatives such as TTF-(7,7',8,8'-tetracyanoquinodimethane) (3.75 Å),[90] TTF$_3$Cl (3.60 Å),[91] TTF-dicyanoquinodiimine (3.69 Å),[92] and TTF-di(methylthio)dicyanoquinodiimine (3.83 Å).[93]
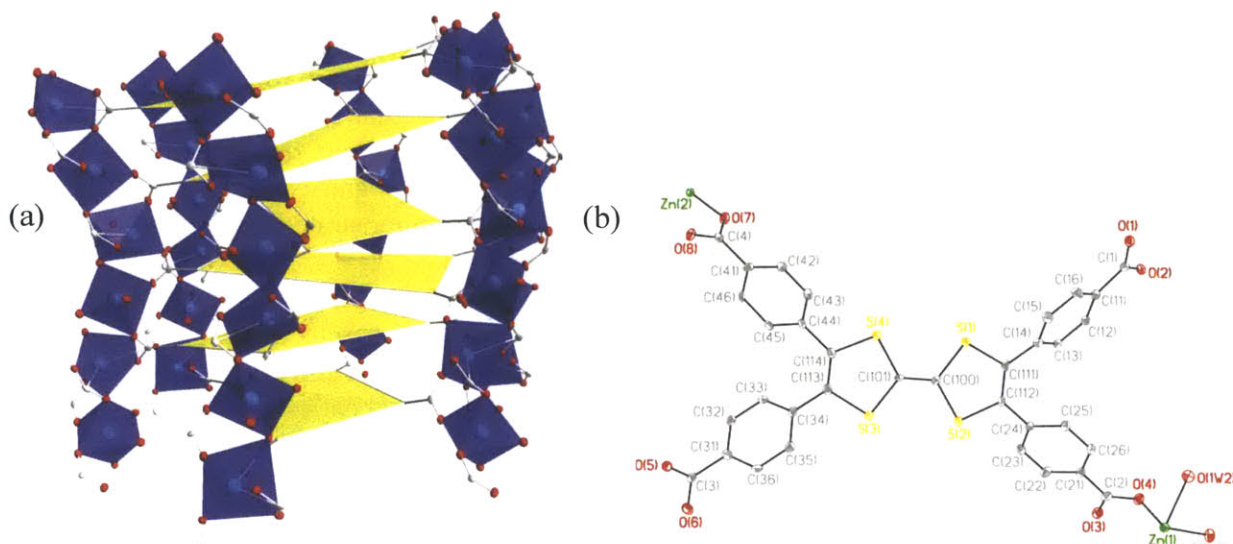
Figure 3.1 (a) Overall structure of **11-13**. Blue polyhedral represent the metal in an oxygen coordination sphere and yellow sheets represent TTFTB^{4-}. (b) ORTEP of **11**.

The two dithiole rings are slightly twisted with respect to each other, with dihedral angles of the *cis* sulfur atoms of 2.32° and 2.35°. The entire TTF unit is slightly puckered, with dihedral angles of the *trans* sulfur atoms of 176.9(1)° and 178.5(1)°. The phenyl rings exhibit a significant twist from the TTF core with dihedral angles between 40° and 52°.

The helical M-O chains consist of an asymmetric unit of two metal units, each of which exhibits a pseudo-octahedral coordination sphere of oxygen atoms bridged by κ^1, κ^1 and κ^1,κ^2 carboxylates. Zn1 contains Zn-O bonds in the range 2.053-2.168 Å and O-Zn1-O angles ranging from 84.9(1)° to 97.5(1)°. The coordination sphere comprises two *cis*-coordinates water molecules and four carboxylate oxygen atoms. The other metal center, Zn2, exhibits a pronounced deviation from an ideal octahedral geometry, as there are four short Zn2-O contacts between 1.947 and 2.035 Å and two significantly longer interactions arranged in a *cis* fashion corresponding to κ^2 carboxylate oxygen atoms with distances of 2.330 and 2.728 Å. Zn2 coordinates chelating carboxylates with a relatively small bite angle, so there is a large distribution of O-Zn2-O angles, ranging from 53.4(1)° to 110.1(1)°.

3.3 Porosity Analysis

The pores are filled with DMF and ethanol molecules that can be located in the solid state structure as well as water molecules coordinating to the metal ion. Thermogravimetric analysis (TGA) of the three MOFs, shown in Figure 3.2, indicates two main steps of mass loss – one step before 200°C and one step above 400°C. The TGA profiles of **11** and **12** exhibit a sharp mass loss between approximately 100°C and 140°C while **13** exhibits a much shallower decline in mass. TGA of **11** showed a 28.3% solvent loss, approximately corresponding to 3.5 molecules of DMF and water (28.2%). There are 1.5 more molecules of DMF than calculated from the elemental analysis, because the samples were removed from the mother liquor and allowed to dry on filter paper, rather than being washed with ethanol. TGA of **12** showed a 19.3% solvent loss, corresponding to 1.75 DMF molecules and 4 water molecules (20.0%), as indicated by elemental analysis. TGA of **13** showed a 12.5% solvent loss, approximately corresponding to 0.7 molecules of DMF and 3.75 molecules of water (13.0%). In calculating these numbers, the initial

mass loss near room temperature was attributed to surface solvent loss and thus not considered in the mass percent calculation. This process allowed for better agreement with the elemental analysis results. Compounds **11-13** exhibit a large plateau of thermal stability above 180°C until the final decomposition point upwards of 400°C. Using this information, the three structures were evacuated at 200°C and 4 mmHg for 12 hours. Elemental analysis of these materials indicated complete removal of solvent and PXRD indicated that the phases retained crystallinity. A space-filling model shows the pores to be approximately 5 Å in diameter.
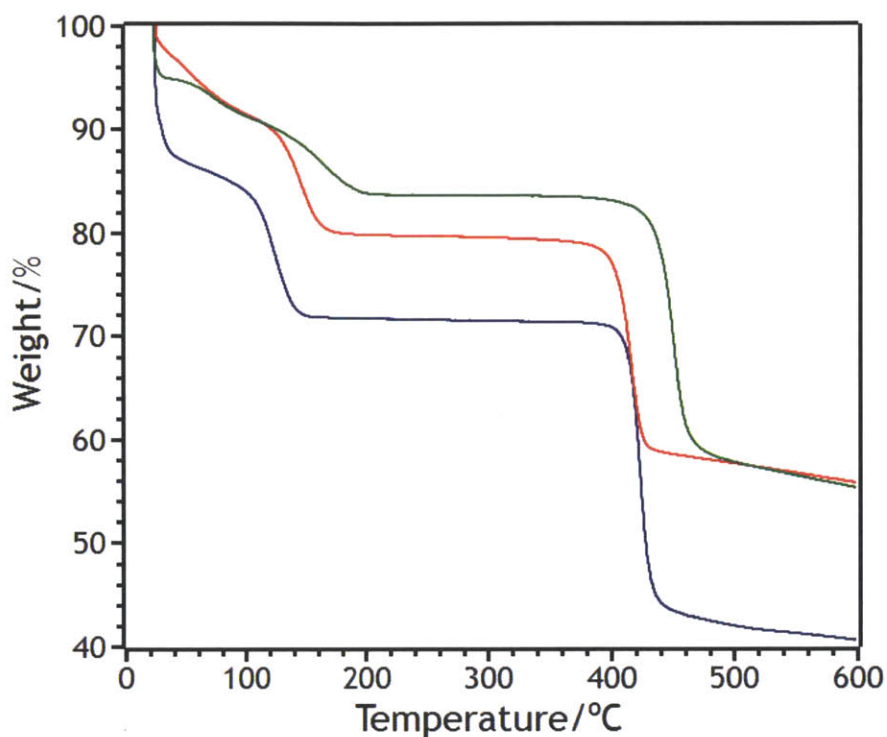
Figure 3.2 TGA profiles of **11** (blue), **12** (red), and **13** (green). Profiles were acquired at 1 °C/min.

Nitrogen sorption isotherms of the desolvated **11-13** at 77K, shown in Figure 3.3, can be classified as Type I isotherms indicating microporous nature. BET analysis of the isotherms gave surface areas of 662(2), 676(3), and 601(3) cm^2/g for **11**, **12**, and **13**, respectively. These surface areas are significantly greater than those of previously studied porous, conductive, ordered materials. Using a cylindrical pore model, Tarazona non-local density functional theory (TNLDFT) indicated a pore distribution with a very sharp peak at 6 Å, which is similar to the pore size calculated from a space filling model.[94] The calculated fits from the TNLDFT treatment, shown in Figure 3.3a, are in excellent agreement with the measured isotherms. These pores offer channels for the introduction of small molecules.
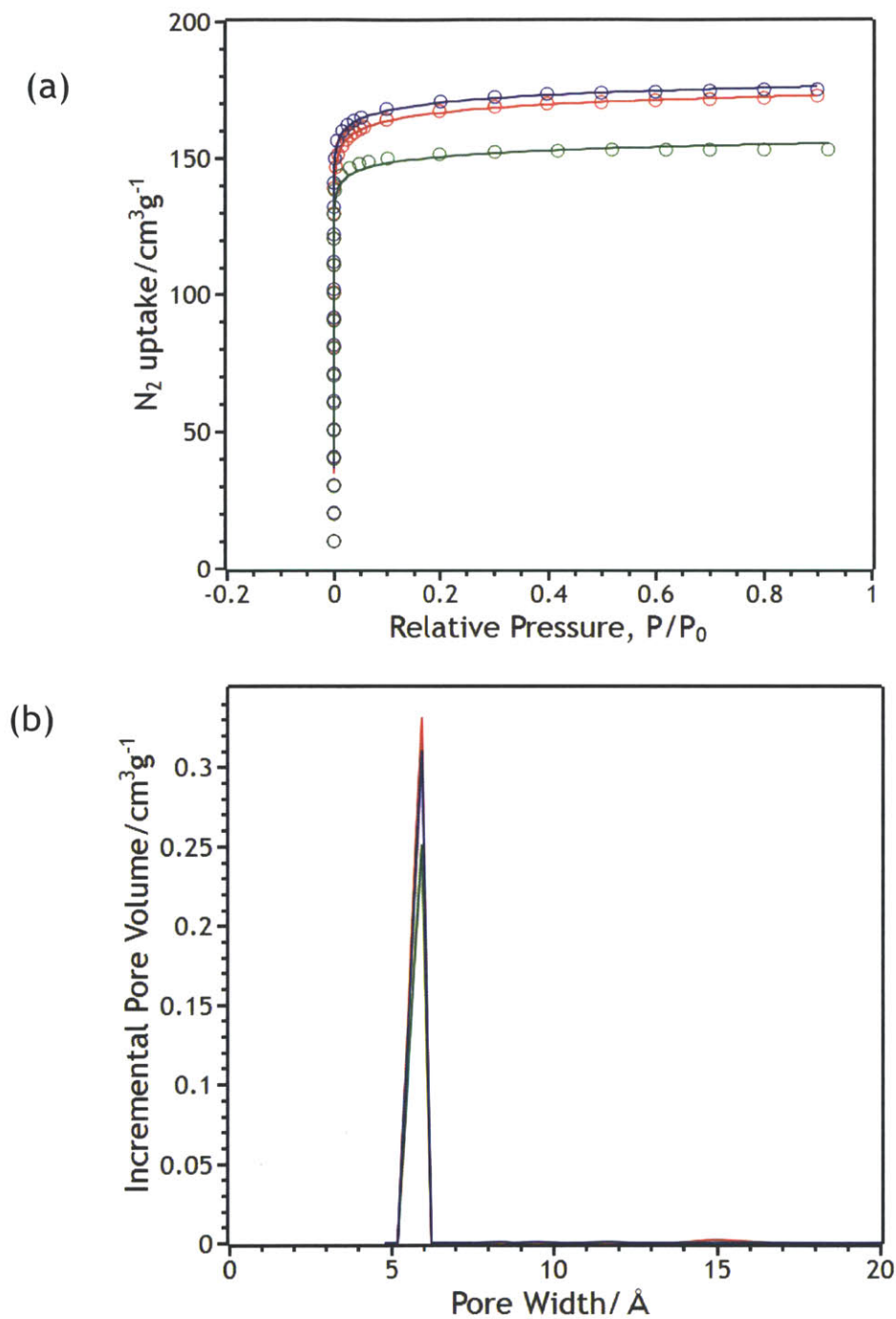
Figure 3.3 (a) N_2 isotherms collected at 77K for **11** (red), **12** (blue), and **13** (green). The corresponding BET surface areas are 662(2), 676(3), and 601(3) cm^2/g for **11**, **12**, and **13**, respectively. The fits for each material gave $C = -8189$ and a correlation coefficient of 0.9999730; $C = 49342$ and a correlation coefficient of 0.9999319; $C = 74139$ and a correlation coefficient of 0.9999121 for **11**, **12**, and **13**, respectively. (b) The pore size distributions of **11** (red), **12** (blue), and **13** (green) as calculated by the Tarazona non-local density functional theory method implemented in the ASAP 2020 software provided by Micromeritics.

3.4 Electrochemical Characterization
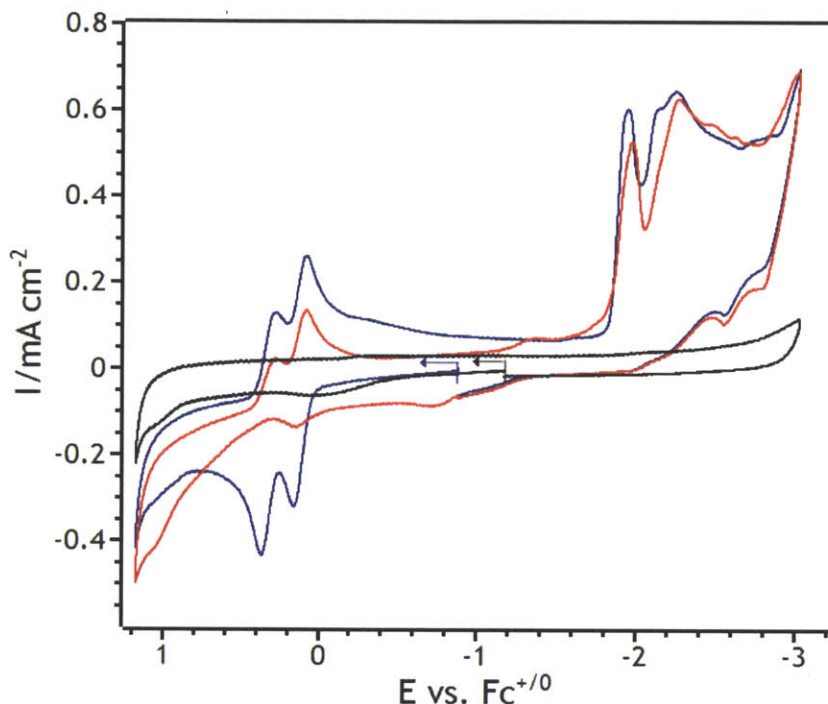
Figure 3.4 Cyclic voltammogram of H_4TTFTB in 0.1 M $TBAPF_6$ in DMF with a glassy carbon button working electrode, Ag/Ag(cryptand) reference electrode, and platinum wire counter electrode. Traces shown are the blank (black), first scan (blue), and second scan (red).

We then hoped to electrochemically characterize H_4TTFTB to determine if the ligand maintained the electroactivity of the TTF core. A solution cyclic voltammogram (CV) of H_4TTFTB in a 0.1 M solution of tetra-*n*-butylammonium hexafluorophosphate in DMF with a glassy carbon button working electrode, silver/silver(cryptand) reference electrode, and platinum wire reference is shown in Figure 3.4. The CV shows two reversible oxidation waves at $E_{1/2,ox1} = 118$ mV and $E_{1/2,ox2} = 320$ mV vs. $Fc^{0/+}$. Scanning further in the negative region, as seen in Figure 3.4, shows a number of irreversible cathodic features that likely stem from ligand decomposition as evidenced by the very small return oxidation wave in the second scan. The first oxidation wave is approximately 170 mV positively shifted from TTF due to the electron-withdrawing benzoate moieties.[95] The second wave is nearly identical for H_4TTFTB and TTF.

After acquiring a CV of H_4TTFTB, we moved towards electrochemically characterizing **11-13**. In order to do so, we scanned a variety of electrodes, solvents, and electrolytes based on previous reports on the electrochemistry of solids. The conditions studied are documented in Table 3.1. None of the attempted methods yielded an informative CV. In the scenario that an electrochemical response was observed, the solution was observed to slightly yellow over time; this is indicative of H_4TTFTB leaching into solution.

Electrode	Solvent	Electrolyte
Glassy carbon button	MeCN	TBAPF$_6$
Platinum button	DMF	TBAP
Gold button	Propylene carbonate	TEABF$_4$
FTO	DMSO	LiClO$_4$
Carbon paste	DCM	NaPF$_6$

Table 3.1 Conditions attempted to acquire solid state CV. Nearly all permutations were attempted.

3.5 Spectroscopic Characterization

Due to the difficulty in obtaining a CV of **11-13**, we assumed that the voltammetric response was similar to that of the ligand. Iodine can easily singly oxidize TTF but is unable to oxidize TTF$^+$, so we reasoned that iodine would at most singly oxidize H$_4$TTFTB due to the similar potential of the second oxidation of both TTF and H$_4$TTFTB.[96] Treatment of H$_4$TTFTB with a large excess of iodine in ethanol afforded H$_4$TTFTBI$_3$ as a green powder after extensive washing with hexanes. Elemental analysis indicated a slight amount of remaining iodine and room temperature EPR spectroscopy give a signal centered at $g = 2.006$, as seen in Figure 3.5. Organic radicals – TTF radicals in particular – exhibit EPR signals in a very similar location suggesting that the observed species is very likely a TTF-centered radical.[97] Some samples of as-synthesized **11** show similar sharp signals at $g = 2.006$, indicating the sample was doped during synthesis. The sharpness of the signal is likely caused by the coordinative immobilization in the MOF lattice that generates a fairly uniform environment for each TTF core as opposed to the random orientations present in solid H$_4$TTFTB. In the case of **12**, **13**, and undoped **11**, we immersed both crystals and powders in dichloromethane solutions of iodine for 12 hours to afford significantly darker colored materials that were presumably partially doped as triiodide salts. EPR spectra of **11** prepared by these conditions matched those of **11** doped during MOF synthesis. The EPR spectra of **12** and **13** showed sharp signals at $g = 2.004$ superposed on very broad signals with $g = 2$ observed in the undoped materials corresponding to the unpaired electrons localized on the metal centers.
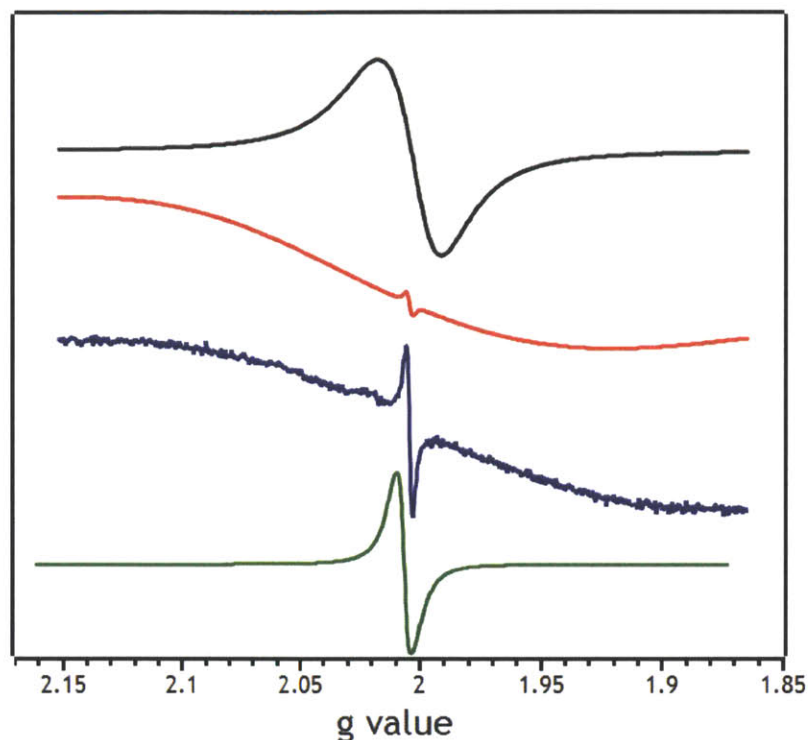
Figure 3.5 Solid state EPR spectra of $H_4TTFTBI_3$ (black), **13** (red), **12** (blue), and **11** (green).

Because of the color change and the potential to observe changes in electronic structure, we characterized our TTF-based materials by UV-Vis-NIR spectroscopy. The solution UV-Vis-NIR spectrum of H_4TTFTB in DMF is shown in Figure 3.6a. There is a strong absorption band below 350 nm typical of TTF and phenyl rings as well as a less intense band at 450 nm corresponding to a TTF-based transition.[98] The pronounced low-energy tail of the 450 nm transition potentially corresponds to a transition from a TTF-based HOMO to a benzoate-based LUMO. In order to rationalize the position of the HOMO-LUMO gap, we can examine the HOMO and LUMO of the individual components. The HOMO of TTF has been determined to be -6.4 eV vs. vacuum.[99] Reports of the HOMO for benzoic acid have given values ranging from -9.17 to -9.70 eV vs. vacuum[100–102] and the lowest energy electronic transition has been reported to be 270 nm, or 4.6 eV.[98] The approximate energy of the benzoic acid HOMO is then between -4.6 eV and -5.1 eV, resulting in a HOMO-LUMO transition in H_4TTFTB between 1.3 eV and 1.8 eV, or 950 to 690 nm. This analysis does not take into account the fact that the electron withdrawing benzoate group will lower the TTF-based HOMO and the electron donating core will raise the benzoate-based LUMO, thus causing a blueshift in the expected absorption energy. This helps explain the striking color change during the Pd-catalyzed cross coupling reaction between TTF and ethyl 4-bromobenzoate from yellow-orange to dark burgundy.
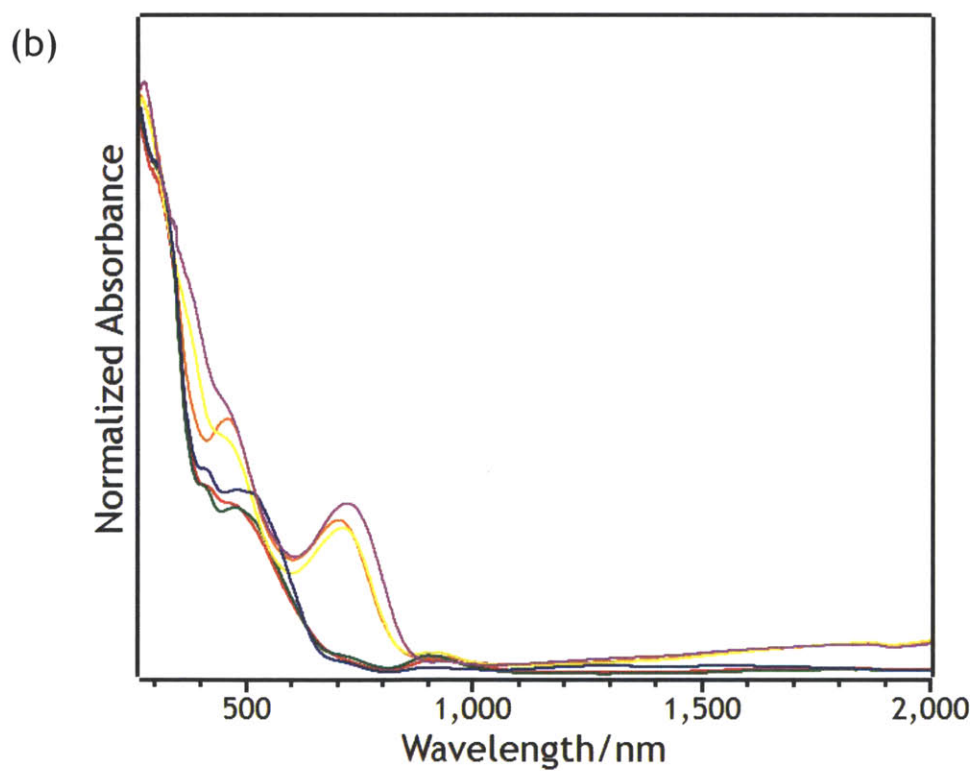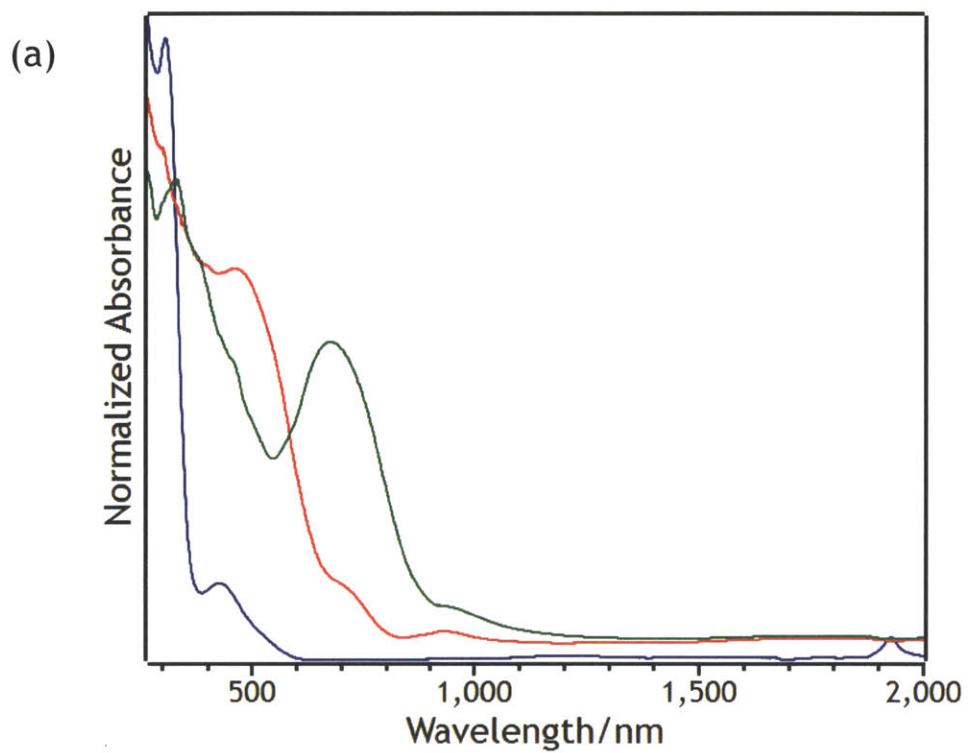
Figure 3.6 (a) Solution UV-Vis-NIR spectrum of H_4TTFTB in DMF (blue) and diffuse reflectance spectra of H_4TTFTB (red) and $H_4TTFTBI_3$ (green). (b) Diffuse reflectance spectra of **11** (red), **12** (blue), **13** (green), doped **11** (orange), doped **12** (magenta), and doped **13** (yellow).

The diffuse reflectance UV-Vis-NIR spectra of H_4TTFTB and $H_4TTFTBI_3$ are shown in Figure 3.6a. The solid and solution spectra of H_4TTFTB are very similar. The discrepancy in intensity of the peak near 450 nm could be due to the influence of solvent absorption or the freezing out of modes occurring in the solution phase when in the solid state. The shoulder near 700 nm is unique to the solid state measurement, but it is likely due to a small doped impurity since the doped sample exhibits a pronounced absorbance near 700 nm. Studies on mechanically interlocked dimers of TTF have suggested that a new peak between 600 to 900 nm likely arises from a π dimer of TTF^+.[103–107] A UV-Vis-NIR spectrum of a dilute solution of H_4TTFTB titrated with iodine does not show the appearance of this peak, which is suggestive of the assignment of this peak as arising from a dimeric species. Since H_4TTFTB is almost completely singly oxidized in this case, the lack of a charge transfer band arising from a monocationic π dimer is expected.

The corresponding diffuse reflectance UV-Vis-NIR spectra of **11**, **12**, **13**, and the doped species are shown in Figure 3.6b. The three materials have similar properties in the region recorded, so the spectra of **11** and its doped species will be discussed for the sake of brevity. The spectrum of **11** closely matches spectra of the interlocked dimers discussed above and exhibits sharp peaks due to the immobile units. Peaks at 705 nm and 451 nm correspond to a π dimer and TTF^+ transitions, respectively. The fact that the peak at 705 nm is so pronounced suggests that the sample is almost completely doped. Previous studies have shown that when the mixed-valence dimer peak is visible, the peak in the near infrared is nearly nonexistent. A slow rise in the Kubelka-Munk function beginning at approximately 1500 nm and continuing at the endpoint of collection, 2000 nm, potentially represents a broad charge transfer band. The fact that the rise exists in doped **11**, **12**, and **13** but not undoped **11**, **12**, and **13** suggests that this may be a feature of interest. Although weak, the transition at approximately 2000 nm (5000 cm^{-1}) is in a region typical of an intervalence charge transfer band in a TTF_2^+ dimer. Assuming a class II system in the Robin-Day classification system in which the coupling constant, H_{AB}, is significantly less than the reorganization energy, λ,[108] we would anticipate a peak width at room temperature of $(47.9 l^{0.5})$ cm^{-1} = 47.9 $(5000)^{0.5}$ cm^{-1} = 3400 cm^{-1}.[109] The peak is ill-defined, but a rough estimate affords a peak width of approximately 3000 cm^{-1}, which is in close agreement with the predicted value indicating that the systems under study are likely class II.

3.6 Conductivity and Charge Mobility Studies

The possibility of oxidizing **11-13** opened up the possibility of significantly increasing the conductivity with a small amount of oxidative doping. Using 100 μm diameter copper wire, we pasted on contacts approximately 1 mm apart using silver paint onto a 7 mm diameter pellet. We then performed standard four point probe conductivity measurements, taking into account the correction factor needed when the thickness of the pellet is comparable to the spacing of the probes. All samples measured exhibited conductivity values on the order of 10^{-6} S/cm, which compares unfavorably to values between 10^{-4} and 10^{-3} S/cm, corresponding to the conductivity values of previously reported conductive MOFs. However, the values are not particularly reliable since they are near the lower limit of the instrument used to conduct the measurements. Materials treated with iodine exhibited very similar conductivity values that could be due to nearly complete doping as discussed above. In these systems, the conductivity is expected to be one dimensional – only occurring through the TTF stack. When ground into a powder for a bulk

measurement, the grain boundary resistance is likely to be high as the hopping direction can change significantly upon encountering another crystallite.

The crystals of **11-13** were too small to perform single crystal measurements of conductivity, so we took a different approach to understand the inherent charge transport properties without complications arising from grain boundary resistance. Flash photolysis time resolved microwave conductivity (FP-TRMC) measurements provided us a non-contact method to make small length-scale charge mobility measurements.[110,111] With this technique, our collaborators at the University of Osaka were able to probe the conductivity of **11-13** on the length scale of several nanometers, thus avoiding problems stemming from grain boundaries and contact resistances. These measurements were carried out in ambient conditions on films comprised of **11-13** and PMMA (40/60 wt%) due to the difficulty in solution-processing **11-13**. Samples were pulsed with 355 nm light and time-of-flight transient charge carrier collection was performed to determine the photocarrier generation efficiency. The resulting data are shown in Figure 3.7, with the resulting charge mobility values and charge generation efficiencies collected in Table 3.2.

Sample	$(\Phi\Sigma\mu)_{max}/cm^2V^{-1}s^{-1}$	Φ	$\mu/cm^2V^{-1}s^{-1}$
Zn$_2$TTFTB	$3.2 \cdot 10^{-5}$	$2 \cdot 10^{-4}$	0.21
Mn$_2$TTFTB	$2.8 \cdot 10^{-5}$	$9 \cdot 10^{-4}$	$3 \cdot 10^{-2}$
Co$_2$TTFTB	$6.0 \cdot 10^{-5}$	$3 \cdot 10^{-3}$	$2 \cdot 10^{-2}$
H$_4$TTFTB	$9 \cdot 10^{-6}$	$4 \cdot 10^{-3}$	$2 \cdot 10^{-3}$
Zn$_2$TTFTBI$_x$	$1.0 \cdot 10^{-5}$	$4 \cdot 10^{-3}$	$3 \cdot 10^{-3}$
Co$_2$TTFTBI$_x$	$1.0 \cdot 10^{-5}$	$9 \cdot 10^{-3}$	$1 \cdot 10^{-3}$

Table 3.2 Conductivity, charge separation efficiency, and charge mobility values.

The most promising sample was **11**, which exhibited a charge mobility of 0.21 cm^2/Vs. Both **12** and **13** exhibit charge mobilities one order of magnitude lower than that of **11**. One potential rationalization for the drop in mobility is hole transfer from the TTF column to the metal node, since such a transfer is only possible in the case of Co^{2+} and Mn^{2+} metal centers and not Zn^{2+}. This is, however, unlikely because the redox potential of the H$_4$TTFTB$^{+/0}$ couple, albeit in DMF, is 0.73 V vs. SHE, whereas the aqueous Mn$^{3+/2+}$ and Co$^{3+/2+}$ couples are 1.51 V and 1.82 V vs. SHE, respectively. Being in an oxygen environment, we can expect that the Mn and Co centers in the MOF would exhibit similar redox potentials, but the expected redox potential of TTFTB^{4-} in the MOF is less obvious. Regardless, the potentials are significantly different and it is unlikely that TTF$^+$ can oxidize either Mn^{2+} or Co^{2+}. The reason for the difference is unclear at the present and more experiments are needed to draw definitive conclusions.
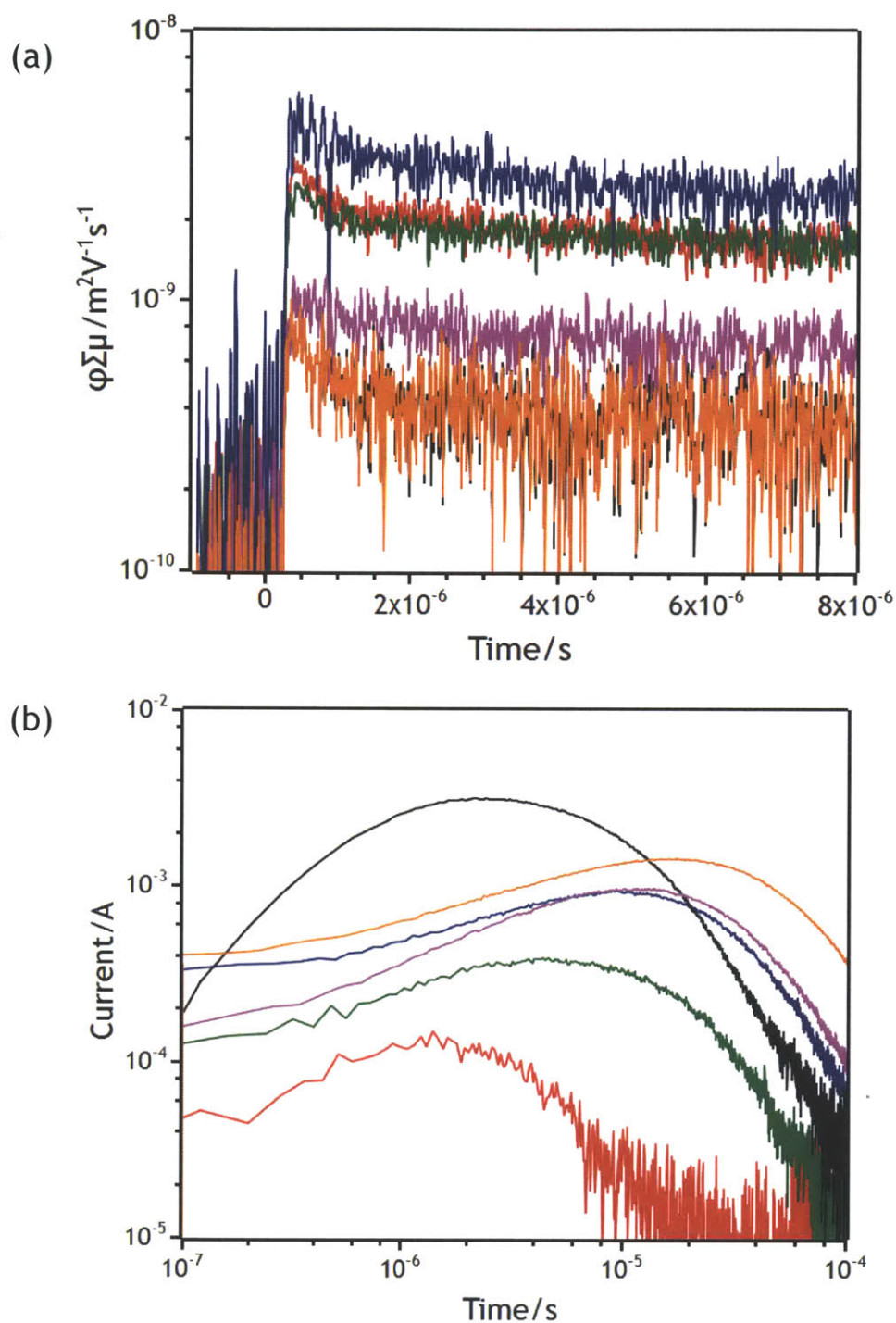
Figure 3.7 (a) Conductivity transients observed by FP-TRMC upon excitation at 355 nm with $6.5 \cdot 10^{15}$ photons cm^{-2} per pulse for H_4TTFTB (black), **11** (red), **12** (blue), **13** (green), doped **11** (orange), and doped **12** (magenta). (b) Photocurrent transients observed for 20-26 μm thick solid films of materials in PMMA matrices sandwiched between Au-semitransparent and Al electrodes. The transients were observed with a terminate resistance of 10 kΩ under an applied bias of $1.2 \text{-} 1.5 \cdot 10^4$ V/cm.

The doped materials likely exhibit poor charge mobility due to the hole transfer from iodide or triiodide to cationic TTF radicals. Since these materials are likely hole transporters, moving the hole away from the conduction pathway can result in blocking charge transport. Considering the high degree of doping in these materials, as seen by UV-Vis-NIR spectroscopy, it is likely that there are many sites from which an electron can be transferred. The free ligand likely exhibits poor ordering which results in poor charge mobility.

As a reference, commonly used thiophenes in photovoltaic applications, such as poly(3-hexylthiophene)[112] and poly(2,5-bis(3-alkylthiophen-2-yl)thieno[3,2-b]thiophenes[113] have field-effect mobilities of approximately 0.1 and 0.2-0.6 cm^2/Vs, respectively. These are bulk measurements, but it is promising that 11 has a mobility on the same order of magnitude as widely used materials. FP-TRMC measurements have also been applied to conductive covalent-organic frameworks to determine charge mobility values. These materials contain electroactive porphyrin or phthalocyanine cores stacked in a nearly eclipsed fashion to give charge mobilities between 0.1 and 8 cm^2/Vs, which are similar to the charge mobility of 11.

Application of the energy-time uncertainty principle to this system allows us to evaluate the suitability of a band model.[114,115] According to the uncertainty principle,

$$W\tau > \hbar,$$

which effectively states that a charge carrier spends less time on a site than the typical phonon timescale and thereby avoids being trapped. Here, W represents the bandwidth that is related to the overlap integral, γ, in the tight binding approach as

$$W = 4\gamma$$

and τ represents the electron-phonon scattering time that we hope to be longer than the time a carrier spends on a given site. In order to relate τ to more easily measured parameters, we can start by noting that

$$v_d = \mu E$$

where v_d is the drift velocity, μ is the electron mobility, and E is the applied field. We can relate t to measurable quantities through the effective mass of the electron, m^*. This quantity, which differs from the rest mass, allows a particle obeying quantum mechanics to be treated pseudo-classically. In order to find m^*, we can make the approximation that after every scattering event, the velocity of the electron is randomized and then proceeds to be accelerated by the field until the next event. In this case, all of the v_0 cancel with one another. We can thus describe the electron with a classical equation of motion given as

$$m^* \frac{d^2r}{dt^2} + \frac{m^*}{\tau} \frac{dr}{dt} = -eE.$$

In this equation, the scattering phenomenon is treated as a damping factor. The damping term opposes the by electric force until a point when two are equal and there is no longer acceleration. This velocity is the drift velocity of the electron and is given by

$$v_d = \frac{e\tau}{m^*} E,$$

which is in the form of the equation above, showing that

$$\mu = \frac{e\tau}{m^*}.$$

We must now address the question of the meaning of m^*. This is the mass that a particle confined in a potential appears to have if it were treated as a free particle. We can start with the group velocity of a particle, namely

$$v = \frac{d\omega}{dk} = \frac{1}{\hbar} \frac{d(\hbar\omega)}{dk} = \frac{1}{\hbar} \frac{dE}{dk}.$$

We can also note that

$$\hbar \frac{dk}{dt} = \frac{d(\hbar k)}{dt} = \frac{dp}{dt} = \frac{d(m^* v)}{dt} = m^* \frac{dv}{dt}.$$

Since we have already derived an expression for v, we can substitute it into the above equation to get

$$\hbar \frac{dk}{dt} = m^* \frac{d}{dt}\left(\frac{1}{\hbar}\frac{dE}{dk}\right)$$

$$\frac{1}{m^*}\frac{dk}{dt} = \frac{1}{\hbar^2}\frac{d^2 E}{dk^2}\frac{dk}{dt}$$

$$m^* = \hbar^2 \left(\frac{d^2 E}{dk^2}\right)^{-1}.$$

We now need to find a relationship between E and k for our system. As TTF is primarily a hole conductor, we can consider the conduction through the HOMO. By using the tight binding approximation, we can consider, to a very good approximation, a TTF core and the two adjacent TTF cores. The Bloch wave function for this system can be given by

$$\psi_k = \sum_m e^{ik \cdot T_m} c(k)|\varphi_m\rangle,$$

where T_m is a translation vector from one TTF to the next, $c(k)$ is a mixing coefficient, and $|\varphi_m\rangle$ is the HOMO of TTF unit m.

We can insert this wavefunction into the Schrödinger Equation to obtain

$$H \sum_m e^{ik \cdot T_m} c(k)|\varphi_m\rangle = E \sum_m e^{ik \cdot T_m} c(k)|\varphi_m\rangle.$$

We can then left multiply by an arbitrary state such as $\langle\varphi_0|$. This gives

$$\sum_m e^{ik \cdot T_m} c(k)\langle\varphi_0|H|\varphi_m\rangle = E \sum_m e^{ik \cdot T_m} c(k)\langle\varphi_0|\varphi_m\rangle.$$

We then make the tight binding approximation and note that the orbital overlap between adjacent HOMOs is small, thus making all $|\varphi_m\rangle$ states nearly orthogonal and leading to the approximation $\langle\varphi_n|\varphi_m\rangle = \delta_{mn}$. We can also define $E_0 = \langle\varphi_n|H|\varphi_n\rangle$ and $\gamma = -\langle\varphi_n|H|\varphi_{n\mp1}\rangle$. Substituting these terms into the above expression gives

$$e^{-ika}c(k)\langle\varphi_0|H|\varphi_{-1}\rangle + c(k)\langle\varphi_0|H|\varphi_0\rangle + e^{ika}c(k)\langle\varphi_0|H|\varphi_1\rangle = Ec(k)\langle\varphi_0|\varphi_0\rangle$$

$$E_0 - \gamma e^{ika} - \gamma e^{-ika} = E$$

$$E = E_0 - 2\gamma \cos(ka).$$

The bandwidth, W, of this band is thus given by $W = 4\gamma$. Near the $k = 0$ point where the HOMO energy is highest and thus most likely to facilitate hole conduction, we can approximate the band energy as

$$E \approx E_0 - 2\gamma\left(1 - \frac{k^2 a^2}{2}\right) = E_0 - 2\gamma + \gamma k^2 a^2.$$

We can finally take the second derivative with respect to the wave vector and substitute into the expression for effective mass to give

$$\frac{d^2 E}{dk^2} = 2\gamma a^2 = \frac{W a^2}{2}$$

$$m^* = \frac{2\hbar^2}{W a^2}.$$

We can return to the original uncertainty relation and insert the expressions for τ and m^* to give

$$\frac{W\mu m^*}{e} > \hbar$$

$$\frac{W\mu}{e}\frac{2\hbar^2}{Wa^2} > \hbar$$

$$\mu > \frac{ea^2}{2\hbar}$$

Using the separation in our system of $a = 3.8\text{Å}$, we see that the minimum charge mobility required for band theory to be applicable in M_2TTFTB is 0.8 cm^2/Vs. This is larger than the values we obtain, but not significantly so, indicating that the system can likely be described as partially delocalized. We thus arrive at similar conclusions using a molecular analysis arising from interpretations of UV-Vis-NIR spectra and supramolecular analysis. One line of reasoning to explain the localized nature of the cationic radical is the 60° rotation between TTF units that lowers orbital overlap between adjacent TTF units as seen in Figure 3.8. In order to understand the overlap more quantitatively, we extracted the coordinates of a pair of adjacent TTFTB^{4-} from the solid state structure of **11**, removed the zinc atoms, included protons on the carboxylate groups, and then calculated the zero-point energy and the corresponding Kohn-Sham orbitals. The two occupied orbitals highest in energy represent, as suspected, the "bonding" and "anti-bonding" of the two TTF units. These states are separated by approximately 0.2 eV, which is indicative of poor overlap between the TTF cores. This poor overlap helps to justify the use of the tight binding approximation above.
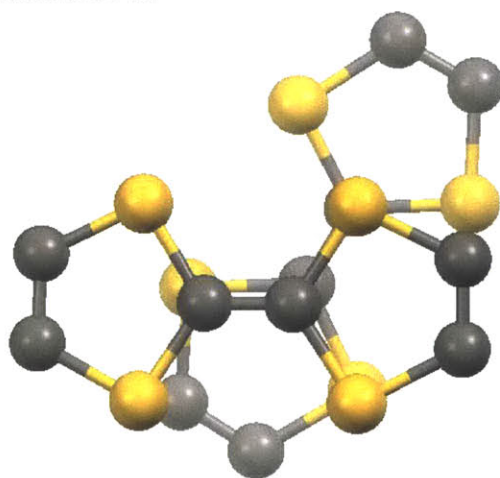
Figure 3.8 Overlap of TTF units in **11**.

3.7 Summary and Future Studies

In summary, we have prepared a novel ligand H_4TTFTB that self assembles upon mixing with zinc, cobalt, and manganese nitrate into a helical structure that was previously unknown for TTF-based materials. The TTF cores are arranged such that there is one close S⋯S contact of 3.80 Å. Both the ligand and the MOF can be oxidized in the presence of iodine, as confirmed by EPR and UV-Vis-NIR studies. Although the extent of doping was not confirmed in the case of **11-13**, comparison of the spectral data with previous studies conducted on TTF-based dimers suggests that nearly all of the TTF cores have been singly oxidized. There appears to be a weak TTF-TTF$^+$ charge transfer band whose characteristics suggest that **11-13** are class II materials. Four-point-probe measurements conducted on pressed pellets indicate low conductivity that is at

least partly due to the presence of grain boundaries between randomly oriented particles and the likely one-dimensional conductivity pathways. Flash-photolysis time-resolved microwave conductivity studies that avoid problems stemming from anisotropy and grain boundaries show that **11** possesses a charge mobility of 0.21 $cm^2/V \cdot s$, with **12** and **13** having charge mobilities approximately one order of magnitude lower. When compared with estimates derived from basic band theory, the charge mobility of **11** is nearly high enough to allow for a band model of charge transport, suggesting a partially delocalized system as suggested by the UV-Vis-NIR data.

There remain studies to be carried out on the H_4TTFTB system to more completely understand its behavior. The presented UV-Vis-NIR study is only a cursory study that presents an incomplete understanding of the peak assigned as the charge transfer band. In order to better understand this feature, the following experiments can be conducted. H_4TTFTB and $H_4TTFTBI_3$ can be ground together with a mortar and pestle in a 1:1 ratio and the solid state spectra can be observed. A charge transfer band near 2000 nm should be readily evident due to the high probability of a TTF-TTF$^+$ interaction in the relatively homogeneous mixture of the oxidized and neutral materials. Mixtures of different ratios can be prepared and studied to see if the charge transfer peak decays on either side of what should be a maximum at a 1:1 ratio. Since the molar absorptivity of the peak is important for calculating the coupling constant between TTF units, it is of interest to approximate this value. A thin film of H_4TTFTB can be spin-coated onto a substrate and its UV-Vis-NIR spectrum can be measured. After the thickness of the film has been determined, the spectrum can be converted into a plot of molar absorptivity by also noting the change in mass of the substrate. If this spectrum is similar to the DRIFTS spectrum of H_4TTFTB, the values of the Kubelka-Munk function can be approximately correlated to molar absorptivity values. Care must be taken to ensure the reproducibility of the degree of grinding and packing employed in the measurement. Measurements can also be taken of **11-13** in a similar fashion, and as long as the sample preparation is similar to that of H_4TTFTB, approximate molar absorptivities can be assigned. Rather than soaking **11-13** in I_2 solutions for upwards of one day, the soaking time can be shortened and the spectrum can be measured for each degree of doping, hoping to emulate the rise and decay of the charge transfer band. The coupling constant between TTF units can then be approximated and a more quantitative assignment of the degree of delocalization can be made.

Probing the system with temperature dependent Raman spectroscopy might also yield insight into the rate constant of electron transfer from one TTF to an adjacent oxidized TTF. The stretching frequency of the central ethylene unit is highly sensitive to the oxidation state of TTF, making it a good handle for Raman spectroscopy. The stretch can first be identified for **11-13** and their corresponding doped species. A spectrum of a partially doped sample can then be taken. Since the rate of charge transfer is likely slow, the temperature can be increased until these signals are observed to coalesce. By modeling this information, a rate constant can be obtained and correlated with the information gleaned from UV-Vis-NIR studies.

Film growth is another area that will be important to study to understand whether **11-13** are functional materials. We have made cursory attempts towards this goal using FTO and gold- and C_{60}-coated glass slides, but have been unable to obtain any uniformity in the films. These substrates were chosen since they are typical components in photovoltaic devices. The wide absorption spectrum led us to pursue application as solar cell materials. We are also currently exploring the possibility of film growth on single layer graphene substrates. As discussed earlier, uniform COF films have been grown on single layer graphene substrates, which likely stems from the interaction of the π cores of COF building blocks with the graphene substrate. Since our

system also seeks to arrange an organic π system, we anticipate that graphene will prove to be an effective substrate for film growth and subsequent device construction.

We must also understand the reason for the significant difference in charge mobility between **11**, and **12** and **13**. One hypothesis to test is that charge transfer occurs from the M^{II} center to TTF^+. In order to test this hypothesis, EPR spectroscopy can be conducted. After measuring a sample of undoped material, a small amount of I_2 can be introduced into the tube without allowing the tube to move. The intensity of the paramagnetic metal signal can be compared, since the M^{III} species in use here possess integer spins and would be silent in typical X-band measurements. In order to address the possibility of charge transfer to triiodide, the anion can be exchanged for a less redox active small anion such as chloride and the charge mobility can be measured. If the charge mobility increases, it would suggest that charge transfer to the anion plays an important role in charge transport.

In addition to the aforementioned studies on H_4TTFTB-based materials, it will also be interesting to study related materials. Although we were unsuccessful in its preparation, it is still worth pursuing the selenium analog of H_4TTFTB. Selenium has larger frontier orbitals than sulfur and, if the selenium analog self-assembles into a stacked structure, it will prove more likely to be conductive. Another possibility is to use the TTF core but append different aryl substituents to retain the ease of synthesis while introducing new functionalities. One aryl molecule of interest is 3-aza-4-bromobenzoic acid. The helical structure of **11-13** is likely caused at least in part by the unfavorable H···H interaction of the benzoate groups. The positioning of a nitrogen atom *ortho* to the TTF core reduces the driving force for the rings to offset and increases the likelihood of planarization and thus more S···S overlap.

3.8 Experimental Section

Materials. Tetraethyl tetrathiafulvalene tetrabenzoate (**Et₄TTFTB**) was prepared according to a literature procedure.[86] $Mn(NO_3)_2 \cdot xH_2O$ (99.98% metals basis, Alfa Aesar), $Co(NO_3)_2 \cdot xH_2O$ (99%, Strem Chemicals), $Zn(NO_3)_2 \cdot xH_2O$ (99%, Alfa Aesar),tetrabutylammonium hexafluorophosphate (≥99%, Fluka), Kryptofix® 222 (Cryptand 222, 4,7,13,16,21,24-Hexaoxa-1,10-diazabicyclo[8.8.8]-hexacosane, $C_{18}H_{36}N_2O_6$, 98%, Acros Organics), silver nitrate (99.9%, Strem Chemicals), ethanol (Macron Chemical), and *N,N'*-dimethylformamide (Macron Chemical) were obtained from commercial sources and used as received unless otherwise indicated. Dry, deaereated DMF was obtained by degassing DMF with a vigorous flow of argon for 30 min and then passing the solvent through two alumina columns in a Glass Contour Solvent System. Deuterochloroform and DMSO-d_6 were purchased from Cambridge Isotope Laboratories and used as received.

Instrumentation. NMR spectra were recorded on a Varian 300 Mercury NMR spectrometer and a Bruker Avance-400 NMR spectrometer. ^1H NMR data are reported as follows: chemical shift (multiplicity (br s = broad singlet, dt = doublet of triplets), integration, coupling constants, and peak assignments). ^1H and ^{13}C chemical shifts are reported in ppm from TMS with the residual solvent resonances as internal standards.

Elemental analyses were performed by Midwest Microlab.

Thermogravimetric analyses (TGA) were performed on a TA Instruments Q500 Thermogravimetric Analyzer. Samples were placed in a platinum pan and heated from room temperature to 600°C at 1°C/min under a stream of N_2.

Single crystal X-ray diffraction was performed with crystals mounted on a Kapton loop using motor oil. Low temperature (100 K) diffraction ndata (ϕ- and ω-scans) were collected on a Bruker-AXS X8 Kappa Duo diffractometer coupled to a Smart APEX II CCD detector with MoKa radiation (l = 0.71073 Å) from a $I\mu S$-micro source. Absorption and other corrections were applied using SADABS. The structure was solved by direct methods using SHELXS and refined against F^2 on all data by full-matrix least squares as implemented in SHELXL-97. All non-hydrogen atoms were refined anisotropically. Hydrogen atoms were included in the model at geometrically calculated positions using a riding model.

Powder X-ray diffraction (PXRD) patterns were recorded with a Bruker D8 Advance diffractometer equipped with a $\theta/2\theta$ Bragg-Brentano geometry and nickel-filtered Cu Ka radiation (Kα_1 = 1.5406 Å, Kα_2 = 1.5444 Å, Kα_1/Kα_2 = 0.5). The tube voltage and current were 40 kV and 40 mA, respectively. Samples for PXRD were prepared by placing a thin layer of powdered material on a zero-background crystal plate.

Gas sorption data was acquired on a Micromeritics ASAP 2020 Accelerated Surface Area and Porosimetry analyzer. Ultra-high purity grade N_2 and He were used for adsorption measurements. Prior to analysis, materials were activated by removing the solvent at 200°C for 12 hours, making sure that the degas rate never exceeded 2 mtorr/min. N_2 adsorption isotherms were measured at 77K. Ultra high purity grade (99.999% purity) N_2 and He, oil-free valves and gas regulators were used for the free space correction and measurement.

Cyclic voltammograms were obtained using a Bio-logic SP-200 potentiostat. All measurements were carried out in an Innovative Technologies glovebox under N_2 in DMF with 0.1M tetrabutylammonium hexafluorophosphate. All reported potentials are referenced to the Fc/Fc$^+$ couple. The working electrode was a glassy carbon button electrode (BASi, 0.071 cm^2) and the counter electrode was a platinum wire (Alfa Aesar). The reference electrode was prepared by transferring a solution of silver nitrate (16.9 mg, 0.100 mmol) and Cryptand 222 (Kryptofix® 222, 155 mg, 0.411 mmol) in a 0.1M solution of tetrabutylammonium hexafluorophosphate in dry, deaerated DMF to a nonaqueous reference electrode kit (BASi). The standard potential of this reference electrode was determined to be $E°_{Ag/Ag(crpytand)+}$ = -0.526 V vs. Fc/Fc$^+$, and its drift was determined to be less than 10 mV over the course of three months. Because of its prior demonstrated stability, this reference electrode was determined to be an ideal system for experiments in DMF, wherein Ag/Ag$^+$ reference electrodes are typically unstable.[116]

Conductivity measurements were performed on pellets pressed using a 7 mm diameter die (International Crystal Labs) at 2.5 Mg for three minutes using a Specac pellet press. Four copper wire (100μm diameter) leads were pasted on with silver paint (Silver Adhesive 503, 62% Weight Solids, Electron Microscopy Sciences) with a spacing of approximately 1 mm. The samples were then placed on a glass slide with copper wire (10 gauge, Arcor) leads immobilized with epoxy. Contact between the leads from the pellets and the wire on the glass slide was made with silver paint. The copper wire from the slide was interfaced with a Jandel Model RM3-AR sourcemeter to carry out the four-point probe measurement.
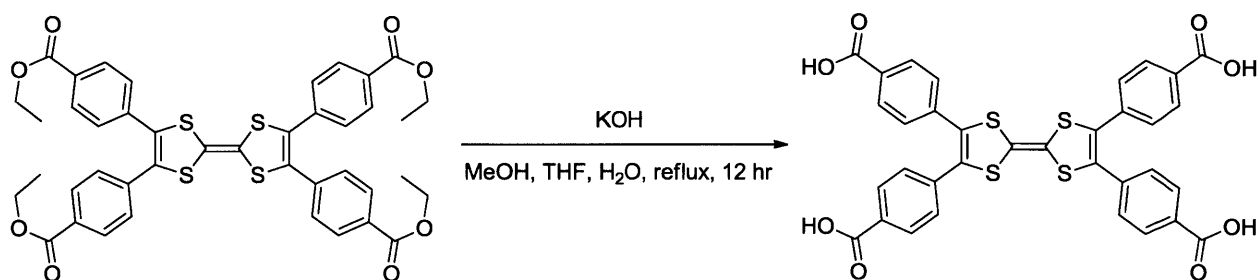
Tetrathiafulvalene tetrabenzoic acid · 1.5 MeOH (H₄TTFTB). This procedure was adapted from a literature procedure.[87] Methanol, THF, and distilled water were degassed under a vigorous flow of nitrogen for 30 minutes. A 50 mL flask was charged with Et₄TTFTB (734 mg, 0.921 mmol) and subjected to three cycles of evacuation and refilling with N_2. Degassed methanol (7 mL) and THF (7 mL) were added to generate a suspension. In a separate flask, sodium hydroxide (466 mg, 11.6 mmol) was dissolved in degassed water (5 mL). The sodium hydroxide solution was added to Et₄TTFTB under N_2 and the reaction was heated to reflux for 12 hours. The reaction was then cooled to room temperature and the volatiles were removed *in vacuo*. 1M HCl (30 mL) was added to afford a maroon precipitate, which was collected by filtration and washed with water (50 mL). The product was collected and put under high vacuum for 12 hours to afford H₄TTFTB as a maroon solid (556.5 mg, 0.813 mmol, 88%). ^{1}H NMR (DMSO-d_6): δ = 13.14 (br s, 4H, CO₂*H*), 7.87 (dt, 8H, *J* = 8.3 Hz, 1.8 Hz, C*H*CCO₂H), 7.35 (dt, 8H, *J* = 8.4 Hz, 1.8 Hz, SCCC*H*). ^{13}C NMR (DMSO-d_6): δ = 166.5, 135.5, 131.2, 129.9, 129.2, 129.1, 107.7. Anal. Calcd. for $C_{35.5}H_{26}O_{9.5}S_4$: C, 58.18; H, 3.57. Found: C, 57.99; H, 3.60.

Zn₂TTFTB(H₂O)₃(DMF)₂ (11). X-ray quality single crystals: A solution of zinc nitrate hexahydrate in 1:1 water/ethanol (66.5 mM, 0.7 mL) was added to a solution of H₄TTFTB in 3:1 DMF/ethanol (17.9 mM, 0.7 mL). The reaction was heated to 65°C for 72 hours to afford **11** as dark red needles. Anal. Calcd. for $C_{40}H_{36}N_2O_{13}S_4Zn_2$: C, 47.48; H, 3.59; N, 2.77. Found: C, 47.51; H, 3.60; N, 2.70.
Bulk synthesis: Zinc nitrate hexahydrate (319 mg, 1.07 mmol) was dissolved in 1:1 water/ethanol (32 mL). H₄TTFTB (200 mg, 0.292 mmol) was dissolved in DMF (24 mL). To this was added ethanol (8 mL). The zinc nitrate solution was slowly added to H₄TTFTB, making sure that no precipitate formed upon addition. The reaction was heated at 75°C for 72 hours to afford a precipitate. The product was collected by filtration and washed with DMF (40 mL) and ethanol (40 mL) to afford **11** as a dark maroon powder (221 mg, 0.218 mmol, 75%). PXRD of the bulk material indicated phase purity. The powder was evacuated at 200°C for 12 hours at 4 mtorr. Anal. Calcd. for $C_{34}H_{16}O_8S_4Zn_2$: C, 50.32; H, 1.99. Found: C, 49.80; H, 1.64.

Mn₂TTFTB(DMF)₀.₇(H₂O)₃.₇₅ (12). Manganese nitrate hydrate (268 mg, 1.07 mmol) was dissolved in 1:1 water/ethanol (32 mL). H₄TTFTB (200 mg, 0.293 mmol) was dissolved in DMF (24 mL). To this was added ethanol (8 mL). The manganese nitrate solution was slowly added to H₄TTFTB, making sure that no precipitate formed upon addition. The reaction was heated at 75°C for 72 hours to afford a precipitate. The product was collected by filtration and washed with DMF (40 mL) and ethanol (40 mL) to afford dark maroon single crystals of Mn₂TTFTB(DMF)₀.₇(H₂O)₃.₇₅. Anal. Calcd. for $C_{36.1}H_{28.4}O_{12.5}N_{0.7}S_4Mn_2$: C, 47.68; H, 3.15; N, 1.08. Found: C, 47.55; H, PXRD of the material revealed phase purity. The crystals were evacuated at 200°C for 12 hours at 4 mtorr to yield the evacuated crystals (205 mg, 0.259 mmol, 88%). Anal. Calcd. for $C_{34}H_{16}O_8S_4Mn_2$: C, 51.65; H, 2.04. Found: C, 51.36; H, 2.37.

Co$_2$TTFTB(DMF)$_{1.75}$(H$_2$O)$_4$ (13). Cobalt nitrate hexahydrate (311 mg, 1.07 mmol) was dissolved in 1:1 water/ethanol (32 mL). H$_4$TTFTB (201 mg, 0.293 mmol) was dissolved in DMF (24 mL). To this was added ethanol (8 mL). The cobalt nitrate solution was slowly added to H$_4$TTFTB, making sure that no precipitate formed upon addition. The reaction was heated at 75°C for 72 hours to afford a precipitate. The product was collected by filtration and washed with DMF (40 mL) and ethanol (40 mL) to afford dark maroon single crystals of Co$_2$TTFTB(DMF)$_{1.75}$(H$_2$O)$_4$. Anal. Calcd. for C$_{39.25}$H$_{36.25}$N$_{1.75}$O$_{13.75}$S$_4$Co$_2$: C, 47.21; H, 3.66; N, 2.45. Found: C, 47.16; H, 3.60; N, 2.35. PXRD of the material revealed phase purity. The crystals were evacuated at 200°C for 12 hours at 4 mtorr to yield the evacuated crystals. However, the elemental analysis did not pass.
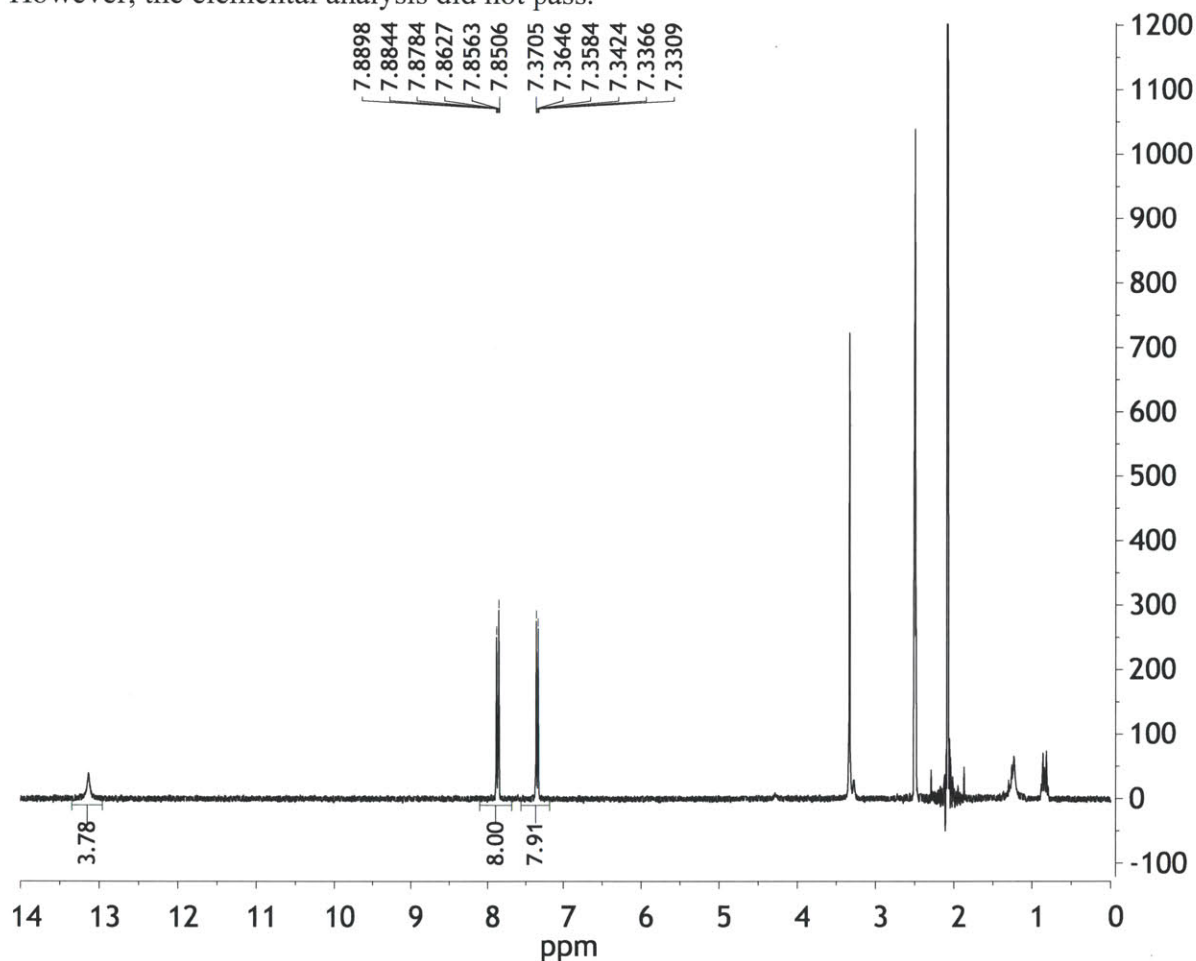
Figure 3.9 ^{1}H NMR spectrum of H$_4$TTFTB
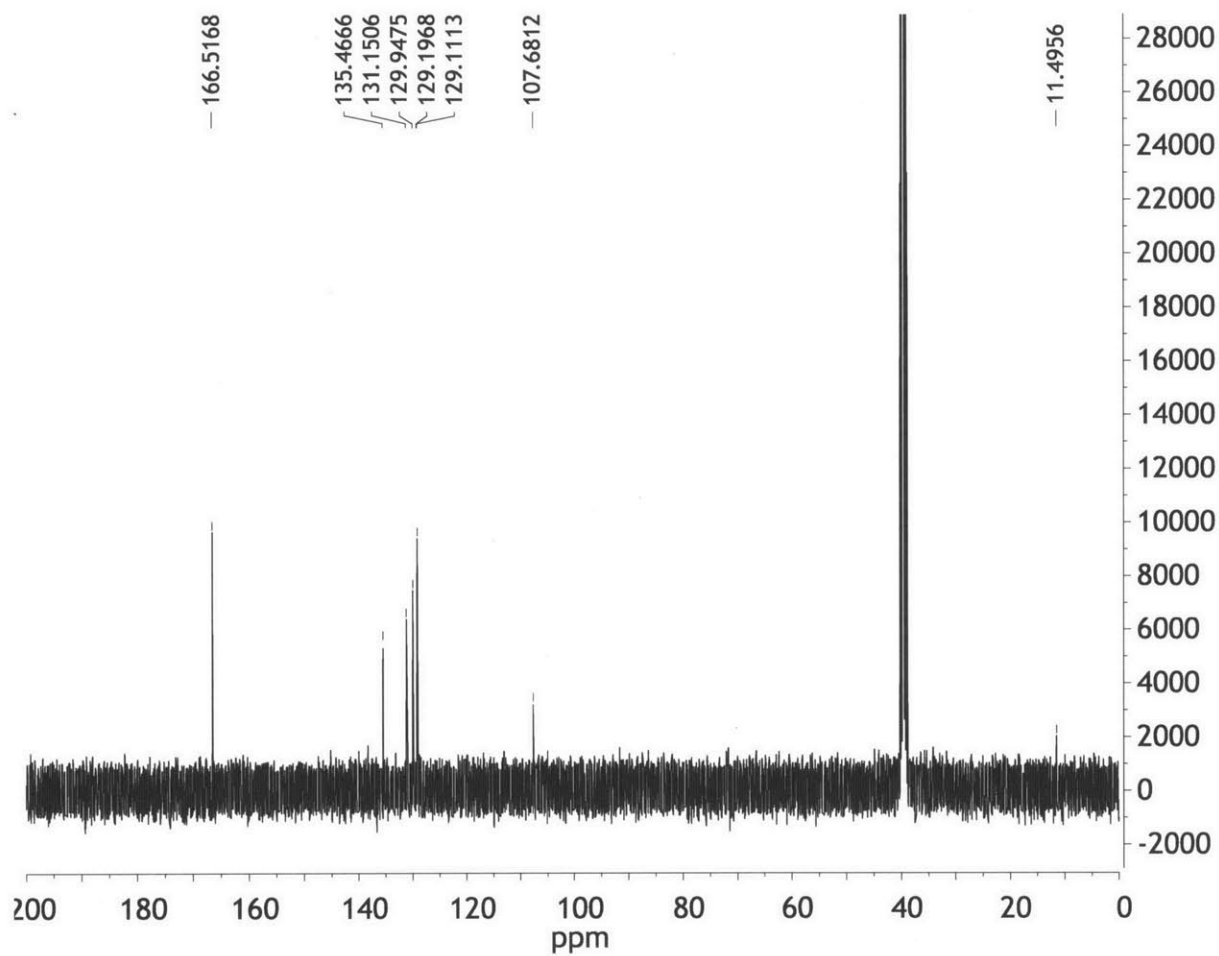
Figure 3.10 ^{13}C NMR spectrum of H$_4$TTFTB

Peak labels (left to right): 166.5168, 135.4666, 131.1506, 129.9475, 129.1968, 129.1113, 107.6812, 11.4956

Table 3.3 Crystal data and structure refinement parameters for ZnTTFTB (**11**).

empirical formula	$C_{41.59}H_{38.99}N_{1.90}O_{12.85}S_4Zn_2$
formula weight	1029.96
Temperature/K	100(2)
λ/Å	0.71073
crystal dimensions/mm^3	0.20 x 0.05 x 0.05
crystal system	Hexagonal
space group	$P6_5$
a/Å	19.293(3)
b/Å	19.293(3)
c/Å	20.838(3)
α/°	90
β/°	90
γ/°	120
V/Å^3	6717.4(17)
Z	6
ρ calcd/mg·m^{-3}	1.528
μ/mm^{-1}	1.322
F(000)	3172
θ range collected	2.33 to 24.34°
limiting indices	$-22 \leq h \leq 22$
	$-22 \leq k \leq 22$
	$-24 \leq l \leq 24$
Completeness to θ	99.8%
Reflections collected/unique	105711/7532
min and max transmission	0.9368 and 0.7779
data/restraints/parameters	7352/5/574
R(int)	0.0665
goodness-of-fit on F^2	1.061
Final R indices [I>2σ(I)]	$R_1 = 0.0216$
	$wR_2 = 0.0498$
R indices (all data)	$R_1 = 0.0227$
	$wR_2 = 0.0503$
largest diff. peak and hole	0.430 and -0.193 e$^-$/Å^3

Table 3.4 Crystal data and structure refinement parameters for CoTTFTB (**12**).

empirical formula	$C_{41.58}H_{20}N_{1.82}O_{12.88}S_4Co_2$
formula weight	997.24
Temperature/K	100(2)
$\lambda/\text{Å}$	0.71073
crystal dimensions/mm^3	0.40 x 0.15 x 0.10
crystal system	Hexagonal
space group	$P6_1$
a/Å	19.3867(7)
b/Å	19.3867(7)
c/Å	20.8268(15)
$\alpha/°$	90
$\beta/°$	90
$\gamma/°$	120
V/Å^3	6778.9(6)
Z	6
ρ calcd/mg·m^{-3}	1.466
μ/mm^{-1}	0.982
F(000)	3020
θ range collected	2.30 to 26.89°
limiting indices	$-24 \leq h \leq 24$
	$-24 \leq k \leq 24$
	$-26 \leq l \leq 26$
Completeness to θ	100%
Reflections collected/unique	130979/9985
min and max transmission	0.6948 and 0.9082
data/restraints/parameters	9985/103/582
R(int)	0.0807
goodness-of-fit on F^2	1.059
Final R indices [I>2σ(l)]	$R_1 = 0.0374$
	$wR_2 = 0.0944$
R indices (all data)	$R_1 = 0.0416$
	$wR_2 = 0.0974$
largest diff. peak and hole	0.564 and -0.586 e$^-$/Å^3

Table 3.5 Crystal data and structure refinement parameters for MnTTFTB (**13**).

empirical formula	$C_{40.94}H_{37.30}Mn_2N_{1.76}O_{12.59}S_4$
formula weight	993.54
Temperature/K	100(2)
$\lambda/\text{Å}$	0.71073
crystal dimensions/mm^3	0.20 x 0.05 x 0.03
crystal system	Hexagonal
space group	$P6_5$
a/Å	19.4690(7)
b/Å	19.4690(7)
c/Å	20.6804(8)
$\alpha/^\circ$	90
$\beta/^\circ$	90
$\gamma/^\circ$	120
V/Å^3	6788.5(4)
Z	6
ρ calcd/mg·m^{-3}	1.458
μ/mm^{-1}	0.805
F(000)	3060
θ range collected	2.61 to 30.37°
limiting indices	$-27 \leq h \leq 27$
	$-22 \leq k \leq 24$
	$-29 \leq l \leq 29$
Completeness to θ	100%
Reflections collected/unique	231237/13845
min and max transmission	0.8556 and 0.9763
data/restraints/parameters	13845/5/589
R(int)	0.0672
goodness-of-fit on F^2	1.029
Final R indices [I>2σ(l)]	$R_1 = 0.0345$
	$wR_2 = 0.0893$
R indices (all data)	$R_1 = 0.0414$
	$wR_2 = 0.0938$
largest diff. peak and hole	0.948 and -0.430 e$^-$/Å^3

Appendix A: Using MATLAB as a Tool for Structure Determination

Materials can undergo a wide variety of structural distortions in response to different stimuli. These distortions can diminish crystallinity in the material, meaning that single crystal X-ray diffraction is no longer viable, rendering powder X-ray diffraction as a primary means of structural determination. There are a number of methods to determine a structure solution given an input hat is very close to the true structure, but obtaining the initial structure is often difficult.

We previously determined the structure of a layered material, $Zn_2(TCPE)(DMF)_x$ (TCPE = tetraphenylethylene tetracarboxylate), by single crystal X-ray diffraction.[117] Upon removal of *N,N*-diethylformamide molecules present during synthesis, the crystals were no longer suitable for structure determination by single crystal X-ray diffraction and gave a powder diffraction pattern distinct from the starting material. Widely used software such as FOX did not provide adequate structure solutions.[118] FOX takes as its input a chemical fragment and reorients and distorts it to obtain a structure solution for a given powder diffraction pattern. No input we tried resulted in a chemically sensible solution, as the layer distorted badly or the TPE carboxylate dissociated from the zinc node, to name a few problems. We surmised that the change in diffraction pattern resulted from a shifting of layers with respect to each other. In order to find an approximate structure solution, we needed software that could maintain the rigidity of individual layers while varying the translation between sheets. As a result, we wrote a MATLAB script utilizing a macro known as "Functional Slider" to manually determine an approximate structure solution.

The script takes as its input a unit cell in which one layer of the material is situated in the *ab* plane with the stacking of layers occurring parallel to the *c* axis. There are three input parameters describing the displacement of one layer relative to the other – shift along *a* (Δx), shift along *b* (Δy), and interlayer spacing (q) – that are mapped onto slider bars. After generating the resulting structure, the script outputs a plot containing both the experimental and calculated patterns that is updated as the slider bars are shifted as well as a dummy .RES file that can be used to view the calculated structure.

We chose to model the shifting of layers with respect to one another as an ABAB type structure. We can operate on an input file containing one layer with unit cell parameters *a*, *b*, and *c*. The first step involves scaling the fractional coordinates along the *c* axis to give

$$z' = \frac{c}{2q} z$$

to allow for the introduction of the second layer by pushing the first layer downward in the unit cell. We also introduce the new value for the *c* parameter *c'* given by

$$c' = 2q$$

The second layer has coordinates given by

$$(x', y', z'') = (x + \Delta x, y + \Delta y, z' + 0.5)$$

Because our script is so easily modified, we also looked to model other structural distortions while trying to model the layered structures. Another distortion that is somewhat common in MOFs is known as breathing, in which a pore shaped approximately like a rhombohedral prism can dilate and contract in the presence of different stimuli. The vertices of these rhombus-shaped pores are infinite chains of metal ions and the sides of the rhombus are constructed by organic linkers. As seen in Figure A.1, we would like to manipulate the angle θ by moving a slider and compare calculated and experimental powder patterns. In this script, we note that the length, $L/2$, between metal chains and the angle θ uniquely define the axes *a* and *b*

while leaving c unchanged. The distance L can be determined using the original a and b by noting that

$$L = \sqrt{a^2 + b^2}$$
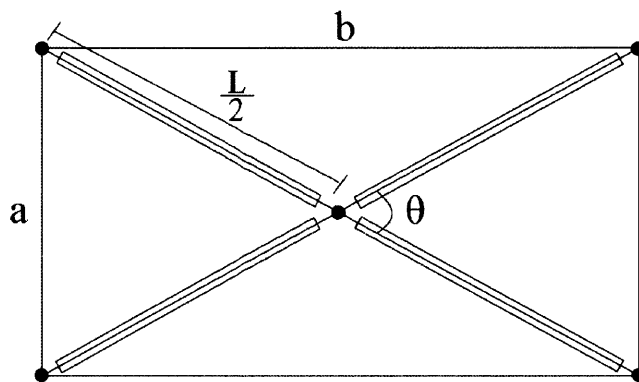
Figure A.1 Schematic drawing of a breathing MOF.

Now, specifying an angle θ, we see that we can determine new values of a and b, denoted a' and b' as follows

$$a' = L \sin\frac{\theta}{2}$$
$$b' = L \cos\frac{\theta}{2}$$

With all the alterations complete, the powder X-ray pattern can be calculated.

We begin by calculating the scattering factor

$$sf = \sum_{n=1}^{4} a_n \exp\left(-\frac{b_n}{\lambda^2}\sin\frac{2\theta}{2}\right) + c$$

where the a_n, b_n, and c values are given in crystallographic tables and are different for each atom.[119] The angle 2θ is the angle of the reflection. In order to determine 2θ, we can first find the volume of the unit cell given by

$$V = abc\sqrt{1 - \cos^2\alpha - \cos^2\beta - \cos^2\gamma + 2\cos\alpha\cos\beta\cos\gamma}$$

The spacing between planes, d_{hkl} is then given by

$$\frac{1}{d_{hkl}{}^2} = \frac{1}{V^2}(h^2 b^2 c^2 \sin^2\alpha + k^2 a^2 c^2 \sin^2\beta$$
$$+ l^2 a^2 b^2 \sin^2\gamma + 2hkabc^2(\cos\alpha\cos\beta - \cos\gamma)$$
$$+ 2kla^2 bc(\cos\beta\cos\gamma - \cos\alpha) + 2hlab^2 c(\cos\alpha\cos\gamma - \cos\beta))$$

from which we can determine the angle 2θ to be

$$2\theta = 2\sin^{-1}\left(\frac{\lambda}{2d_{hkl}}\right)$$

Each atom's subsequent contribution to the overall structure factor, S

$$S_{hkl} = sf \cdot e^{-B_{iso}\sin(2\theta/2)/\lambda^2} e^{2\pi i(hx+ky+lz)} \cdot \text{occupancy}$$

where B_{iso} is the isotropic Debye-Waller factor. This can be disregarded with minimal effect on the calculated powder pattern. The individual contributions to the overall structure factor can then be summed and multiplied by its complex conjugate to obtain $F_{hkl}{}^2$.

In the case of preferential orientation along a vector h_{pref}, k_{pref}, l_{pref} for a degree of preferential orientation $p \geq 0$, one model of preferential orientation modeling used here suggests that the squared structure factor can be modified as

$$F_{hkl}^{2\prime} = F_{hkl}^2 \exp(p \cos 2\phi)$$

for an angle ϕ between the preferred direction and h, k, l given by

$$\phi = \cos^{-1}\left(\frac{h h_{\text{pref}} + k k_{\text{pref}} + l l_{\text{pref}}}{\sqrt{h^2 + k^2 + l^2}\sqrt{h_{\text{pref}}^2 + k_{\text{pref}}^2 + l_{\text{pref}}^2}} \right)$$

The intensity, I, of each reflection is proportional to the combined structure factor F_{hkl}^2.

Once the structure factors have been determined, the calculated profile can be determined using a pseudo-Voigt fit. This fit consists of a linear combination of a Lorenzian and Gaussian fits. A parameter, η, describes the proportion of the profile described by a Lorenzian. The overall profile, $f(2\theta)$, is then

$$f(2\theta) = \eta L + (1 - \eta)G$$

where

$$L(2\theta) = \frac{F_{hkl}^2}{(2\theta - 2\theta_0)^2 + (0.5\gamma)^2}$$

and

$$G(2\theta) = F_{hkl}^2 \exp\left(\frac{-(2\theta - 2\theta_0)^2}{\frac{\gamma^2}{4\ln(2)}} \right)$$

with γ representing the full width at half maximum. The last step is to introduce the Lorentz-Polarization factor, which is the product of two terms, the Lorentz factor and the polarization factor. The Lorentz factor arises from three different phenomena: a) the arms of the diffractometer move at a constant angular velocity, but the time afforded to each reflection plane is not constant; b) diffraction for a crystal can occur for angles slightly deviating from Bragg's law; c) the difference in the amount of crystals oriented in such a way that they satisfy Bragg's law. This term, L, can be shown to be

$$L = \frac{1}{4 \sin^2 \theta \cos \theta}$$

The next factor, the polarization factor, arises from the unpolarized nature of the incident X-rays and the fact that the electron off of which the X-ray is scattering emits radiation parallel to the direction of incidence. This factor can be shown to be

$$P = \frac{1 + \cos^2 2\theta}{2}$$

Thus, the product of these two factors, LP, alters the intensity of the observed radiation such that the intensity after accounting for these effects, I', is given by

$$I' = I \frac{1 + \cos^2 2\theta}{8\sin^2 \theta \cos \theta}$$

Using the layer translation script, we were unable to fit the experimental pattern of $Zn_2(TCPE)$ to a simple translation of the layers as seen in Figure A.2. The two lowest angle peaks corresponding to the (010) and (200) reflections were present at different angles than their counterparts in the experimental pattern. This shows that the a and b unit cell parameters are incorrect in the current model. Since the calculated (010) and (200) peaks occur at angles lower

64

than those in the experimental pattern, it is clear that both the *a* and *b* values are smaller than those suggested by the initial model. Breathing is not an appropriate description of this structural change since it necessitates the increase of either *a* or *b* at the expense of the other. In order to accommodate this distortion, we simply altered *a* and *b* with slider bars and examined the resulting structure to see if the bond lengths remained sensible. We found that our new parameters were *a* = 21.79 Å, *b* = 12.65 Å, and *c* = 8.6 Å. Many of the C-C bonds are shorter than expected (e.g. 1.34 Å in the structure determined by single crystal X-ray diffraction vs. 1.30 Å as determined by this script). This suggests that the change in Zn-O bond angles and distances is likely the significant contributor to structural distortion because coordinative linkages are more pliable than C-C bonds. As a result, we do not anticipate that our script will be able to perfectly match the intensities observed in the experimental powder pattern since our carbon atom positions likely slightly differ from the true positions. We noted that a significant portion of the diffraction intensity would arise from the zinc centers, suggesting that matching the peak intensities of the first few peaks can still give us valuable structural insights.
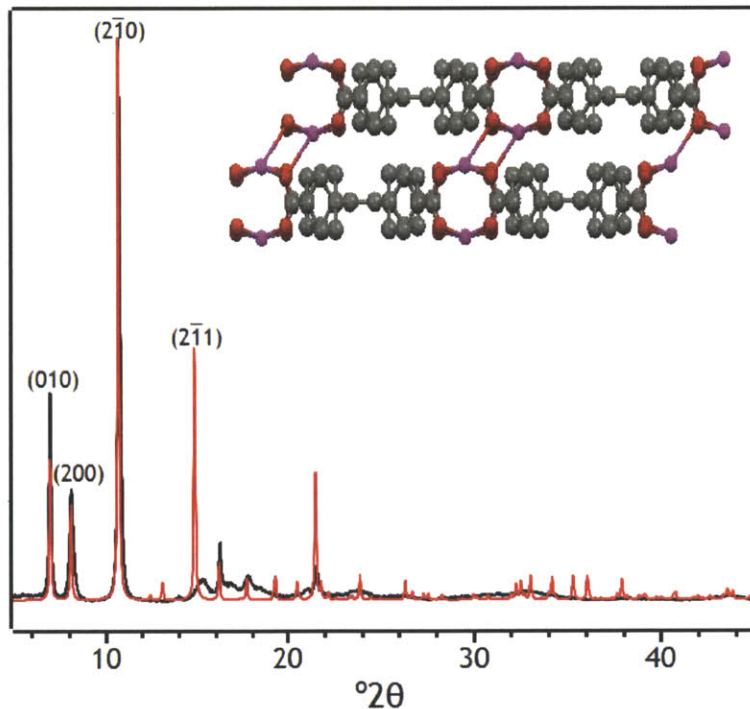
Figure A.2 Calculated (red) and experimental (black) powder diffraction patterns for desolvated Zn$_2$(TPE-tetracarboxylate) with *a* = 21.79 Å, *b* = 12.65 Å, *c* = 8.6 Å, translation along *a* of 0.13, and translation along *b* of 0.17.

In the calculated pattern, the intensities of the (010) and (200) peaks are nearly identical without any shifting, but the experimental data suggests a clear difference in their intensities. Shifting the layers with respect to each other resulted in significant changes in the relative intensities of the two peaks. We translated adjacent layers by 0.13 along *a* and 0.17 along *b* to achieve a structure whose powder diffraction pattern proved a relatively close match to the observed powder diffraction pattern. The resulting structure indicated close contacts between the carboxylate oxygen atom of one layer and the zinc center of another layer.

The peak at $2\theta \approx 15°$, corresponding to the ($2\bar{1}1$) reflection in this model, is much broader than the other peaks at low angle in the experimental pattern. It is the first non-negligible intensity peak with $k \neq 0$ and is thus the first peak that could be affected by ill-defined spacing between layers. We anticipate that the a and b axes are defined by a fairly rigid 2D net, but our model suggests that the layers are only held together along the c axis by weak Zn-O interactions. It is understandable that the predicted peak intensity deviates from the experimental peak intensity since the model does not account for ill-defined lattice spacing.

A structure we decided to examine with the breathing module of our script was that of copper(II) benzene-1,4-bis(tetrazolate), Cu(bdt). This species was reported to exhibit a significant change in the powder diffraction pattern upon removal of solvent. Similar work was subsequently reported with derivatives of bdt and exposure of the methyl derivative to different solvent conditions resulted in structures with significant changes in the powder diffraction patterns.[120] The authors surmised, based on work with the triazolate derivative, that the structure was undergoing breathing behavior that modulated the size of the rhomboid-shaped pores.[121] We found that breathing was an appropriate description of the processes occurring, as seen in Figure A.3. We note a change in angle of approximately 30° between DMF-solvated and MeOH-slvated structures. While the actual structure likely involves the flexing of the ligand as in the case of the triazolate, this approximation gives a fairly accurate assessment of the nature of the distortions.

The modular nature of this script allows it to be modified to model distortions not considered here. We anticipate that this script will be valuable to a variety of research groups studying 2D materials. One class of materials, namely covalent organic frameworks (COFs), is comprised of 2D sheets of covalently bound aromatic systems held together in the third dimension by van der Waals interactions. COFs tend to be poorly crystalline, thus making structure determination difficult. Modeling these structures typically necessitates a refinement based on a Le Bail routine[122] of the few peaks available to obtain suitable unit cell parameters.[7,16] Since results from this refinement only give approximate parameters, this script could be used to provide an approximate structure solution.

In summary, we have prepared a MATLAB script capable of providing approximate structure solutions for materials undergoing distortions such as sliding of planes relative to one another and distortion of cylindrical pores. The code was designed to be modular and thus accommodate unforeseen modifications by users. We hope that this will probe to be a valuable tool for those studying structural distortions in polycrystalline materials.
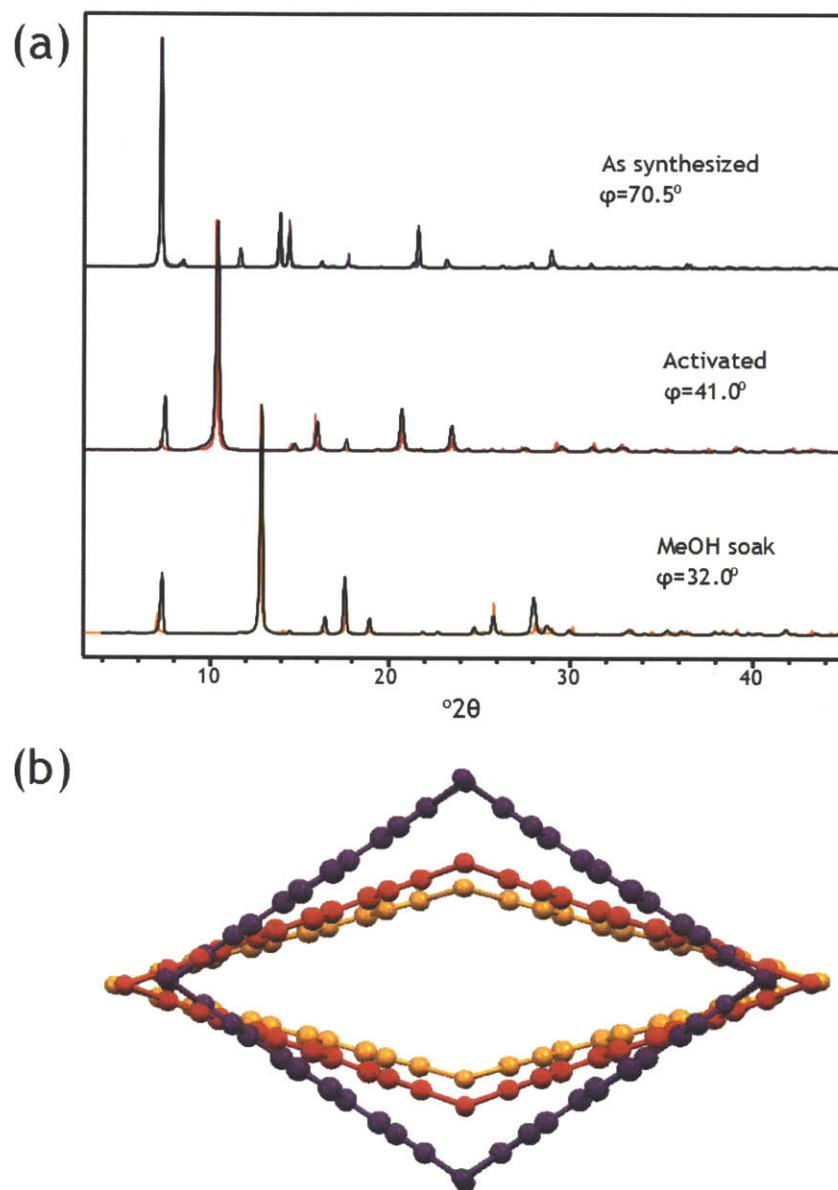
Figure A.3 (a) Experimental patterns (black) and fitted patterns for the as synthesized (purple), activated (red), and MeOH soaked (orange) structures. (b) Corresponding pore sizes color-coded to match the fitted patterns.

Appendix B: Tutorial for using `breathing.m` and `layer_pxrd.m`

This is a function implemented in MATLAB that can be used in conjunction with `funcslider.m` (available free for charge at http://www.mathworks.com/matlabcentral/fileexchange/28076-function-parameter-slider/content/funcslider.m) to dynamically model breathing behavior in MOFs. As its input, it takes the angle θ made between ligands connected by a metallic vertex. The output is a plot containing both the experimental and calculated powder patterns as well as a dummy .RES file if desired. As presently constructed the user can move a slidebar to vary the angle θ and view the calculated pattern versus the experimental pattern in real time. A variety of other parameters can be varied in this manner as well.

The function `layer_pxrd.m` operates very similarly to `breathing.m`. The only difference is that there are three variable specified at the present, namely *q1*, *q2*, and *q3*, which represent the translation along the *a* axis, translation along *b*, and interlayer spacing. The following is specific to `breathing.m`, but the same information can be used for `layer_pxrd.m`.

In order to use the script, place the files `breathing.m`, `resgenerator_1.m`, `funcslider.m`, and `scattering_factor_parameters.m` into the working directory in MATLAB. Edit the file to reflect the desired files and parameters needed for the simulation. The parameters that should be edited are indicated in the box.

```matlab
1   function atom_type=breathing(theta)
2   %%%%%breathing(theta) takes as an input the angle theta made between two
3   %%%%%ligands meeting at the metal node. Also required are the name of the
4   %%%%%coordinates file, text file of the powder diffraction pattern, desired
5   %%%%%name of the output dummy.RES file, and unit cell parameters. Other
6   %%%%%parameters that can be altered are the full-width of half maximum,
7   %%%%%wavelength of the x-ray source, isotropic debye-waller parameter,
8   %%%%%degree to which the calculated peak profile is Gaussian or Lorenzian,
9   %%%%%maximum h,k,l values, and direction and degree of preferential
10  %%%%%orientation. Any of the numerical quantities can be varied with
11  %%%%%sliders by making them inputs.
12
13
14      %%%%%%%%Parameters for the user to change
15
16      %Specify the file that will supply atom types, x, y, z, and occupancy. This
17      %file should have the format: atom_type x y z occupancy. There should be no
18      %extraneous lines/text. This does not distinguish between tabs and spaces.
19 -    coordinates='CuBDT_coordinates.txt';
20      %Specify the file that will supply the experimental powder pattern. The
21      %file should contain two columns - one with the two theta values and the
22      %other with the intensities, in that order.
23 -    experimental_pattern='CuBDT_MeOH_pxrd.txt';
24      %%%%Specify the filename of the output dummy .RES file
25 -    resfilename='CuBDT_MeOH_simulated.res';
26      %%%%Specify the full width at half maximum
27 -    fwhm=0.1;
28      %Wavelength of the x-ray source in angstroms
29 -    lambda=1.54056;
30      %isotropic debye-waller parameter - usually between 3.5 and 6.5 square
31      %angstroms
32 -    Biso=0;
33      %%%Enter the unit cell parameters here
34 -    a=13.5747;
35 -    b=22.249;
36 -    c=7.0528;
37 -    alpha=90;
38 -    beta=90;
39 -    gamma=90;
40      %%%%End of unit cell input
41      %Enter % of calculated pattern you would like to have described by a
42      %lorentzian function vs. a gaussian function
43 -    eta=0.5;
44      %%%%%%Enter the maximum h, k, and l values you would like to calculate. The
45      %%%%%%calculated peaks will be for -hmax <= h <= hmax; -kmax<= k <= kmax;
46      %%%%%%-lmax <= l <= lmax
47 -    hmax=3;
48 -    kmax=3;|
49 -    lmax=3;
50      %%%Enter the degree (number greater than or equal to 0) and direction of
51      %preferential orientation
52 -    pref=0;
53 -    preferred_h=0;
54 -    preferred_k=1;
55 -    preferred_l=0;
56      %%%%No more parameters for the user to change
```

Figure B.1 Area for the user to edit in `breathing.m`

All texted preceded by the percent sign (%) are comments and not read by MATLAB when executing the script. All comments refer to commands immediately below the comment.

In line 19, the user should replace 'CuBDT_coordinates.txt' with the name of the file containing the following information:

Atom type   x   y   z   occupancy

A sample input file is shown below. The new file name should be surrounded by single quotation marks as indicated in the sample shown in line 19.

```
Cu1 0.5 0.5 0.5 0.25
O1   0.6226  0.5 0.25      0.25
N1   0.56569 0.43663 0.6562  1
N2   0.6129  0.38905 0.5929  1
C1   0.6417  0.3609  0.75     0.5
C2   0.698   0.3046  0.75     0.5
C3   0.725   0.277   0.5818   1
H3   0.7092  0.2952  0.467    1
```

Figure B.2 Sample input file

This file can easily be generated from a .RES file by removing the header, deleting the second column in the atom list, and deleting the last column in the atom list.

The next input is on line 23, the experimental powder x-ray pattern file. This should contain two columns – the 2θ values and the intensities.

The next input, on line 25, is the desired filename for the output dummy .RES file used to visualize the calculated structure.

The rest of the inputs are parameters for the simulation. The first parameter to input, fwhm, is the full width at half maximum in units of $°2\theta$. The second is the wavelength of the x-rays used. The current value is that of Cu Kα radiation. The next parameter is Biso, the Debye-Waller factor, is set to 0 by default. The value is usually very small for molecular systems and still fairly small for other condensed phases. The value is unlikely to make a significant impact on the calculated pattern. This value serves to attenuate the structure factor at high angles with an exponential envelope.

The next set of inputs is the unit cell parameters of the original structure described by the coordinates file.

Since the calculated powder pattern is a pseudo-Voigt profile, it comprises a linear combination of a Gaussian and Lorenzian fit. The parameter eta corresponds to the proportion of the profile will be described by the Lorenzian profile.

The next three parameters are the maximum *h*, *k*, and *l* values for which peak positions and intensities will be calculated.

The last parameters to input are those to correct for preferential orientation. The first parameter, pref, represents the degree to which the sample is preferentially oriented. This should be a

number greater than or equal to 0, where 0 represents no preferential orientation. The next three parameters are the direction of preferential orientation.

Once all the parameters have been set as desired, one can proceed to run the script in MATLAB. In the command window, the program will run with sliders upon typing `funcslider(@breathing)`
and pressing enter. This will bring up a window shown below depicting the experimental powder pattern in blue. An error will be displayed in the command window. This is because the default angle is 0, thus making one of the unit cell parameters 0.
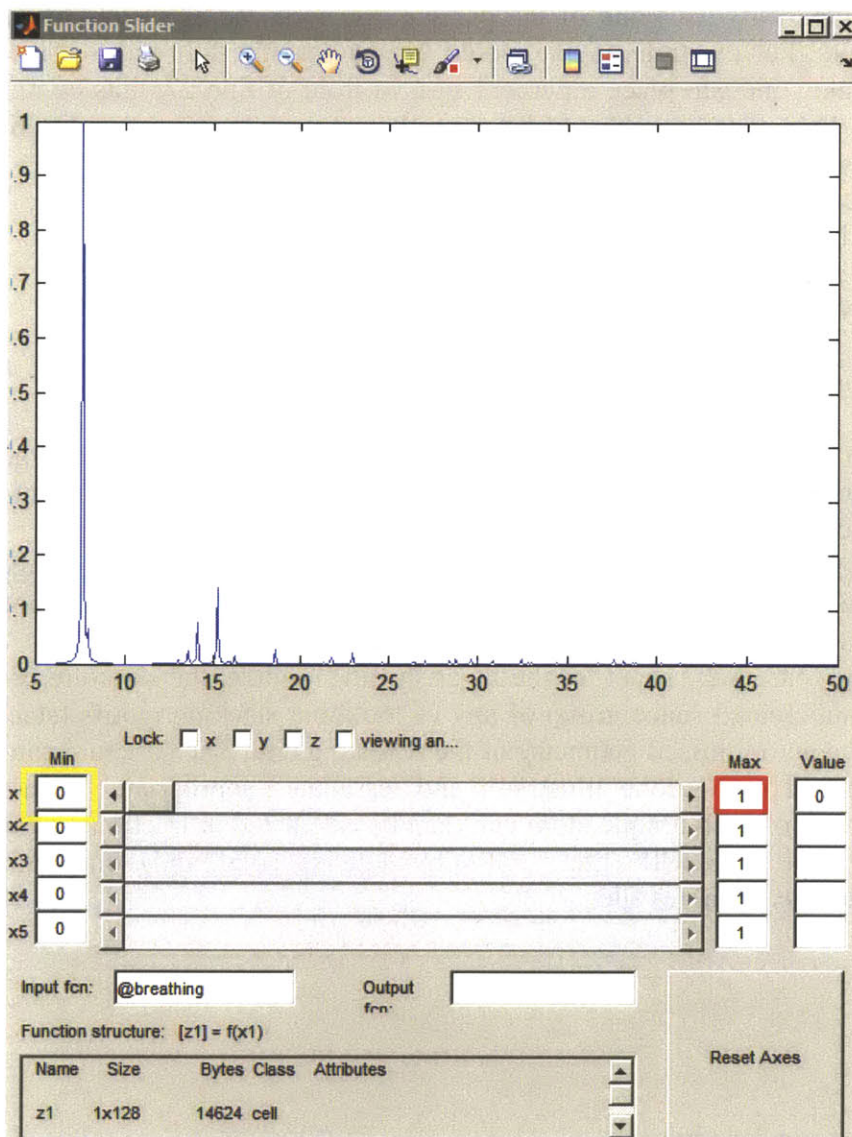
Figure B.3 Functional slider interface

The first step is to increase the maximum value to 90, which corresponds to a ligand-metal-ligand angle of 90°. To do this, click inside the textbox indicated in red and type 90 followed by either tab or enter. The slider boxed in yellow can now be moved to the desired angle. The calculated powder pattern will appear in red. During this time, a dummy .RES file will be created

every time the calculated pattern changes. If there is a considerable lag between movement of the slider and an update of the calculated pattern, the last line of `breathing.m` can be commented out by placing a percent sign in front of the text. The coding of the .RES file generator is inefficient and can significantly slow down the problem. If this is the case, after obtaining a satisfactory angle, the applet window can be closed. The last line of `breathing.m` can be uncommented and the user can type `breathing(angle)`, where `angle` is the desired value of the angle, in the command window and then press enter to generate the .RES file.

As can be seen in the functional slider applet, the script `funcslider.m` has the ability to accommodate 5 parameters that can be varied using the slider bars. Although the program as currently constructed only uses one of the parameters, it can be easily modified to vary other relevant parameters. For example, if one would like to vary the full width at half maximum of the calculated peaks, one can place a percent sign in front of line 27, thus commenting out the contents of that line. The variable `fwhm` can then be made an argument of the function 'breathing' by altering the first line to read as follows:
`function atom_type=breathing(theta, fwhm)`
The second slide bar will now become active.

Once can use `layerpxrd.m` in a similar manner.

Constructing an original model:

If one desires to start from a model derived from single crystal X-ray diffraction data, the structure can be transformed to fit the requirements for this script. The .cif file can be opened in a program such as Mercury (available free of cost at http://www.ccdc.cam.ac.uk/free_services/free_downloads/). Under Edit>Change Spacegroup setting, the user can switch the axes of the unit cell until a cell is found that contains the metal chain along the c axis. This can be saved as a .res file.

If one desires to prepare a 2D sheet for the layer shifting module, the structure can be generated by knowing the anticipated space group of any of the input stacking motifs (stacking, eclipsed, etc.) and by having an optimized geometry of the repeating unit. The structure can be copied into graphics software such as Adobe Illustrator and tessellated appropriately until a unit cell is formed. The position of each unique atom can then be calculated in fractional coordinates. Then, using a program such as ISOCIF (http://stokes.byu.edu/iso/isocif.html), one can generate a .cif file, which can be saved as a .res file.

Appendix C: MATLAB Scripts

C.1 breathing.m

```
function atom_type=breathing(theta)
%%%%breathing(theta) takes as an input the angle theta made between two
%%%%ligands meeting at the metal node. Also required are the name of the
%%%%coordinates file, text file of the powder diffraction pattern, desired
%%%%name of the output dummy.RES file, and unit cell parameters. Other
%%%%parameters that can be altered are the full-width of half maximum,
%%%%wavelength of the x-ray source, isotropic debye-waller parameter,
%%%%degree to which the calculated peak profile is Gaussian or Lorenzian,
%%%%maximum h,k,l values, and direction and degree of preferential
%%%%orientation. Any of the numerical quantities can be varied with
%%%%sliders by making them inputs.


%%%%%%Parameters for the user to change

%Specify the file that will supply atom types, x, y, z, and occupancy. This
%file should have the format: atom_type x y z occupancy. There should be no
%extraneous lines/text. This does not distinguish between tabs and spaces.
coordinates='CuBDT_coordinates.txt';
%Specify the file that will supply the experimental powder pattern. The
%file should contain two columns - one with the two theta values and the
%other with the intensities, in that order.
experimental_pattern='CuBDT_MeOH_pxrd.txt';
%%%%Specify the filename of the output dummy .RES file
resfilename='CuBDT_MeOH_simulated.res';
%%%%Specify the full width at half maximum
fwhm=0.1;
%Wavelength of the x-ray source in angstroms
lambda=1.54056;
%isotropic debye-waller parameter - usually between 3.5 and 6.5 square
%angstroms
Biso=0;
%%%Enter the unit cell parameters here
a=13.5747;
b=22.249;
c=7.0528;
alpha=90;
beta=90;
gamma=90;
%%%%End of unit cell input
%Enter % of calculated pattern you would like to have described by a
%lorentzian function vs. a gaussian function
eta=0.5;
%%%%%Enter the maximum h, k, and l values you would like to calculate. The
%%%%%calculated peaks will be for -hmax <= h <= hmax; -kmax<= k <= kmax;
%%%%%-lmax <= l <= lmax
hmax=3;
kmax=3;
lmax=3;
%%%Enter the degree (number greater than or equal to 0) and direction of
%preferential orientation
pref=0;
preferred_h=0;
```

```
preferred_k=1;
preferred_l=0;
%%%%No more parameters for the user to change


%%%%%%%Program starts here



%%%Converting to radians
alpha=alpha*pi/180;
beta=beta*pi/180;
gamma=gamma*pi/180;
theta=theta*pi/180;
%Reads in the atom type with number appended, x, y, and z from the
%specified file
[atom_type_and_number,x,y,z,occupancy]=textread(coordinates,'%s %f %f %f
%f');
%%%%Input the symmetry elements present here
x=[x;0.5+x];y=[y;0.5+y];z=[z;0.5+z];
atom_type_and_number=[atom_type_and_number.',atom_type_and_number.'].';
occupancy=[occupancy;occupancy];
x=[x;0.0-x;0.0+x;0.0+x;0.0-x;0.0+x;0.0-x;0.0-x];
y=[y;0.0+y;0.0-y;0.0+y;0.0-y;0.0-y;0.0+y;0.0-y];
z=[z;0.5+z;0.0+z;0.5-z;0.0-z;0.5-z;0.0-z;0.5+z];
atom_type_and_number=[atom_type_and_number.',atom_type_and_number.',atom_type
_and_number.',atom_type_and_number.',atom_type_and_number.',atom_type_and_num
ber.',atom_type_and_number.',atom_type_and_number.'].';
occupancy=[occupancy;occupancy;occupancy;occupancy;occupancy;occupancy;occupa
ncy;occupancy];
%%%%%%%%%%%Now trying to strip the number from the atom name
atom_type={''};
for n=1:length(atom_type_and_number)
    current=char(atom_type_and_number(n));
    %%%%Change the atom type+number from a cell to text
    if isempty(regexp(current,'\d'));
        atomtype_new=current;
    else
        atomtype_new=current(1:regexp(current,'\d')-1);
    end
    %%%%cut off the part of the name after the first appearance of a number
    cell={atomtype_new};
    atom_type(length(atom_type)+1)=cell;
    %%%Append this new atom name to the list of atom types
end
atom_type=atom_type(2:length(atom_type));
%%%%%%%%%%%%%%Done stripping number from atom name
%%%Change of unit cell parameters a and b corresponding to the new theta
%%%value

diagonal=(a^2+b^2)^(0.5);
a=diagonal*sin(theta/2);
b=diagonal*cos(theta/2);



%%%%%%%%%%%%%Setting up the different h,k,l values
```

```
l_values_temp=repmat(-1*lmax:lmax,1,(2*kmax+1)*(2*hmax+1));
k_repeat_unit=repmat(-1*kmax:kmax,(2*lmax+1),1);
k_values_temp=repmat(reshape(k_repeat_unit,1,(2*lmax+1)*(2*kmax+1)),1,(2*hmax
+1));
h_values_temp=reshape(repmat(-
1*hmax:hmax,(2*kmax+1)*(2*lmax+1),1),1,(2*hmax+1)*(2*kmax+1)*(2*lmax+1));
h_values_temp(hmax*(2*kmax+1)*(2*lmax+1)+kmax*(2*lmax+1)+lmax+1)=[];
k_values_temp(hmax*(2*kmax+1)*(2*lmax+1)+kmax*(2*lmax+1)+lmax+1)=[];
l_values_temp(hmax*(2*kmax+1)*(2*lmax+1)+kmax*(2*lmax+1)+lmax+1)=[];
h=h_values_temp;
k=k_values_temp;
l=l_values_temp;
%%%%%%%%%%%%%%%%Now we have all the h,k,l values with 0,0,0 taken out

%%%%%%%%%%%%%%Determine the two theta values for each h,k,l
V_cell=a*b*c*(1-cos(alpha)^2-cos(beta)^2-
cos(gamma)^2+2*cos(alpha)*cos(beta)*cos(gamma))^0.5;
one_over_dhkl=1/V_cell.*(h.^2*b^2*c^2*sin(alpha)^2+k.^2*a^2*c^2*sin(beta)^2+l
.^2*a^2*b^2*sin(gamma)^2+2.*h.*k*a*b*c^2*(cos(alpha)*cos(beta)-
cos(gamma))+2*k.*l*a^2*b*c*(cos(beta)*cos(gamma)-
cos(alpha))+2*h.*l*a*b^2*c*(cos(alpha)*cos(gamma)-cos(beta))).^(0.5);
two_theta=2.*asin(one_over_dhkl*lambda/2);
%http://classes.uleth.ca/200401/chem4000a/Lecture10.pdf
%%%%%%%%%%%%twotheta values now determined

%%%%%%%%%%%%%%Calculate the structure factor for each reflection
n=1;
structure_factor=0;
while(n<=length(atom_type))
    %%%%read in the parameters for the scattering factor equation and give
    %%%%them names
    sf_parameters=scattering_factor_parameters(atom_type(n));
    a1=sf_parameters(1);
    b1=sf_parameters(2);
    a2=sf_parameters(3);
    b2=sf_parameters(4);
    a3=sf_parameters(5);
    b3=sf_parameters(6);
    a4=sf_parameters(7);
    b4=sf_parameters(8);
    c_=sf_parameters(9);
    %%%%%Plug the parameters into the scattering factor equation
    scattering_factor=a1.*exp(-b1.*sin(two_theta/2).^2/lambda^2)+a2.*exp(-
b2.*sin(two_theta/2).^2/lambda^2)+a3.*exp(-
b3.*sin(two_theta/2).^2/lambda^2)+a4.*exp(-
b4.*sin(two_theta/2).^2/lambda^2)+c_;%Check
    %%%%%%Account for vibration in the form of the debye-waller factor
    scattering_factor=scattering_factor.*exp(-
Biso.*sin(two_theta/2).^2/lambda^2);
    %%%%%%Determine the contribution of the current atom to the overall
    %%%%%%structure factor

structure_factor=structure_factor+scattering_factor.*occupancy(n).*exp(2*pi*1
i.*(h*x(n)+k*y(n)+l*z(n)));
    n=n+1;
end
%%%%%square each term in the structure factor vector
```

```
F_squared=structure_factor.*conj(structure_factor);
%%%%Correction for preferred orientation
%%Angle between h,k,l and preferrential orientation direction
theta_pref_orient=acos((h*preferred_h + k*preferred_k +
l*preferred_l)./((h.^2+k.^2+l.^2).^0.5*(preferred_h^2+preferred_k^2+preferred
_l^2)^0.5));
if theta_pref_orient>pi/2
    theta_pref_orient=pi-theta_pref_orient;
end
F_squared=F_squared.*exp(pref*cos(2*theta_pref_orient));
%%%%read in the experimental pattern
[experimental_two_theta,unnormalized_experimental_intensity]=textread(experim
ental_pattern,'%f %f');
%%%%%convert the calculated two theta values to degrees for easier
%%%%%plotting
two_theta=180*two_theta/pi;

%%%%%Construct the calculated pxrd pattern by adding a lorentzian fraction
%%%%%%to a gaussian fraction

%%Gaussian part
c_=fwhm/(2*(2*log(2))^0.5);
n=1;
unnormalized_gauss=0;
while(n<=length(two_theta))
    unnormalized_gauss_contribution=F_squared(n).*exp(-
(experimental_two_theta-two_theta(n)).^2/(2*c_^2));
    unnormalized_gauss=unnormalized_gauss+unnormalized_gauss_contribution;
    n=n+1;
end
gauss_part=unnormalized_gauss/max(unnormalized_gauss);

%%Lorentzian part
n=1;
unnormalized_lorentz=0;
while(n<length(two_theta))
    unnormalized_lorentz_contribution=F_squared(n)./((experimental_two_theta-
two_theta(n)).^2+(0.5*fwhm)^2);

unnormalized_lorentz=unnormalized_lorentz+unnormalized_lorentz_contribution;
    n=n+1;
end
lorentz_part=unnormalized_lorentz/max(unnormalized_lorentz);
%%%%%%Mix together the Lorentzian and Gaussian parts in the ratio
%%%%%%specified by eta to generate the pseudo-Voigt function
calculated_intensity=eta*lorentz_part+(1-eta)*gauss_part;
%%%%%Now put in the Lorentz-Polarization factor:
calculated_intensity=calculated_intensity.*(1+cos(experimental_two_theta*pi/1
80).^2)./(8*sin(experimental_two_theta*pi/180/2).^2.*cos(experimental_two_the
ta*pi/180/2));
calculated_intensity=calculated_intensity/max(calculated_intensity);
%%%%normalize the experimental intensity
experimental_intensity=unnormalized_experimental_intensity/max(unnormalized_e
xperimental_intensity);

%%%%%Plot the calculated pattern in red and the experimental pattern in
%%%%%blue
```

```
plot(experimental_two_theta,calculated_intensity,'Color','red');
hold on
plot(experimental_two_theta,experimental_intensity);
hold off


%%%%Generate a dummy res file to visualize coordinates
resgenerator_1(a,b,c,alpha,beta,gamma,atom_type,x,y,z,occupancy,resfilename);
```

C.2 layerpxrd.m

```
function atom_type=layer_pxrd(q1,q2,q3)
%%%%%layer_shift_pxrd_calculator(h) takes three inputs. q1 is the shift along
a in fractional
%%%%%coordinates. q2 is the shift along b in fractional coordinates. q3 is
%%%%%the interlayer spacing. To use this function, you need to open up
%%%%%blah.m and type in the coordinate file, experimental pattern, unit cell
parameters, and a few parameters that
%%%%%describe the shape of the calculated peaks.


%%%%%%%Parameters for the user to change



%Specify the file that will supply atom types, x, y, and z. This file
%should have the format: atom_type x y z. There should be no extraneous
%lines/text. This does not distinguish between tabs and spaces.
coordinates='Cu_HHTP_MOF_coordinates.txt';
%Specify the file that will supply the experimental powder pattern. The
%file should contain two columns - one with the two theta values and the
%other with the intensities, in that order.
experimental_pattern='Cu_HHTP_MOF_experimental_pxrd_background_removed.txt';

resfilename='structure.res';
%Radius of the diffractometer in millimeters
R=500;
s=0.55;
pref=0;
fwhm=0.1;
%Wavelength of the x-ray source in angstroms
lambda=1.54056;
%isotropic debye-waller parameter - usually between 3.5 and 6.5 square
angstroms
Biso=0;
%%%Enter the unit cell parameters here
a=21.23;
b=21.23;
c=3.22;
alpha=90;
beta=90;
gamma=120;
%%%%End of unit cell input
%%%%%%%%%%%%%%Enter % of calculated pattern you would like to have
%%%%%%%%%%%%%%described by a lorentzian function vs. a gaussian function
eta=0.5;
%%%%%Enter the maximum h, k, and l values you would like to calculate. The
%%%%%calculated peaks will be for -hmax <= h <= hmax; -kmax<= k <= kmax;
%%%%%-lmax <= l <= lmax
hmax=3;
kmax=3;
lmax=3;
%%%Enter the direction of preferential orientation
preferred_h=0;
preferred_k=1;
preferred_l=0;
```

```
%%%%No more parameters for the user to change


%%%%%%%Program starts here


%%%Converting to radians
alpha=alpha*pi/180;
beta=beta*pi/180;
gamma=gamma*pi/180;
%Reads in the atom type with number appended, x, y, and z from the
%specified file
[atom_type_and_number,x,y,z,occupancy]=textread(coordinates,'%s %f %f %f
%f');


%%%%%%%%%%%Now trying to strip the number from the atom name
atom_type={''};
for n=1:length(atom_type_and_number)
    current=char(atom_type_and_number(n));
    %%%%Change the atom type+number from a cell to text
    if isempty(regexp(current,'\d'));
        atomtype_new=current;
    else
        atomtype_new=current(1:regexp(current,'\d')-1);
    end
    %%%%cut off the part of the name after the first appearance of a number
    cell={atomtype_new};
    atom_type(length(atom_type)+1)=cell;
    %%%Append this new atom name to the list of atom types
end
atom_type=atom_type(2:length(atom_type));
%%%%%%%%%%%%%%Done stripping number from atom name


%%%%Add the symmetry equivalents to finish up the layer
%x=[x;0.5+x];
%y=[y;y];
%z=[z;z];
%atom_type=[atom_type,atom_type];
%occupancy=[occupancy;occupancy];
%%%%Get the coordinates for the second layer
x_new=x+q1;
x=[x;x_new];
y_new=y+q2;
y=[y;y_new];
z=c/(2*q3)*z;
z_new=z+0.5;
z=[z;z_new];
c=2*q3;
atom_type=[atom_type,atom_type];
occupancy=[occupancy;occupancy];
%%%%Coordinates set for two layers and c value updated to deal with new
%%%%spacing



%%%%%%%%%%%%%%Setting up the different h,k,l values
l_values_temp=repmat(-1*lmax:lmax,1,(2*kmax+1)*(2*hmax+1));
```

```matlab
k_repeat_unit=repmat(-1*kmax:kmax,(2*lmax+1),1);
k_values_temp=repmat(reshape(k_repeat_unit,1,(2*lmax+1)*(2*kmax+1)),1,(2*hmax
+1));
h_values_temp=reshape(repmat(-
1*hmax:hmax,(2*kmax+1)*(2*lmax+1),1),1,(2*hmax+1)*(2*kmax+1)*(2*lmax+1));
h_values_temp(hmax*(2*kmax+1)*(2*lmax+1)+kmax*(2*lmax+1)+lmax+1)=[];
k_values_temp(hmax*(2*kmax+1)*(2*lmax+1)+kmax*(2*lmax+1)+lmax+1)=[];
l_values_temp(hmax*(2*kmax+1)*(2*lmax+1)+kmax*(2*lmax+1)+lmax+1)=[];
h=h_values_temp;
k=k_values_temp;
l=l_values_temp;
%%%%%%%%%%%%%%%%Now we have all the h,k,l values with 0,0,0 taken out

%%%%%%%%%%%%%%Determine the two theta values for each h,k,l
V_cell=a*b*c*(1-cos(alpha)^2-cos(beta)^2-
cos(gamma)^2+2*cos(alpha)*cos(beta)*cos(gamma))^0.5;
one_over_dhkl=1/V_cell.*(h.^2*b^2*c^2*sin(alpha)^2+k.^2*a^2*c^2*sin(beta)^2+l
.^2*a^2*b^2*sin(gamma)^2+2.*h.*k*a*b*c^2*(cos(alpha)*cos(beta)-
cos(gamma))+2*k.*l*a^2*b*c*(cos(beta)*cos(gamma)-
cos(alpha))+2*h.*l*a*b^2*c*(cos(alpha)*cos(gamma)-cos(beta))).^(0.5);
two_theta=2.*asin(one_over_dhkl*lambda/2);
%http://classes.uleth.ca/200401/chem4000a/Lecture10.pdf
%%%%%%%%%%%%twotheta values now determined

%%%%%%%%%%%%%%Calculate the structure factor for each reflection
n=1;
structure_factor=0;
while(n<=length(atom_type))
    %%%%read in the parameters for the scattering factor equation and give
    %%%%them names
    sf_parameters=scattering_factor_parameters(atom_type(n));
    a1=sf_parameters(1);
    b1=sf_parameters(2);
    a2=sf_parameters(3);
    b2=sf_parameters(4);
    a3=sf_parameters(5);
    b3=sf_parameters(6);
    a4=sf_parameters(7);
    b4=sf_parameters(8);
    c_=sf_parameters(9);
    %%%%%Plug the parameters into the scattering factor equation
    scattering_factor=a1.*exp(-b1.*sin(two_theta/2).^2/lambda^2)+a2.*exp(-
b2.*sin(two_theta/2).^2/lambda^2)+a3.*exp(-
b3.*sin(two_theta/2).^2/lambda^2)+a4.*exp(-
b4.*sin(two_theta/2).^2/lambda^2)+c_;%Check
    %%%%%%Account for vibration in the form of the debye-waller factor
    scattering_factor=scattering_factor.*exp(-
Biso.*sin(two_theta/2).^2/lambda^2);
    %%%%%%Determine the contribution of the current atom to the overall
    %%%%%%structure factor

structure_factor=structure_factor+scattering_factor.*exp(2*pi*1i.*(h*x(n)+k*y
(n)+l*z(n)));
    n=n+1;
end
%%%%square each term in the structure factor vector
F_squared=structure_factor.*conj(structure_factor);
```

```
%%%%%Correction for preferred orientation
%%Angle between h,k,l and preferrential orientation direction
theta_pref_orient=acos((h*preferred_h + k*preferred_k +
l*preferred_l)./((h.^2+k.^2+l.^2).^0.5*(preferred_h^2+preferred_k^2+preferred
_l^2)^0.5));

F_squared=F_squared.*exp(pref*abs(cos(theta_pref_orient)));
[h;k;l;two_theta*180/pi;exp(pref*abs(cos(theta_pref_orient)))]

%%%%%read in the experimental pattern
[experimental_two_theta,unnormalized_experimental_intensity]=textread(experim
ental_pattern,'%f %f');

%%%%%convert the calculated two theta values to degrees for easier
%%%%%plotting
two_theta=180*two_theta/pi;




%%%%%Construct the calculated pxrd pattern by adding a lorentzian fraction
%%%%%to a gaussian fraction

%%Gaussian part
c_=fwhm/(2*(2*log(2))^0.5);
n=1;
unnormalized_gauss=0;
while(n<=length(two_theta))
    unnormalized_gauss_contribution=F_squared(n).*exp(-
(experimental_two_theta-two_theta(n)).^2/(2*c_^2));
    unnormalized_gauss=unnormalized_gauss+unnormalized_gauss_contribution;
    n=n+1;
end
gauss_part=unnormalized_gauss/max(unnormalized_gauss);

%%Lorentzian part
n=1;
unnormalized_lorentz=0;
while(n<length(two_theta))
    unnormalized_lorentz_contribution=F_squared(n)./((experimental_two_theta-
two_theta(n)).^2+(0.5*fwhm)^2);

unnormalized_lorentz=unnormalized_lorentz+unnormalized_lorentz_contribution;
    n=n+1;
end
lorentz_part=unnormalized_lorentz/max(unnormalized_lorentz);
%%%%%%%Mix together the Lorentzian and Gaussian parts in the ratio
%%%%%%%specified by eta to generate the pseudo-Voigt function
calculated_intensity=eta*lorentz_part+(1-eta)*gauss_part;
%%%%%Now put in the Lorentz-Polarization factor:
calculated_intensity=calculated_intensity.*(1+cos(experimental_two_theta*pi/1
80).^2)./(8*sin(experimental_two_theta*pi/180/2).^2.*cos(experimental_two_the
ta*pi/180/2));
calculated_intensity=calculated_intensity/max(calculated_intensity);
%%%%normalize the experimental intensity
experimental_intensity=unnormalized_experimental_intensity/max(unnormalized_e
xperimental_intensity);
```

```
%%%Correct for sample displacement
sample_two_theta=experimental_two_theta+2*s/R*180/pi*cos(experimental_two_the
ta*pi/180*0.5);

%%%%%Plot the calculated pattern in red and the experimental pattern in
%%%%%blue
plot(sample_two_theta,calculated_intensity,'Color','red');
hold on
plot(experimental_two_theta,experimental_intensity);
hold off

%%%%Generate a dummy res file to visualize coordinates
%resgenerator_1(a,b,c,alpha,beta,gamma,atom_type,x,y,z,occupancy,resfilename)
;
```

C.3 resgenerator_1.m

```
function
y=resgenerator_1(a,b,c,alpha,beta,gamma,atomtypes,x,y,z,occupancy,resfilename
)
%%%This function takes as inputs the unit cell parameters, the atom types
%%%present (SFAC), the numbers of each atom present (UNIT), the atom list
%%%(atomtypes) as a row vector, the number corresponding to each atom type
%%%(atomnumbers) as a row vector, and the fractional coordinates x, y, and
%%%z as row vectors. It outputs a dummy res file that can be used to
%%%visualize the packing.
alpha=alpha*180/pi;beta=beta*180/pi;gamma=gamma*180/pi;
%Merge atoms that end up on the same site
x=mod(x,1);y=mod(y,1);z=mod(z,1);
n=1;
while(n<=length(x))
    m=n+1;
    while(m<=length(x))
        if x(n)==x(m) && y(n)==y(m) && z(n)==z(m)

x(m)=[];y(m)=[];z(m)=[];atomtypes(m)=[];occupancy(n)=occupancy(n)+occupancy(m
);occupancy(m)=[];
        else
            m=m+1;
        end
    end
    n=n+1;
end
occupancy=occupancy+10;
n=1;
SFAC=atomtypes(1);
while(n<=length(atomtypes))
    current=char(atomtypes(n));
    if sum(ismember(SFAC,current))>0
        n=n+1;
    else
        SFAC(length(SFAC)+1)={current};
        n=n+1;
    end
end
n=1;
atomnumbers=[];
UNIT=zeros(1,length(SFAC));
while(n<=length(atomtypes))
    current=char(atomtypes(n));
    atomnumbers(length(atomnumbers)+1)=find(ismember(SFAC,current),1);

UNIT(find(ismember(SFAC,current),1))=UNIT(find(ismember(SFAC,current),1))+1;
    n=n+1;
end

fid=fopen(resfilename,'w');
fprintf(fid,'TITL MATLAB structure\nCELL 0.71073 %3.4f %3.4f %3.4f %3.3f
%3.3f %3.3f\nZERR 1 0 0 0 0 0 0\nLATT -1\n',a,b,c,alpha,beta,gamma);
n=1;
fprintf(fid,'SFAC ');
while(n<=length(SFAC))
```

```
        fprintf(fid,'%s ',char(SFAC(n)));
        n=n+1;
end
fprintf(fid,'\n');
fprintf(fid,'UNIT ');
n=1;
while(n<=length(UNIT))
        fprintf(fid,'%d ',UNIT(n));
        n=n+1;
end
fprintf(fid,'\n');
fprintf(fid,'L.S. 10\nBOND $H\nFMAP 2\nPLAN 10\nWGHT 0.1\nFVAR 0.1 \n');
n=1;
while(n<=length(atomtypes))
        fprintf(fid,'%s %d %1.5f %1.5f %1.5f %1.5f
0.05\n',char(atomtypes(n)),atomnumbers(n),x(n),y(n),z(n),occupancy(n));
        n=n+1;
end
fprintf(fid,'HKLF 4\n\nEND');
y=5;
```

C.4 scattering_factor_parameters.m

```
function sf = scattering_factor_parameters(a)
a=char(a);
if strcmp(a,'H')
    sf=[0.493002 10.5109 0.322912 26.1257 0.140191 3.14236 0.040810 57.7997
0.003038];
elseif strcmp(a,'Li')%This is for Li(0)
    sf=[1.1282 3.9546 0.7508 1.0524 0.6175 85.3905 0.4653 168.261 0.0377];
%elseif strcmp(a,'Li')%This is for Li+
    %sf=[0.6968 4.6237 0.7888 1.9557 0.3414 0.6316 0.1563 10.0953 0.0167];
elseif strcmp(a,'C')
    sf=[2.31 20.8439 1.02 10.2075 1.5886 0.5687 0.865 51.6512 0.2156];
elseif strcmp(a,'N')
    sf=[12.2126 0.0057 3.1322 9.8933 2.0125 28.9975 1.1663 0.5826 -11.529];
elseif strcmp(a,'O')
    sf=[3.04850 13.2771 2.2868 5.7011 1.5463 0.3239 0.867 32.9089 0.2508];
elseif strcmp(a,'B')
    sf=[2.0545 23.2185 1.3326 1.021 1.0979 60.3498 0.7068 0.1403 -0.1932];
%elseif strcmp(a(b),'Na')%this is for Na+
%    sf=[3.2565 2.6671 3.93620 6.1153 1.3998 0.2001 1.0032 14.0390 0.404];
elseif strcmp(a,'Na')
    sf=[4.7626 3.285 3.1736 8.8422 1.2674 0.3136 1.1128 129.424 0.676];
elseif strcmp(a,'Si')
    sf=[6.2915 2.4386 3.0353 32.3337 1.9891 0.6785 1.541 81.6937 1.1407];
elseif strcmp(a,'P')
    sf=[6.4345 1.9067 4.1791 27.1570 1.7800 0.526 1.4908 68.1645 11.1149];
elseif strcmp(a,'S')
    sf=[6.9053 1.46790 5.2034 22.2151 1.4379 0.2536 1.5863 56.172 0.8669];
%elseif strcmp(a,'Cl')%this is for Cl-
%    sf=[18.2915 0.0066 7.2084 1.1717 6.5337 19.5424 2.3386 60.4486 -16.378];
elseif strcmp(a,'Cl')
    sf=[11.4604 0.0104 7.1964 1.16620 6.25560 18.5194 1.6455 47.7784 -
9.5574];
elseif strcmp(a,'Cr')
    sf=[10.6406 6.1038 7.3537 0.392 3.324 20.2626 1.4922 98.7399 1.1832];
elseif strcmp(a,'Mn')
    sf=[11.2819 5.3409 7.3573 0.3432 3.01930 17.8674 2.24410 83.7543
1.08960];
elseif strcmp(a,'Fe')
    sf=[11.7695 4.7611 7.3573 0.3072 3.5222 15.3535 2.3045 76.8805 1.0369];
elseif strcmp(a,'Co')
    sf=[12.2841 4.2791 7.3409 0.2784 4.0034 13.5359 2.2488 71.1692 1.0118];
elseif strcmp(a,'Ni')
    sf=[12.8376 3.8785 7.292 0.2565 4.4438 12.1763 2.38 66.3421 1.0341];
elseif strcmp(a,'Cu')
    sf=[13.338 3.5828 7.1676 0.247 5.6158 11.3966 1.6735 64.8126 1.191];
elseif strcmp(a,'Zn')
    sf=[14.0743 3.2655 7.0318 0.2333 5.1652 10.3163 2.41 58.7097 1.3041];
elseif strcmp(a,'Se')
    sf=[17.0006 2.4098 5.8196 0.2726 3.9731 15.2372 4.3543 43.8163 2.8409];
elseif strcmp(a,'Cs')
    sf=[20.3892 3.569 19.1062 0.3107 10.662 24.3879 1.4953 213.904 3.3352];
%elseif strcmp(a,'Cs')%this is for Cs+
    %sf=[20.3524 3.552 19.1278 0.3086 10.2821 23.7128 0.9615 59.4565 3.2791];
elseif strcmp(a,'Mo')
    sf=[3.7025 0.2772 17.2356 1.0958 12.8876 11.004 3.7429 61.6584 4.3875];
```

end

References

(1) Brandon, N. P.; Brett, D. J. *Phil. Trans. R. Soc. A* **2006**, *364*, 147–59.

(2) Yuhas, B. D.; Smeigh, A. L.; Samuel, A. P. S.; Shim, Y.; Bag, S.; Douvalis, A. P.; Wasielewski, M. R.; Kanatzidis, M. G. *J. Am. Chem. Soc.* **2011**, *133*, 7252–5.

(3) Yuhas, B. D.; Prasittichai, C.; Hupp, J. T.; Kanatzidis, M. G. *J. Am. Chem. Soc.* **2011**, *133*, 15854–15857.

(4) Simon, P.; Gogotsi, Y. *Nat. Mater.* **2008**, *7*, 845–54.

(5) Lang, X.; Hirata, A.; Fujita, T.; Chen, M. *Nat. Nanotechnol.* **2011**, *6*, 232–236.

(6) Popere, B. C.; Della Pelle, A. M.; Poe, A.; Thayumanavan, S. *Phys. Chem. Chem. Phys.* **2012**, *14*, 4043–4057.

(7) Côté, A. P.; Benin, A. I.; Ockwig, N. W.; O'Keeffe, M.; Matzger, A. J.; Yaghi, O. M. *Science* **2005**, *310*, 1166–70.

(8) Tilford, R. W.; Mugavero, S. J.; Pellechia, P. J.; Lavigne, J. J. *Adv. Mater.* **2008**, *20*, 2741–2746.

(9) Doonan, C. J.; Tranchemontagne, D. J.; Glover, T. G.; Hunt, J. R.; Yaghi, O. M. *Nat. Chem.* **2010**, *2*, 235–238.

(10) Tilford, R. W.; Gemmill, W. R.; zur Loye, H.; Lavigne, J. J. *Chem. Mater.* **2006**, *18*, 5296–5301.

(11) Côté, A. P.; El-Kaderi, H. M.; Furukawa, H.; Hunt, J. R.; Yaghi, O. M. *J. Am. Chem. Soc.* **2007**, *129*, 12914–12915.

(12) Dogru, M.; Sonnauer, A.; Gavryushin, A.; Knochel, P.; Bein, T. *Chem. Commun.* **2011**, *47*, 1707–9.

(13) Ding, X.; Guo, J.; Feng, X.; Honsho, Y.; Guo, J.; Seki, S.; Maitarad, P.; Saeki, A.; Nagase, S.; Jiang, D. *Angew. Chem. Int. Ed.* **2010**, *50*, 1289–1293.

(14) Spitler, E. L.; Dichtel, W. R. *Nat. Chem.* **2010**, *2*, 672–677.

(15) Feng, X.; Chen, L.; Dong, Y.; Jiang, D. *Chem. Commun.* **2011**, 8–10.

(16) El-Kaderi, H. M.; Hunt, J. R.; Mendoza-Cortés, J. L.; Côté, A. P.; Taylor, R. E.; O'Keeffe, M.; Yaghi, O. M. *Science* **2007**, *316*, 268–72.

(17) Wan, S.; Guo, J.; Kim, J.; Ihee, H.; Jiang, D. *Angew. Chem. Int. Ed.* **2008**, *47*, 8826–30.

(18) Spitler, E. L.; Colson, J. W.; Uribe-Romo, F. J.; Woll, A. R.; Giovino, M. R.; Saldivar, A.; Dichtel, W. R. *Angew. Chem. Int. Ed.* **2012**, *208*, 1–6.

(19) Hunt, J. R.; Doonan, C. J.; LeVangie, J. D.; Côté, A. P.; Yaghi, O. M. *J. Am. Chem. Soc.* **2008**, *130*, 11872–3.

(20) Uribe-Romo, F. J.; Hunt, J. R.; Furukawa, H.; Klöck, C.; O'Keeffe, M.; Yaghi, O. M. *J. Am. Chem. Soc.* **2009**, *131*, 4570–1.

(21) Uribe-Romo, F. J.; Doonan, C. J.; Furukawa, H.; Oisaki, K.; Yaghi, O. M. *J. Am. Chem. Soc.* **2011**, *133*, 11478–11481.

(22) Reich, T. E.; Jackson, K. T.; Li, S.; Jena, P.; El-Kaderi, H. M. *J. Mater. Chem.* **2011**, *21*, 10629–10632.

(23) Rabbani, M. G.; El-kaderi, H. M. *Chem. Mater.* **2011**, *23*, 1650–1653.

(24) Wan, S.; Guo, J.; Kim, J.; Ihee, H.; Jiang, D. *Angew. Chem. Int. Ed.* **2009**, *48*, 5439–42.

(25) Lukose, B.; Kuc, A.; Heine, T. *Chem. Eur. J.* **2011**, *17*, 2388–2392.

(26) Patwardhan, S.; Kocherzhenko, A. A.; Grozema, F. C.; Siebbeles, L. D. A. *J. Phys. Chem. C* **2011**, *115*, 11768–11772.

(27) Feng, X.; Liu, L.; Honsho, Y.; Saeki, A.; Seki, S.; Irle, S.; Dong, Y.; Nagai, A.; Jiang, D. *Angew. Chem. Int. Ed.* **2012**, *51*, 2618–2622.

(28) Wan, S.; Felipe, G.; Liao, L.; Ambrogio, M. W.; Botros, Y. Y.; Duan, X.; Seki, S.; Stoddart, J. F.; Yaghi, O. M. *Chem. Mater.* **2011**, *23*, 4094–4097.

(29) Chen, L.; Kim, J.; Ishizuka, T.; Honsho, Y.; Saeki, A.; Seki, S.; Ihee, H.; Jiang, D. *J. Am. Chem. Soc.* **2009**, *131*, 7287–92.

(30) Ding, X.; Chen, L.; Honsho, Y.; Feng, X.; Saengsawang, O.; Guo, J.; Saeki, A.; Seki, S.; Irle, S.; Nagase, S.; Parasuk, V.; Jiang, D. *J. Am. Chem. Soc.* **2011**, *133*, 14510–14513.

(31) McKeown, N. B.; Makhseed, S.; Budd, P. M. *Chem. Commun.* **2002**, *44*, 2780–1.

(32) Spitler, E. L.; Giovino, M. R.; White, S. L.; Dichtel, W. R. *Chem. Sci.* **2011**, *2*, 1588–1593.

(33) Inabe, T.; Tajima, H. *Chem. Rev.* **2004**, *104*, 5503–34.

(34) Parker, V. D. *J. Am. Chem. Soc.* **1976**, *98*, 98–103.

(35)   Lemaur, V.; da Silva Filho, D. a; Coropceanu, V.; Lehmann, M.; Geerts, Y.; Piris, J.; Debije, M. G.; van de Craats, A. M.; Senthilkumar, K.; Siebbeles, L. D. a; Warman, J. M.; Brédas, J.-L.; Cornil, J. *J. Am. Chem. Soc.* **2004**, *126*, 3271–9.

(36)   Lehmann, M.; Kestemont, G.; Gómez Aspe, R.; Buess-Herman, C.; Koch, M. H. J.; Debije, M. G.; Piris, J.; de Haas, M. P.; Warman, J. M.; Watson, M. D.; Lemaur, V.; Cornil, J.; Geerts, Y. H.; Gearba, R.; Ivanov, D. a. *Chem. Eur. J.* **2005**, *11*, 3349–3362.

(37)   Crispin, X.; Cornil, J.; Friedlein, R.; Okudaira, K. K.; Lemaur, V.; Crispin, A.; Kestemont, G.; Lehmann, M.; Fahlman, M.; Lazzaroni, R.; Geerts, Y.; Wendin, G.; Ueno, N.; Brédas, J.-L.; Salaneck, W. R. *J. Am. Chem. Soc.* **2004**, *126*, 11889–99.

(38)   Roy, S.; Kubiak, C. P. *Dalton Trans.* **2010**, *39*, 10937–43.

(39)   Patra, S.; Sarkar, B.; Ghumaan, S.; Fiedler, J.; Kaim, W.; Lahiri, G. K. *Dalton Trans.* **2004**, *3*, 754–8.

(40)   Catalano, V. J.; Larson, W. E.; Olmstead, M. M.; Gray, H. B. *Inorg. Chem.* **1994**, *33*, 4502–4509.

(41)   Kirsch-De Mesmaeker, A.; Jacquet, L.; Masschelein, A.; Vanhecke, F.; Heremans, K. *Inorg. Chem.* **1989**, *28*, 2465–2470.

(42)   Alfonso, M.; Stoeckli-Evans, H. *Acta Crystallogr. E* **2001**, *57*, o242–o244.

(43)   Ong, C.; Liao, S.; Chang, T.; Hsu, H. *Tetrahedron Lett.* **2003**, *44*, 1477–1480.

(44)   Rosen, B. M.; Wilson, D. A.; Wilson, C. J.; Peterca, M.; Won, B. C.; Huang, C.; Lipski, L. R.; Zeng, X.; Ungar, G.; Heiney, P. A.; Percec, V. *J. Am. Chem. Soc.* **2009**, *131*, 17500–17521.

(45)   Servaty, K.; Moucheron, C.; Kirsch-De Mesmaeker, A. *Dalton Trans.* **2011**, *40*, 11704–11.

(46)   Liu, R.; von Malotki, C.; Arnold, L.; Koshino, N.; Higashimura, H.; Baumgarten, M.; Müllen, K. *J. Am. Chem. Soc.* **2011**, *133*, 10372–10375.

(47)   Rutherford, T. J.; Van Gijte, O.; Kirsch-De Mesmaeker, A.; Keene, F. R. *Inorg. Chem.* **1997**, *36*, 4465–4474.

(48)   Hurtley, W. R. H.; Smiles, S. *J. Chem. Soc.* **1926**, *129*, 2263–2270.

(49)   *TTF chemistry: fundamentals and applications of tetrathiafulvalene*; Yamada, J.; Sugimoto, T., Eds.; Springer-Verlag: New York, 2004.

(50) Wudl, F.; Smith, G. M.; Hufnagel, E. J. *J. Chem. Soc. D: Chem. Commun.* **1970**, 1453–1454.

(51) Wudl, F.; Wobschall, D.; Hufnagel, E. J. *J. Am. Chem. Soc.* **1972**, *94*, 670–672.

(52) Kistenmacher, T. J.; Phillips, T. E.; Cowan, D. O. *Acta Crystallogr. B* **1974**, *30*, 763–768.

(53) Howard, M. J.; Heirtzler, F. R.; Dias, S. I. G. *J. Org. Chem.* **2008**, *73*, 2548–2553.

(54) Ivanov, A. V.; Svinareva, P. A.; Tomilova, L. G.; Zefirov, N. S. *Russ. Chem. Bull. Int. Ed.* **2001**, *50*, 919–920.

(55) Adams, R.; Reirschneider, W.; Ferretti, A. *Org. Synth., Coll.* **1973**, *5*, 107–110.

(56) Prakash, I.; Muralidharan, P.; Nallamuthu, N.; Venkateswarlu, M.; Satyanarayana, N. *Materials Research Bulletin* **2007**, *42*, 1619–1624.

(57) Ferretti, A. *Org. Synth., Coll.* **1973**, *5*, 419–421.

(58) Inayoshi, T.; Ono, I. *Synth. Met.* **2000**, *110*, 153–163.

(59) Eddaoudi, M.; Moler, D. B.; Li, H.; Chen, B.; Reineke, T. M.; O'Keeffe, M.; Yaghi, O. M. *Acc. Chem. Res.* **2001**, *34*, 319–30.

(60) Aromí, G.; Barrios, L. a.; Roubeau, O.; Gamez, P. *Coord. Chem. Rev.* **2011**, *255*, 485–546.

(61) Gagnon, K. J.; Perry, H. P.; Clearfield, A. *Chem. Rev.* **2012**, *112*, 1034–54.

(62) Shimizu, G. K. H.; Vaidhyanathan, R.; Taylor, J. M. *Chem. Soc. Rev.* **2009**, *38*, 1430–49.

(63) Chui, S. S.-Y.; Lo, S. M.-F.; Charmant, J. P. H.; Orpen, A. G.; Williams, I. D. *Science* **1999**, *283*, 1148–1150.

(64) Li, H.; Eddaoudi, M.; O'Keeffe, M.; Yaghi, O. M. *Nature* **1999**, *402*, 276–279.

(65) Koh, K.; Wong-Foy, A. G.; Matzger, A. J. *J. Am. Chem. Soc.* **2009**, *131*, 4184–5.

(66) Farha, O. K.; Özgür Yazaydın, A.; Eryazici, I.; Malliakas, C. D.; Hauser, B. G.; Kanatzidis, M. G.; Nguyen, S. T.; Snurr, R. Q.; Hupp, J. T. *Nat. Chem.* **2010**, *2*, 944–948.

(67) Chae, H. K.; Siberio-Pérez, D. Y.; Kim, J.; Go, Y.; Eddaoudi, M.; Matzger, A. J.; O'Keeffe, M.; Yaghi, O. M. *Nature* **2004**, *427*, 523–527.

(68) Furukawa, H.; Ko, N.; Go, Y. B.; Aratani, N.; Choi, S. B.; Choi, E.; Yazaydin, a O.; Snurr, R. Q.; O'Keeffe, M.; Kim, J.; Yaghi, O. M. *Science* **2010**, *329*, 424–8.

(69) Furukawa, H.; Miller, M. a.; Yaghi, O. M. *J. Mater. Chem.* **2007**, *17*, 3197-3204.

(70) Sumida, K.; Rogow, D. L.; Mason, J. a; McDonald, T. M.; Bloch, E. D.; Herm, Z. R.; Bae, T.-H.; Long, J. R. *Chem. Rev.* **2012**, *112*, 724–81.

(71) Suh, M. P.; Park, H. J.; Prasad, T. K.; Lim, D.-W. *Chem. Rev.* **2012**, *112*, 782–835.

(72) Wu, H.; Gong, Q.; Olson, D. H.; Li, J. *Chem. Rev.* **2012**, *112*, 836–68.

(73) Li, J.-R.; Sculley, J.; Zhou, H.-C. *Chem. Rev.* **2012**, *112*, 869–932.

(74) Yoon, M.; Srirambalaji, R.; Kim, K. *Chem. Rev.* **2012**, *112*, 1196–231.

(75) Lee, J.; Farha, O. K.; Roberts, J.; Scheidt, K. a; Nguyen, S. T.; Hupp, J. T. *Chem. Soc. Rev.* **2009**, *38*, 1450–9.

(76) Férey, G.; Millange, F.; Morcrette, M.; Serre, C.; Doublet, M.-L.; Grenèche, J.-M.; Tarascon, J.-M. *Angew. Chem. Int. Ed.* **2007**, *46*, 3259–63.

(77) Takaishi, S.; Hosoda, M.; Kajiwara, T.; Miyasaka, H.; Yamashita, M.; Nakanishi, Y.; Kitagawa, Y.; Yamaguchi, K.; Kobayashi, A.; Kitagawa, H. *Inorg. Chem.* **2009**, *48*, 9048–50.

(78) Kobayashi, Y.; Jacobs, B.; Allendorf, M. D.; Long, J. R. *Chem. Mater.* **2010**, *22*, 4120–4122.

(79) Creutz, C.; Taube, H. *J. Am. Chem. Soc.* **1969**, *91*, 3988–3989.

(80) Narita, M.; Pittman, C. U. *Synthesis* **1976**, 489–514.

(81) Krief, A. *Tetrahedron* **1986**, *42*, 1209–1252.

(82) Schukat, G.; Fanghänel, E. *Sulfur Reports* **1996**, *18*, 1–278.

(83) Imakubo, T.; Maruyama, T.; Sawa, H.; Kobayashi, K. *Chem. Commun.* **1998**, 2021–2022.

(84) Munakata, M.; Kuroda-sowa, T.; Maekawa, M.; Hirota, A.; Wiley, J. *Inorg. Chem.* **1995**, *34*, 2705–2710.

(85) Nguyen, T. L. A.; Demir-Cakan, R.; Devic, T.; Morcrette, M.; Ahnfeldt, T.; Auban-Senzier, P.; Stock, N.; Goncalves, A.-M.; Filinchuk, Y.; Tarascon, J.-M.; Férey, G. *Inorg. Chem.* **2010**, *49*, 7135–7143.

(86) Mitamura, Y.; Yorimitsu, H.; Oshima, K.; Osuka, A. *Chem. Sci.* **2011**, *2*, 2017–2021.

(87) Li, J.-R.; Zhou, H.-C. *Angew. Chem. Int. Ed.* **2009**, *48*, 8465–8.

(88) Chen, B.; Ockwig, N. W.; Fronczek, F. R.; Contreras, D. S.; Yaghi, O. M. *Inorg. Chem.* **2005**, *44*, 181–3.

(89) Chen, B.; Ockwig, N. W.; Millward, A. R.; Contreras, D. S.; Yaghi, O. M. *Angew. Chem. Int. Ed.* **2005**, *44*, 4745–4749.

(90) Blessing, R. H.; Coppens, P. *Solid State Commun.* **1974**, *15*, 215–221.

(91) Williams, R.; Lowe Ma, C.; Samson, S.; Khanna, S. K.; Somoano, R. B. *J. Chem. Phys.* **1980**, *72*, 3781.

(92) Aumüller, A.; Erk, P.; Hünig, S.; von Schütz, J. U.; Werner, H.-P.; Wolf, H. C.; Klebe, G. *Chem. Ber.* **1991**, *124*, 1445–1451.

(93) Mori, T.; Inokuchi, H. *Bull. Chem. Soc. Jpn.* **1992**, *65*, 1460–1462.

(94) Webb, P. A.; Orr, C. *Analytical Methods in Fine Particle Technology*; Micromeritics Instr. Corp.: Norcross, GA, 1997.

(95) Hünig, S.; Kießlich, G.; Quast, H.; Scheutzow, D. *Liebigs Ann. Chem.* **1973**, 310–323.

(96) Matsuzaki, S.; Koga, N.; Moriyama, I.; Toyoda, K. *Bull. Chem. Soc. Jpn.* **1983**, *56*, 2090–2092.

(97) Kim, Y. I.; Hatfield, W. E. *Inorg. Chim. Acta* **1991**, *188*, 15–24.

(98) Klots, C. E.; Compton, R. N.; Raaen, V. F. *J. Chem. Phys.* **1974**, *60*, 1177–1178.

(99) Sato, N.; Saito, G.; Inokuchi, H. *J. Chem. Phys.* **1983**, *76*, 79–88.

(100) Dolomatov, M. Y.; Mukaeva, G. R. *J. Appl. Spec.* **1992**, *56*, 344–347.

(101) Takahata, Y. *J. Mol. Struc. - THEOCHEM* **1984**, *108*, 269–279.

(102) Meeks, J.; Wahlborg, A.; McGlynn, S. P. *J. Electron Spectrosc. Relat. Phenom.* **1981**, *22*, 43–52.

(103) Spanggaard, H.; Prehn, J.; Nielsen, M. B.; Levillain, E.; Allain, M.; Becher, J.; Chemie, O.; Zu, C.- *J. Am. Chem. Soc.* **2000**, *122*, 9486–9494.

(104) Ziganshina, A. Y.; Ko, Y. H.; Jeon, W. S.; Kim, K. *Chem. Commun.* **2004**, 806–7.

(105) Yoshizawa, M.; Kumazawa, K.; Fujita, M. *J. Am. Chem. Soc.* **2005**, *127*, 13456–7.

(106) Coskun, A.; Spruell, J. M.; Barin, G.; Fahrenbach, A. C.; Forgan, R. S.; Colvin, M. T.; Carmieli, R.; Benítez, D.; Tkatchouk, E.; Friedman, D. C.; Sarjeant, A. a; Wasielewski, M. R.; Goddard, W. a; Stoddart, J. F. *J. Am. Chem. Soc.* **2011**, *133*, 4538–47.

(107) Bejger, C.; Davis, C. M.; Park, J. S.; M Lynch, V.; Love, J. B.; Sessler, J. L. *Org. Lett.* **2011**, *13*, 4902–5.

(108) Robin, M. B.; Day, P. *Adv. Inorg. Chem. Radiochem.* **1968**, *10*, 247–422.

(109) Hush, N. S. *Coord. Chem. Rev.* **1985**, *64*, 135–157.

(110) Saeki, A.; Seki, S.; Koizumi, Y.; Tagawa, S. *J. Photochem. Photobiol. A* **2007**, *186*, 158–165.

(111) Saeki, A.; Koizumi, Y.; Aida, T.; Seki, S. *Acc. Chem. Res.* **2012**, *45*, 1193-1202.

(112) Sirringhaus, H.; Brown, P. J.; Friend, R. H.; Nielsen, M. M.; Bechgaard, K.; Sangeveld-Voss, B. M. W.; Spiering, A. J. H.; Janssen, R. A. J.; Meijer, E. W.; Herwig, P.; de Leeuw, D. M. *Nature* **1999**, *401*, 685–688.

(113) McCulloch, I.; Heeney, M.; Bailey, C.; Genevicius, K.; Macdonald, I.; Shkunov, M.; Sparrowe, D.; Tierney, S.; Wagner, R.; Zhang, W.; Chabinyc, M. L.; Kline, R. J.; McGehee, M. D.; Toney, M. F. *Nat. Mater.* **2006**, *5*, 328–33.

(114) Bright, A. A.; Chaikin, P. M.; McGhie, A. R. *Phys. Rev. B* **1974**, *10*, 3560–3568.

(115) Brédas, J. L.; Calbert, J. P.; da Silva Filho, D. a; Cornil, J. *Proc. Natl. Acad. Sci.* **2002**, *99*, 5804–9.

(116) Li, M.; Dincă, M. *J. Am. Chem. Soc.* **2011**, *133*, 12926–9.

(117) Shustova, N. B.; Ong, T.-C.; Cozzolino, A. F.; Michaelis, V. K.; Griffin, R. G.; Dinca, M. *J. Am. Chem. Soc.* **2012**, DOI: 10.1021/ja306042w.

(118) Favre-Nicolin, V.; Černý, R. *J. Appl. Cryst.* **2002**, *35*, 734–743.

(119) Cowley, J. M. Scattering factors for the diffraction of electrons by crystalline solids. *International Tables of Crystallography* **2006**, 259–262.

(120) Sumida, K.; Foo, M. L.; Horike, S.; Long, J. R. *Eur. J. Inorg. Chem.* **2010**, *2010*, 3739–3744.

(121) Demessence, A.; Long, J. R. *Chem. Eur. J.* **2010**, *16*, 5902–8.

(122) Le Bail, A.; Duroy, H.; Fourquet, J. L. *Mat. Res. Bull.* **1988**, *23*, 447–452.

Tarun Narayan
tnarayan@mit.edu

Work Address
77 Massachusetts Ave, Bldg. 6-433
Cambridge, MA 02139
(617) 225-6235

Home Address
319 Albany St, Apt 319B
Cambridge, MA 02139
(408) 608-4983

Interests
Synthetic chemistry; Charge transport processes; Excitonic phenomena; Photonic phenomena

Education
Massachusetts Institute of Technology, Cambridge, MA
M.S. Chemistry

Harvey Mudd College, Claremont, CA
B.S. with High Honors, Chemistry, May 2010

Experience

Research Assistant, Massachusetts Institute of Technology   July 2010-August 2012
Advisor: Mircea Dincă
Project: Designing, preparing, and characterizing electronically
conducting porous, conductive materials

Research Assistant, Harvey Mudd College   September 2009-May 2010
Advisor: Adam Johnson
Project: Developing and testing tantalum-based molecular catalysts for
the asymmetric hydroamination of aminoallenes

CPIMA SURE Summer Intern, Almaden Research Center, IBM   June 2009-August 2009
Advisor: James Hedrick
Project: Developing a new organic catalyst and initiator for the ring
opening polymerization of lactide

Research Assistant, Harvey Mudd College   September 2008-May 2009
Advisor: Hal Van Ryswyk
Project: Synthesis of osmium porphyrins for electron transfer studies

Research Assistant, University of Kentucky, Lexington   May 2008-August 2008
Advisor: John Anthony
Project: Synthesis and testing of anthradithiophenes as organic electronic
materials

Summer Intern, Bloom Energy   May 2007-August 2007
Mentor: Jeffrey Rossel
Project: Testing of fuel cells and fuel cell components, data analysis, and
testing station construction

Awards
DOE Science Graduate Fellow
NSF GRFP Honorable Mention, 2011
Davison Fellow, Massachusetts Institute of Technology
C. P. Chu and Y. Lai Summer Fellow, Massachusetts Institute of Technology
Richard R. Schrock Summer Graduate Fellow, Massachusetts Institute of Technology
ACS Division of Inorganic Chemistry 2009 Undergraduate Award in Inorganic Chemistry

Publications and Presentations
"High Charge Mobility in a Tetrathiafulvalene-Based Microporous Metal-Organic Framework" **Narayan, T. C.**; Miyakai, T.; Seki, S.; Dincă, M. DOI: 10.1021/ja3059827

"Using MATLAB to model structural changes in dynamic materials" **Narayan, T. C.** Dincă, M. *in preparation*

"Asymmetric Catalytic Hydroamination of Aminoallenes by Tantalum Amidoalkoxide Complexes" Hansen, M. C.; Heusser, C. A.; **Narayan, T. C.**; Fong, K. E.; Hara, N.; Kohn, A. W.; Venning, A. R.; Rheingold, A. L.; Johnson, A. R. *Organometallics* **2011**, *30*, 4616.

"Sterically congested tantalum(V) complexes for the asymmetric hydroamination of aminoallenes" **Narayan, T. C.**; Near, K. E.; Johnson, A. R. *ACS Meeting*, 22 March 2010, San Francisco, CA.

"Metalloporphyrins: intramolecular coupling and injectin efficiency on zinc oxide nanotube photoanodes" Eisenmenger, N. D.; Hickman, A.; McQueen, T. A.; Pakula, R. J.; Pankratz, S. C.; **Narayan, T. C.**; Rayermann, G. E.; Jensen, R. A.; Hupp, J. T.; Cave, R. J.; Van Ryswyk, H. *Gordon Research Seminar, Renewable Energy: Solar Fuels*, 31 January 2009, Ventura, CA.

Professional Memberships
American Chemical Society
Sigma Xi
Phi Lambda Upsilon